Double Spin Asymmetry in Exclusive π^+ Electroproduction with CLAS
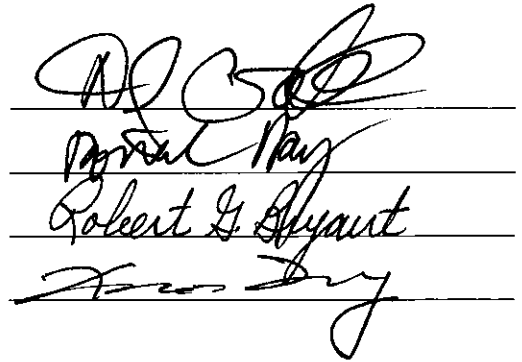
Joshua James Pierce
Charlottesville, VA

B.S., University of Virginia, 2001
M.A., University of Virginia, 2004

A Dissertation presented to the Graduate Faculty of the
University of Virginia in Candidacy for the Degree of
Doctor of Philosophy

Department of Physics

University of Virginia
January, 2008

Robert G. Bryant

Abstract

Measuring the spin structure of the resonances is important for understanding the strong force. The spin asymmetries for pion electroproduction can be used to measure this spin structure. The eg1b run was conducted using CLAS (CEBAF Large Acceptance Spectrometer) at the Thomas Jefferson National Accelerator Facility (TJNAF) in 2000 by the CLAS collaboration. A 1.6 GeV - 5.6 GeV polarized electron beam and polarized nuclear targets (composed of NH_3 or ND_3) were used, allowing spin asymmetries to be measured. This analysis is of the double spin asymmetry $A_\parallel$ in the exclusive production of positive pions from a polarized proton ($ep \rightarrow e\pi^+ n$). The two single spin asymmetries have also been measured.

Contents

List of Figures

Chapter 1

Introduction and Motivation

1.1   Introduction

For many years, physics research has operated under the understanding that there
are four types of forces. The electro-magnetic force, the weak force, the strong nu-
clear force, and gravitation (the weak and electro-magnetic forces have been unified
under one theory, but the other two forces remain separate). Modern particle physics
is largely concerned with the strong nuclear force. The theory of QCD (quantum
chromo-dynamics) is an attempt to understand this force.

   Electron scattering from a nuclear target is a widely used tool for the exploration
of QCD. Electron scattering experiments are used primarily for two reasons. The
first is that the electron is not a strongly interacting particle. Therefore, the action
of an electron is governed solely by the theory of quantum electro-dynamics, perhaps
the best understood and most carefully tested theory in modern physics, and does
not alter the QCD system. The accuracy with which the parameters of QED are
known allows for the the contributions of the electron to the scattering to be taken
into account in a very precise way. The second reason is that electrons are relatively

easy to accelerate to high energies, compared to neutral particles for example. The value of the total number of particles per unit area of the beam times the number of target particles is referred to as the luminosity, and it is this number, along with the cross-section, that determines the overall scattering rate. The statistical error on a measurement is directly related to the number of scattered particles, so it is important to have as high a number of beam particles as possible to make precise measurements. Additionally, the spatial resolution of the measurement is directly related to the energy of the particle. The ability to create high energy, high luminosity electron beams make electrons an attractive choice for scattering experiments.

Inclusive measurements of electron scattering off of proton and neutron targets have revealed the existence of several resonances (short lived particles that are excited states of the proton or neutron) [1] [2] generally grouped into three resonance regions. The three resonances regions can be seen clearly in Fig. 1.1. Information about the resonances is essential to a proper understanding of the strong force. The resonances represent a region where the interactions between the quarks is not yet well described by theory, unlike, for example the high energy regime which is reasonable described through perturbative QCD. An understanding of the structure of the resonances would correspond to an understanding of the interactions of the three quarks within the resonance, and therefore and understanding of the strong force in this regime.

The individual resonances in the resonance regions have been cataloged and various properties of each have been explored, including the mass, through inclusive scattering. By identifying the scattered target particles, still more information about the resonances was obtained, allowing for the determination of the quantum numbers (such as the spin and isospin) and the branching ratios of theses states.

There is an additional way to gain information about the resonances. By control-
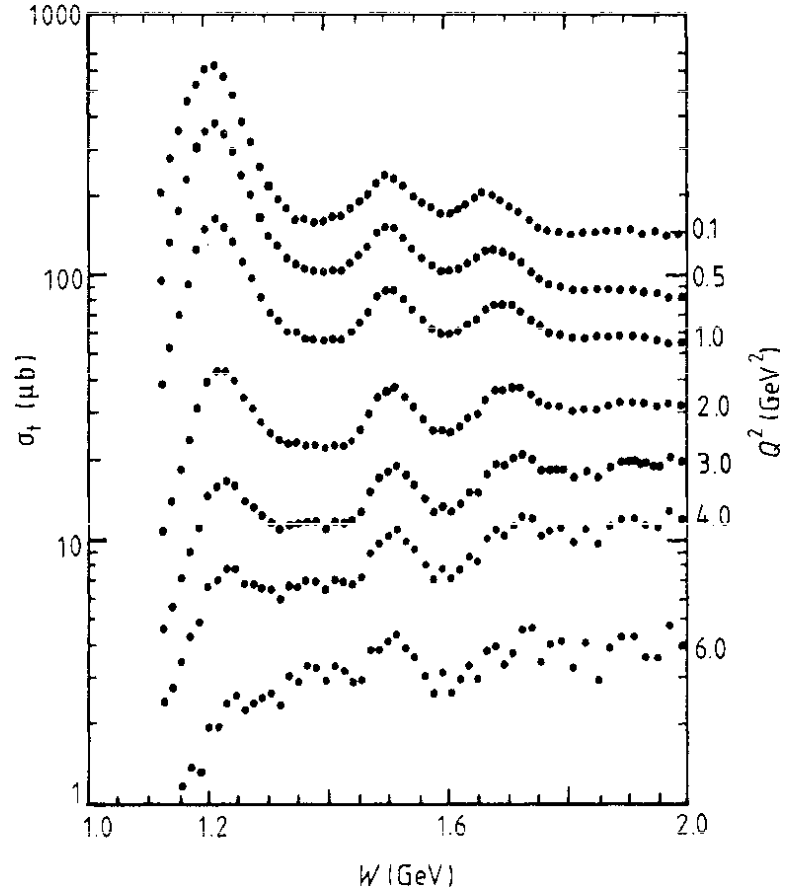
Figure 1.1: Virtual photon-proton cross sections for different Q^2 values clearly showing enhancement in the resonance regions [3]. The Δ region can clearly be seen, along with the second and third resonance regions.

ling the spin of the particles in the reaction, the dependence of the scattering on the relative spins of the particles involved can be measured. These measurements have been made possible by the very high duty factor, spin-polarized beams that are available at the Continuous Electron Beam Accelerator Facility (CEBAF) at the Thomas Jefferson National Accelerator Facility (TJNAF of Jefferson Lab), and advances in the use of spin polarized nuclear targets. Comparing the scattering of the electrons in various spin configurations allows the spin structure of the resonances to be measured.

One method that has been used by many experiments to look at the spin dependence of reactions is the measurement of spin asymmetries [4]. These asymmetries measure the relative cross section difference for different combinations of electron and nucleon spin. The measurement of these asymmetries is possible so long as the helicity of the electron and or target can be flipped, allowing different spin states to be compared while other aspects of the experiment remain the same. There are several advantages in measuring asymmetries, as opposed to total or differential cross sections; these will be discussed later.

The analysis described in this document is of the exclusive reaction $e^\uparrow p^\uparrow \rightarrow e\pi^+ n$. Exclusive pion production is especially useful for the study of the resonance region, since most of the proton resonances decay into $\pi^+ n$ with a very high probability. This analysis is of electron scattering data taken during the eg1b run, in experimental Hall B, at TJNAF, using the CEBAF Large Acceptance Spectrometer. The experiment used a polarized electron beam incident on a polarized nuclear target. The main goal of this analysis is to determine the double spin asymmetry in exclusive $ep \rightarrow e\pi^+ n$ scattering as a function of four different kinematic variables. As a secondary goal single spin asymmetries are also extracted. This has produced a large amount of new information that can help in the understanding of the spin structure of the resonances, acting as a constraint to theory and as a possible input to models.
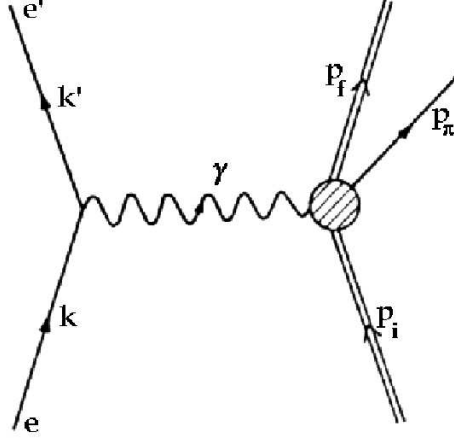
Figure 1.2: The scattering of the electron is approximated by the exchange of a single virtual photon.

1.2 Formalism

In order to describe the asymmetries, it is necessary to first define the coordinate system and momentum frame being used. In the energy scale of interest for this analysis, the electron scattering can be approximated by the exchange of a single virtual photon with four-momentum q (see Fig. 1.2. This is known as the OPE (one photon exchange) approximation and is a common choice in particle physics since the probability for a second photon to be exchange is suppressed by a factor of α^2.

In single pion electro-production, the reaction is described in terms of four kinematic variables, the invariant mass of the struck particle W, the four-momentum transfer q, and the angles associated with the pion. The angles θ^* and ϕ^* are the polar and azimuthal angle that the pion makes with respect to the direction of the four-momentum transfer and the electron scattering plane, in the rest frame of the pion and neutron system. These angles are shown in Fig. 1.4. The analysis is done in this momentum frame with the $\hat{z}$ direction being defined in the direction of the four-momentum transfer, the $\hat{y}$ defined as normal to the hadron scattering plane, and $\hat{x}$ being $\hat{y} \times \hat{z}$.
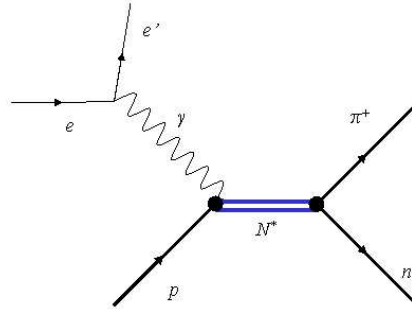
Figure 1.3: One diagram contributing to the ep→eπ$^+$n scattering. This is the reaction of interest for studying the resonances. The proton and virtual photon combine to form a resonance N*. This resonance then decays into a neutron and a π$^+$. There are other processes that contribute, so the scattering does not solely reflect the structure of the resonances.
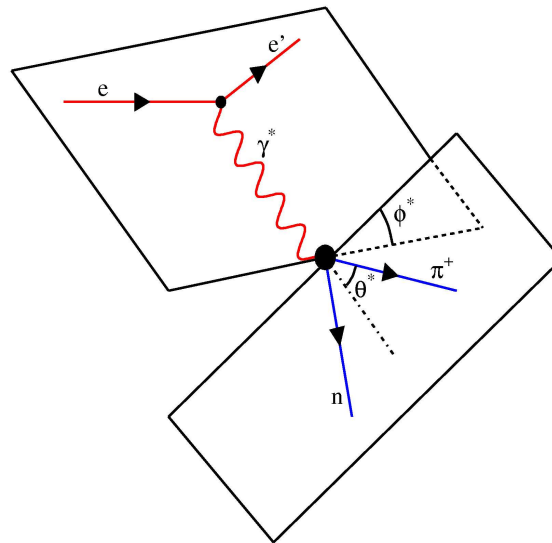
Figure 1.4: Drawing showing the definition of the angles θ^* and ϕ^*. There two angles define the direction the pion travels in relation to the four momentum transfer and the electron scattering plane.

The differential cross section for the production of a pion from electron scattering [5] off a nucleon is given in Eq. 1.1. The differential cross-section depends on kinematic factors (including an energy and momentum conserving delta function, the incoming electron momentum and energy, and the momentum and energy of the outgoing electron and pion), the current of the electron system, j_μ, and the current of the hadron system, J^μ.

$$
\begin{aligned}
d\sigma \ = \ & \frac{\epsilon_i}{k_i} \frac{m_e}{\epsilon_i} \frac{m_P}{E_i} \frac{m_e}{\epsilon_f} \frac{d^3\vec{k}_f}{(2\pi)^3} \frac{1}{2E_\pi} \frac{d^3\vec{p}_\pi}{(2\pi)^3} \frac{m_N}{E_f} \frac{d^3\vec{p}_f}{(2\pi)^3} (2\pi)^4 \\
* \ \ & \delta(p_i + q - p_\pi - p_f) \\
* \ \ & |<p_f, p_\pi|J^\mu|p_i> q^{-2} <k_f|j_\mu|k_i>|^2
\end{aligned}
$$

$$(1.1)$$

The matrix element in Eq. 1.1 can be rewritten, in the approximation of OPE, as the product of the leptonic tensor $\eta_{\mu\nu}$ and the hadronic tensor $W^{\mu\nu}$ [6]. The leptonic tensor is well known and can be combined with kinematic factors to produce the flux of virtual photons produced by the electron beam. This flux Γ is defined in Eq. 1.2. Defining the flux in this manner allows the cross section to be re-written as in Eq. 1.3 where $\frac{d\sigma_\nu}{d\Omega_\pi}$ is the virtual photon cross section which contains all of the information from the hadronic tensor.

$$\Gamma = \frac{\alpha}{2\pi^2} \frac{W^2 - m_p^2}{2m_p Q^2} \frac{E'}{E_0}$$

$$(1.2)$$

$$\frac{d\sigma}{dE' d\Omega_e d\Omega_\pi} = \Gamma \frac{d\sigma_\nu}{d\Omega_\pi}$$

$$(1.3)$$

In general, the virtual photon cross section is a function of the six response func-

tions [7] R_T, R_L, R_{LT}, R_{TT}, $R_{LT'}$, and $R_{TT'}$ as shown in Eq. 1.4.

$$\frac{d\sigma_\nu}{d\Omega_\pi} = \frac{|\vec{q}|}{q_\gamma^{CM}}[R_T + \epsilon_L R_L + \sqrt{2\epsilon_L(1+\epsilon)}R_{LT}\cos\phi^* + \epsilon R_{TT}\cos 2\phi^*] \qquad (1.4)$$

The L refers to the longitudinal component of the virtual photon polarization, the T refers to the transverse component, and the TT and LT terms are interference terms. The un-primed terms are from symmetric combinations of the longitudinal and transverse terms, while the primed terms are from anti-symmetric combinations. q_γ^{CM} is the energy that would be required for a real photon to excite a state with mass W. The degree of the transverse polarization of the photon is represented by ϵ, while ϵ_L is the longitudinal polarization of the photon.

$$\epsilon = \left(1 + \frac{2|\vec{q}|^2}{Q^2}\tan^2\frac{\theta_e}{2}\right)^{-1} \qquad (1.5)$$

$$\epsilon_L = \frac{Q^2}{\omega}\epsilon \qquad (1.6)$$

In the specific case of interest in this analysis, the projections of the response functions onto the polarization of the proton must be considered, in addition to the helicity of the electron. If the polarization of the proton target is defined in the same reference frame as mentioned previously, $\vec{P} = P_x\hat{x} + P_y\hat{y} + P_z\hat{z}$, then the virtual photon cross section can be written as in equation 1.7.

$$\begin{aligned}
\frac{d\sigma_\nu}{d\Omega_\pi} = & \frac{|\vec{q}|}{q_\gamma^{CM}}[R_T + P_y R_T^y + \epsilon_L(R_L + P_y R_L^y) \\
& + \sqrt{2\epsilon_L(1+\epsilon)}((R_{LT} + P_y R_{LT}^y)\cos\phi^* + (P_x R_{LT}^x + P_z R_{LT}^z)\sin\phi^*) \\
& + \epsilon((R_{TT} + P_y R_{TT}^y)\cos 2\phi^* + (P_x R_{TT}^x + P_z R_{TT}^z)\sin 2\phi^*)
\end{aligned} \qquad (1.7)$$

$$+ \quad h\sqrt{2\epsilon_L(1-\epsilon)}((R_{LT'} + P_y R_{LT'}^y)\sin\phi^* + (P_x R_{LT'}^x + P_z R_{LT'}^z)\cos\phi^*)$$

$$+ \quad h\sqrt{1-\epsilon^2}(P_x R_{TT'}^x + P_z R_{TT'}^z)]$$

The response functions can be written in terms of the Chew, Goldberger, Low, Nambu (CGLN) [8] amplitudes F_1, F_2, F_3, F_4, F_5, and F_6 as shown in Equations A.1 in Appendix A. The first four amplitudes represent the transverse current, while the last two represent the longitudinal current. The CGLN amplitudes can be expressed as a multi-pole decomposition of the derivative of Legendre polynomials as shown in Eq. 1.8 [9] where the terms $E_{l\pm}$ are electric terms, $M_{l\pm}$ are magnetic terms, and $L_{l\pm}$ are longitudinal terms. The advantage of being able to express the response functions in terms of multi-poles is that it allows for comparisons to be made to the results of different experiments and phenomenological models even if they do not contain much or any data specifically on the measurement of ep→eπ⁺n in the case of a polarized electron and a polarized proton. So long as data on the same multi-pole terms exist, then the comparison can be made.

$$
\begin{aligned}
F_1 &= \sum_{l\geq 1}[(lM_{l+} + E_{l+})]P'_{l+1} + [(l+1)M_{l-} + E_{l-}P'_{l-1}] \\
F_2 &= \sum_{l\geq 1}[(l+1)M_{l+} + lM_{l-}]P'_l \\
F_3 &= \sum_{l\geq 1}[(E_{l+} - M_{l+})P''_{l+1} + (E_{l-} + M_{l-})P''_{l-1}] \\
F_4 &= \sum_{l\geq 2}[M_{l+} - M_{l-} - E_{l+} - E_{l-}]P''_l \\
F_5 &= \sum_{l\geq 0}[(l+1)L_{l+}P'_{l+1} - lL_{l-}P'_{l-1}] \\
F_6 &= \sum_{l\geq 1}[lL_{l-} - (l+1)L_{l+}]P'_l
\end{aligned}
\tag{1.8}
$$

Alternatively. the response function can be written in terms of helicity amplitudes,

H_1, H_2, H_3, H_4, H_5, and H_6 as originally defined in [10] as shown in Eq. A.2 in Appendix A. The helicity amplitudes represent the probability to transfer from an initial helicity state to a final helicity state. Note that there are only two possible final states, corresponding to the spin of the neutron in the final state, since the pion is a spin zero particle. For the case of exclusive pion electro-production, there are six independent helicity amplitudes [11] shown in Eq. 1.9. The first four amplitudes represent the four different possible combinations of initial and final state nucleon polarization for transversely polarized photons. It is important to note that the final two amplitudes depend on the longitudinal polarization of the virtual photon and are therefore only present in the case of electro-production. The helicity amplitudes can be expressed themselves in terms of CGLN amplitudes and therefore multi-poles.

$$
\begin{aligned}
H &= <\lambda_\pi, \lambda_f | T | \lambda_\gamma, \lambda_i > \\
H_1 &= <0, \frac{1}{2} | T | 1, \frac{1}{2} > \\
H_2 &= <0, \frac{1}{2} | T | 1, -\frac{1}{2} > \\
H_3 &= <0, -\frac{1}{2} | T | 1, \frac{1}{2} > \\
H_4 &= <0, -\frac{1}{2} | T | 1, -\frac{1}{2} > \\
H_5 &= <0, \frac{1}{2} | T | 0, +\frac{1}{2} > \\
H_6 &= <0, \frac{1}{2} | T | 0, +\frac{1}{2} >
\end{aligned}
\tag{1.9}
$$

In the case of the eg1b run period, the target was polarized parallel or anti-parallel to momentum of the electron beam. The $\hat{x}$, $\hat{y}$, and $\hat{z}$ components of the target polarization can the be written in terms of the target polarization in the laboratory system, and the angles ϕ^*, as mentioned earlier, and θ_γ, which is the angle between

the virtual photon and the beam line (Eq. 1.10). The cross section can then be re-written in a new form that takes this into account (Eq. 1.11).

$$
\begin{aligned}
P_x &= P_T \sin\theta_\gamma \cos\phi^* \\
P_y &= -P_T \sin\theta_\gamma \sin\phi^* \\
P_z &= P_T \cos\theta_\gamma
\end{aligned}
\tag{1.10}
$$

$$
\begin{aligned}
\frac{d\sigma_\nu}{d\Omega_\pi} =\ & \frac{|\vec{q}|}{q_\gamma^{CM}}\{R_T - P_T \sin\theta_\gamma \sin\phi^* R_T^y + \epsilon_L(R_L - P_T \sin\theta_\gamma \sin\phi^* R_L^y) \\
+\ & \sqrt{2\epsilon_L(1+\epsilon)}[(R_{LT} - P_T \sin\theta_\gamma \sin\phi^* R_{LT}^y)\cos\phi^* \\
+\ & (P_T \sin\theta_\gamma \cos\phi^* R_{LT}^x + P_T \cos\theta_\gamma R_{LT}^z)\sin\phi^*] \\
+\ & \epsilon[(R_{TT} - P_T \sin\theta_\gamma \sin\phi^* R_{TT}^y)\cos 2\phi^* \\
+\ & (P_T \sin\theta_\gamma \cos\phi^* R_{TT}^x + P_T \cos\theta_\gamma R_{TT}^z)\sin 2\phi^*] \\
+\ & h\sqrt{2\epsilon_L(1-\epsilon)}[(R_{LT'} - P_T \sin\theta_\gamma \sin\phi^* R_{LT'}^y)\sin\phi^* \\
+\ & (P_T \sin\theta_\gamma \cos\phi^* R_{LT'}^x + P_T \cos\theta_\gamma R_{LT'}^z)\cos\phi^*] \\
+\ & h\sqrt{1-\epsilon^2}(P_T \sin\theta_\gamma \cos\phi^* R_{TT'}^x + P_T \cos\theta_\gamma R_{TT'}^z)\}
\end{aligned}
\tag{1.11}
$$

The cross section has four distinct parts, one that is independent of target polarization and beam helicity, one that depends on beam helicity, one that depends on target polarization, and one that depends both on beam helicity and target polarization. It is natural to write the cross section in these terms as shown in Eq. 1.12. In this case, P_B is the polarization of the incident electron beam, and P_T is the polarization of the target.

$$\sigma = \sigma_0 + P_B \sigma_e + P_T \sigma_t - P_B P_T \sigma_{et} \tag{1.12}$$

where

$$\sigma_0 = \frac{|\vec{q}|}{q_\gamma^{CM}} [R_T + \epsilon_L R_L + \sqrt{2\epsilon_L(1+\epsilon)} R_{LT} \cos \phi^* + \epsilon R_{TT} \cos 2\phi^*], \tag{1.13}$$

$$\sigma_e = \frac{|\vec{q}|}{q_\gamma^{CM}} \sqrt{2\epsilon_L(1-\epsilon)} R_{LT'} sin\phi^*, \tag{1.14}$$

$$\begin{aligned}
\sigma_t &= \frac{|\vec{q}|}{q_\gamma^{CM}} [\epsilon(R_{TT}^x \sin \theta_\gamma \cos \phi^* + R_{TT}^z \cos \theta_\gamma) \sin 2\phi^* \\
&\quad - \epsilon R_{TT}^y \sin \theta_\gamma \sin \phi^* \cos 2\phi^* \\
&\quad + \sqrt{2\epsilon_L(1+\epsilon)}(R_{LT}^x \sin \theta_\gamma \cos \phi^* + R_{LT}^z \cos \theta_\gamma) \sin \phi^* \\
&\quad - \sqrt{2\epsilon_L(1+\epsilon)} R_{LT}^y \sin \theta_\gamma \sin \phi^* \cos \phi^* \\
&\quad - (R_T^y + \epsilon_L R_L^y) \sin \theta_\gamma \sin \phi^*],
\end{aligned} \tag{1.15}$$

and

$$\begin{aligned}
\sigma_{et} &= \frac{|\vec{q}|}{q_\gamma^{CM}} [\sqrt{2\epsilon_L(1-\epsilon)}(R_{LT'}^x \sin \theta_\gamma \cos \phi^* + R_{LT'}^z \cos \theta_\gamma) \cos \phi^* \\
&\quad - \sqrt{2\epsilon_L(1-\epsilon)}(R_{LT'}^y \sin \theta_\gamma \sin \phi^* \sin \phi^*)) \\
&\quad + \sqrt{1-\epsilon^2}(R_{TT'}^x \sin \theta_\gamma \cos \phi^* + R_{TT'}^z \cos \theta_\gamma)].
\end{aligned} \tag{1.16}$$

The different portions of the cross section can be separated from each other in different ways. Particularly, the angular dependence of the cross section can be mea-

sured for a specific spin state. As an example, the σ_e component to the cross section clearly has a $\sin \phi^*$ dependence (this $\sin \phi^*$ dependence actually displays one of the traditional difficulties in these sorts of measurements, as there is often no way to make an out of plane measurement using traditional, small acceptance detectors). In addition, the cross section could be measured for several different combinations of beam and target polarization. The ideal choice would be to do both, allowing for the largest number of observables to be extracted. That is the procedure in this analysis.

1.3 Asymmetries

This thesis will concern itself only with the analysis of the spin asymmetries, as opposed to direct measurement of the cross sections. There are two main reasons for this choice. The first is that, in the asymmetries, the measurement is of the interference between polarized and unpolarized terms. This has the effect of amplifying the relatively small polarization dependent term by the large polarization independent terms. The second reason is more of an experimental consideration. In asymmetries, many of the factors that need to be known very well in order to calculate a cross section cancel in the ratio. This means that the asymmetry measurement is not generally dependent on acceptance, detector efficiency, or luminosity so long as these factors are not changing over time in a way that results in different values for the different spin configurations. Since these factors can all have large systematic errors associated with their determination, the ability to make a measurement of the spin dependence of the cross section independent of these factors can greatly lower the total systematic error for the experiment.

Asymmetries are constructed by comparing the total count rates in different helicity configurations. The simplest asymmetry, in the case of an un-polarized target and

a beam with a polarization of 100%, and identical luminosities is shown in Eq. 1.17. $N_\uparrow$ represent the number of counts while the beam had positive helicity, while $N_\downarrow$ is the number of counts when the beam had a negative helicity. The reversal of the beam helicity allows the asymmetry to be constructed.

$$A_\| = \frac{N_\uparrow - N_\downarrow}{N_\uparrow + N_\downarrow} \tag{1.17}$$

In the eg1b run, both a polarized beam and a polarized target were used. This allowed for both the beam and target polarization to be reversed. The reversal of both of these allows for the construction of three independent asymmetries. These asymmetries can be related to the ratio of different spin dependent parts of the cross section the spin independent parts of the cross section. Equations 1.18-1.20 show the relevant asymmetries with the assumption that the beam and the target both have 100% polarization.

$$A_e = \frac{\sigma_e}{\sigma_0} = \frac{(\sigma_{++} - \sigma_{-+}) + (\sigma_{+-} - \sigma_{--})}{(\sigma_{++} + \sigma_{-+}) + (\sigma_{+-} + \sigma_{--})} \tag{1.18}$$

$$A_t = \frac{\sigma_t}{\sigma_0} = \frac{(\sigma_{++} + \sigma_{-+}) - (\sigma_{+-} + \sigma_{--})}{(\sigma_{++} + \sigma_{-+}) + (\sigma_{+-} + \sigma_{--})} \tag{1.19}$$

$$A_{et} = \frac{\sigma_{et}}{\sigma_0} = \frac{(\sigma_{-+} - \sigma_{++}) + (\sigma_{+-} - \sigma_{--})}{(\sigma_{++} + \sigma_{-+}) + (\sigma_{+-} + \sigma_{--})} \tag{1.20}$$

where $+$ and $-$ sub-scripts are the sign of the beam (first sub-script) and target (second sub-script) polarizations.

The main goal of this analysis is to extract A_{et} in the region of the resonances as a function of the kinematic variables mentioned earlier.

1.4 Expectation of Results for Asymmetries

1.4.1 σ_{et} from eg1a

The eg1a run, a previous run in Hall B using a similar configuration and the same target as the eg1b run, took both inclusive and exclusive electron scattering data [12][13][14]. The data from this run have been used to analyze the double spin asymmetry from π^+ electro-production[14]. The results of the eg1a analysis are shown in Fig.s 1.5 and 1.6. Due to low statistics, in the analysis of the eg1a data it was necessary to integrate over at least one of the aforementioned kinematic variables. In this case, ϕ^* was chosen since the behavior of the asymmetry as a function of this variable is well known. In addition to losing information about the ϕ^* dependence of the asymmetry, which as earlier noted helps in the separation of the different response functions, this need to integrate adds the requirement for an acceptance correction in ϕ^*. The added statistics of the eg1b run should allow the asymmetry to be measured in much smaller bins in W, which would allow for increased sensitivity to the resonances. Also, the statistics are high enough that it is not necessary to integrate over any of the kinematic variables, eliminating the need for any acceptance correction and preserving the information about the ϕ^* dependence of the asymmetry. Additionally, the eg1b run took data at two additional beam energies, compared to the eg1a run. This means that the kinematic coverage in W and Q^2 was extended.

1.4.2 $\sigma_{LT'}$

Since the part of the cross-section that depends only on the beam polarization requires only a polarized beam, and no polarized target, there are a greater number of measurements. Some of these measurements have been done with very high statistics,
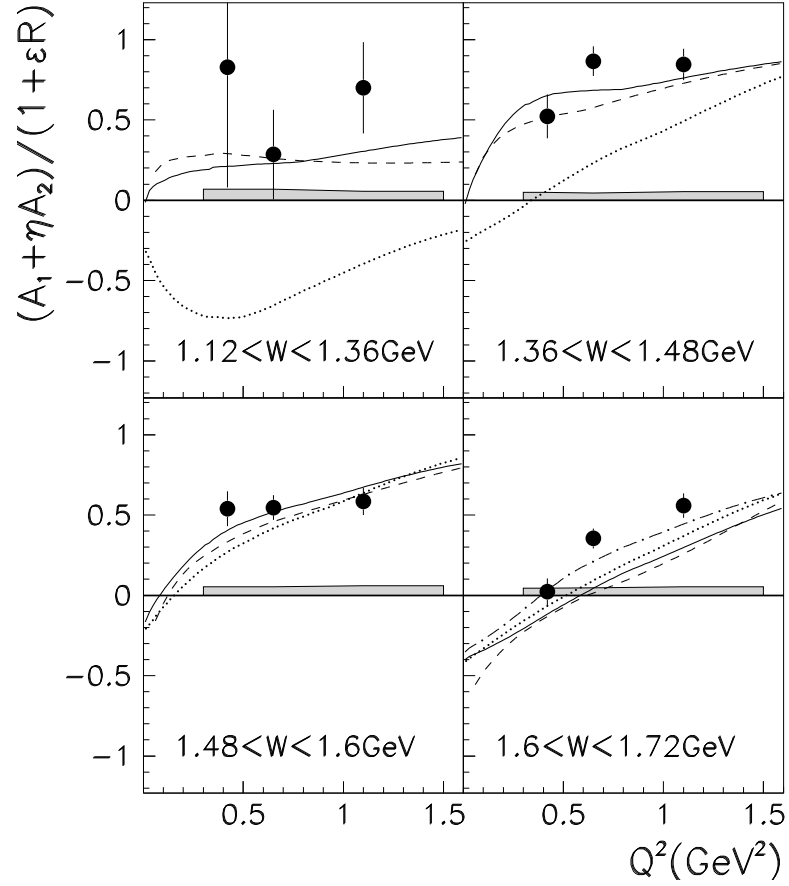
Figure 1.5: Double spin asymmetry of ep→eπ$^+$n as a function of Q^2 as measured by the eg1a experiment [14]. A comparison is shown between the data and MAID 2000 [9] and the AO [15] model.
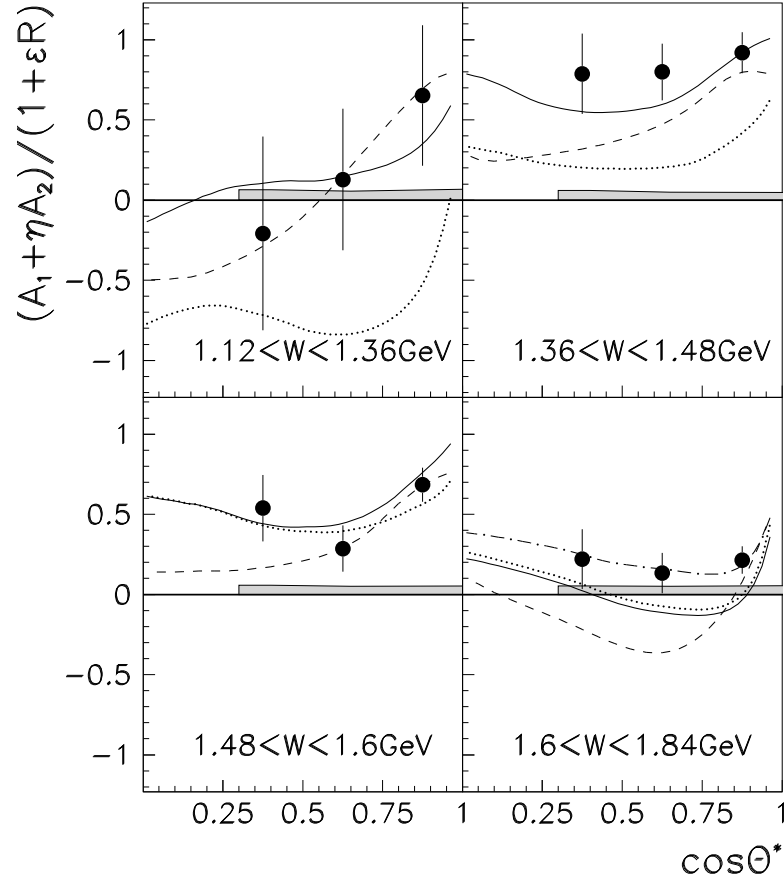
Figure 1.6: Double spin asymmetry of ep→eπ⁺n as a function of θ^* as measured by the eg1a experiment [14]. Again, the comparison is shown between the data and MAID 2000 [9] and the AO model [15].

as the limit on the beam current that can be used in an experiment that has a polarized target is often the ability of the target itself to withstand the flux of electrons. The lack of a polarized target allows for a much higher flux of electrons to be used, meaning greater statistics can be accumulated in the same amount of time. In the event that there is zero target polarization, Eq. 1.12 becomes Eq. 1.21. Also, from Eq. 1.14, it can be seen that σ_e depends only on the angle ϕ^*, as previously defined, and the single response function $R_{LT'}$. The cross section in this case is often rewritten in terms of $\sigma_{LT'}$ (Eq. 1.22), which is analogous to $R_{LT'}$.

$$\sigma = \sigma_0 + P_B \sigma_e \tag{1.21}$$

$$\sigma = \frac{p_\pi^*}{k_\gamma^*}(\sigma_0 + h\sqrt{2\epsilon_L(1-\epsilon)}\sigma_{LT'} \sin\theta^* \sin\phi^*) \tag{1.22}$$

where p_π^* is the pion momentum in the center of mass frame and k_γ^* is the photon equivilent energy.

Previous experiments using CLAS and the polarized beam at Jefferson Lab have measured $\sigma_{LT'}$ in different resonance regions. This has been done by measuring an asymmetry much like the one shown in Eq. 1.18. Since there are only two helicity states present, the asymmetry for this case is written as in equation 1.23. The additional helicity states that are present in Eq. 1.18 are needed to cancel out the contributions from the double spin and target spin asymmetries, which are obviously not present in the case of unpolarized targets.

$$A_{LT'} = \frac{1}{P_B}\frac{\sigma_\uparrow - \sigma_\downarrow}{\sigma_\uparrow - \sigma_\downarrow} = \frac{1}{P_B}\frac{N_\uparrow - N_\downarrow}{N_\uparrow - N_\downarrow} \tag{1.23}$$

Data taken with CLAS has been used to determine $A_{LT'}$ and $\sigma_{LT'}$ in the Δ
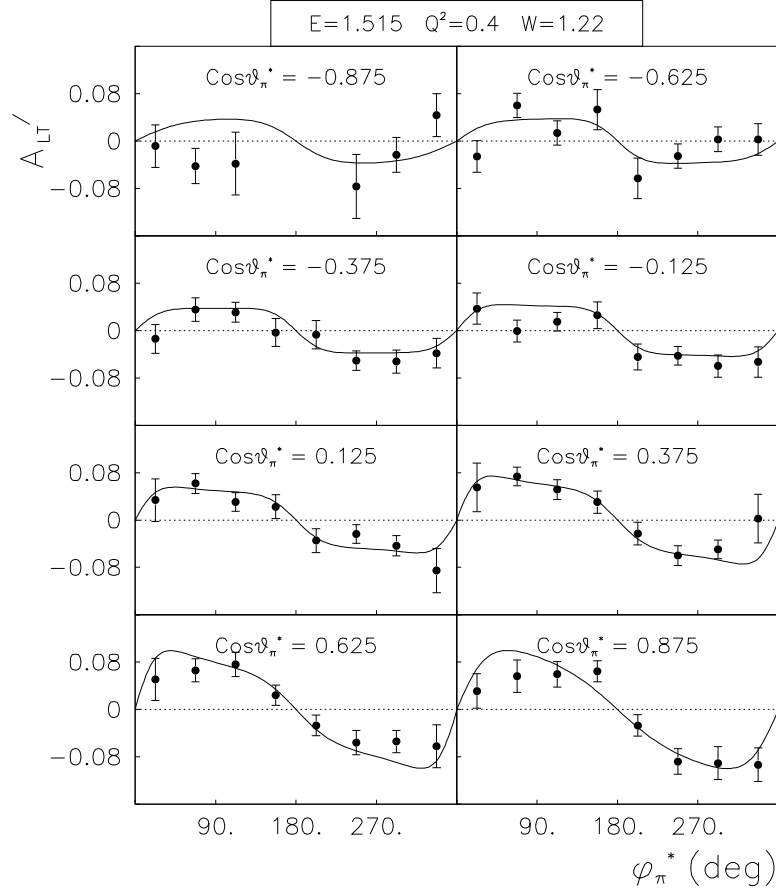
Figure 1.7: Beam spin asymmetry $A_{LT'}$ of ep→eπ⁺n as a function of ϕ^* for a fixed value of W and Q^2 in several bins in $\cos\theta^*$ [16]. Comparison is to the MAID2000 model [9].

resonance region [16] and the second and third resonance regions [17]. $\sigma_{LT'}$ was extracted from $A_{LT'}$ using the relation shown in Eq. 1.24 and values for σ_0 obtained in the same experiment [18]. The result for $A_{LT'}$ [16] in the region of the Δ resonance is shown in Fig. 1.7. Extracted values of $\sigma_{LT'}$ [17] are shown in Fig. 1.8.

$$A_{LT'} = \frac{\sqrt{2\epsilon_L(1-\epsilon)}\sigma_{LT'}\sin\theta^*\sin\phi^*}{\sigma_0} \tag{1.24}$$
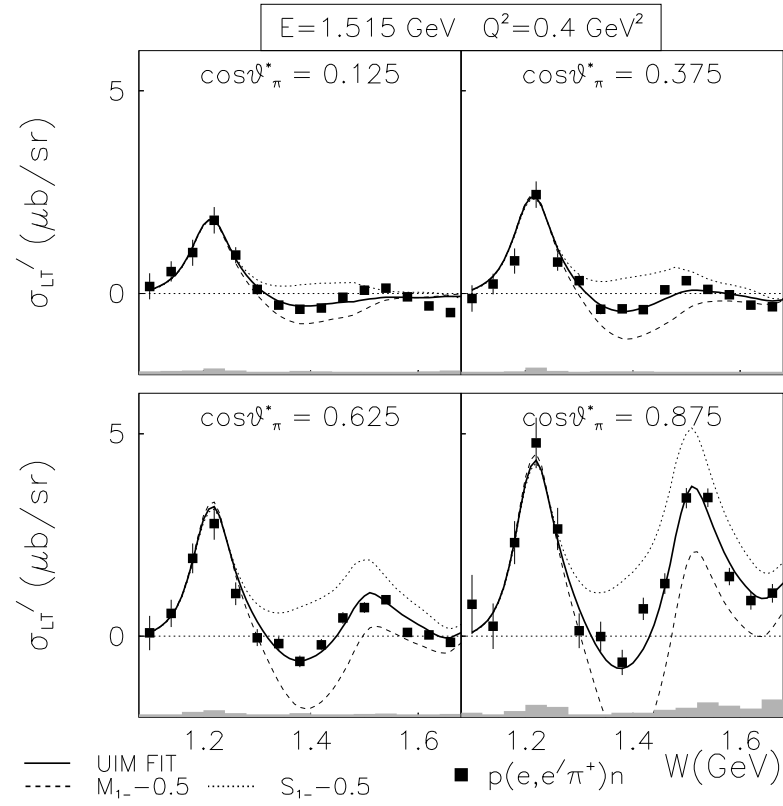
Figure 1.8: $\sigma_{LT'}$ of W for fixed values of Q^2 [17].

1.4.3   Asymmetries from Models

While very little data exists on the double spin asymmetries themselves, there are models that use other scattering data from various types of experiments to predict, among other things, the polarized response functions and the asymmetries for pion electro-production. One example of this is MAID [9], which is a model for pion photo- and electro-production. MAID is an isobar model with Breit-Wigner amplitudes being used to estimate the contributions from the resonances, and with backgrounds calculated from Born diagrams. The model can be used to predict the multipole terms (like those in equation 1.8) and therefore any number of polarization observables, such as the double spin asymmetry. The strength of different multipole contributions from different resonances can be changed to estimate the effect of these resonances on the asymmetry. While MAID is interesting for comparing to the current analysis, more important is the possible impact of this analysis on MAID, as information on the double spin asymmetries could be directly used to help model the multipoles. Other models of the resonances could also benefit from more data on the double spin asymmetry.

For an overview of data from a variety of reactions which give insight into the structure of the resonances and the impact of this data on various models, see Ref. [19].

1.5   eg1b

The eg1b experimental run was designed as an extension of the eg1 run period. The eg1b experiment took data at four different beam energies: 1.6 GeV, 2.3 GeV, 4.2 GeV, and 5.6 GeV. The primary goal of the eg1b experiment was to measure the structure function g_1 for the proton and neutron [20][21]. This is done by measuring the spin asymmetry for inclusive electron scattering. In the case of inclusive scatter-

ing, only the orientations of the electron and proton spins relative to each other have any influence on the asymmetry, so the asymmetry can be constructed as in equation 1.25:

$$A_{\parallel} = \frac{N_{\downarrow\uparrow} - N_{\uparrow\uparrow}}{N_{\downarrow\uparrow} + N_{\uparrow\uparrow}} \qquad (1.25)$$

where $N_{\downarrow\uparrow}$ is the number of counts when the target and the beam polarizations were anti-parallel, and $N_{\uparrow\uparrow}$ is the number of counts when the spins are parallel. In inclusive scattering, reversal of the target polarization is not necessary to conduct the experiment, although it is done in order to limit the systematic errors that can be associated with the target polarization measurement.

$A_{\parallel}$ is related to the physics asymmetries A_1 and A_2 by the relation shown in Eq. 1.26. The A_1 and A_2 asymmetries can be expressed in terms of the structure functions g_1 and g_2 by the relation shown in equation 1.29. The analysis of the inclusive reaction for the 1.6 and 5.6 GeV data has been completed and the analysis of the other beam energies is underway.

$$A_{\parallel} = D(A_1 + \eta A_2) \qquad (1.26)$$

where

$$\eta = \frac{\frac{\epsilon\sqrt{Q^2}}{E'}}{1 - \frac{\epsilon E'}{E}} \qquad (1.27)$$

and

$$D = \frac{1 - \frac{\epsilon E'}{E}}{1 + \epsilon R}. \qquad (1.28)$$

$$A_1 = \frac{g_1 - \gamma^2 g_2}{F_1}$$

$$A_2 = \frac{\gamma(g_1 + g_2)}{F_1}$$

(1.29)

As mentioned previously, this thesis uses the same data that are used for the inclusive analysis, but it uses the information that the CLAS detector has about the other particles in the reaction, specifically the π^+. This is the advantage of using a detector like CLAS, which is capable of measuring events with high multiplicity and has a very large acceptance.

In this thesis, the apparatus used in the experiment will be discussed, with special attention given to the polarized nuclear target. The data analysis, which contains contributions from many members of the eg1b analysis group, will also be described. The results of the analysis will be presented, sources of systematic error will be discussed and the consequences of the asymmetry data will be explored. The data are of exceptional quality, having been taken with beam and target polarization of 70% or greater. The high polarizations of the beam and target combined with the large amount of data and the large acceptance of CLAS gives an opportunity to measure the double spin asymmetry for ep→eπ^+n with an unparalleled level of accuracy as an independent function of all four relevant kinematic variables. This has the potential to add greatly to the understanding of the spin structure of the resonances.

Chapter 2

CEBAF and CLAS

2.1 Introduction

The eg1b experiment used the existing electron beam and detector package for experimental Hall B at the Thomas Jefferson National Accelerator Facility. The electron accelerator (CEBAF) and the detector (CLAS), will be briefly described, with emphasis on the aspects that are essential to the analysis of the exclusive π^+ double spin asymmetry.

2.2 CEBAF

CEBAF (Continuous Electron Beam Accelerator Facility) produces a longitudinally polarized electron beam. The accelerator is a race track design (see Fig. 2.1), with two linear accelerators connected by recirculating arcs [22]. The electrons can circulate in the race track as many as five times, resulting in an electron energy as high as 6 GeV. The accelerator is of a continuous wave type, which means that it has a much higher duty factor than traditional accelerators. This is accomplished by the use of
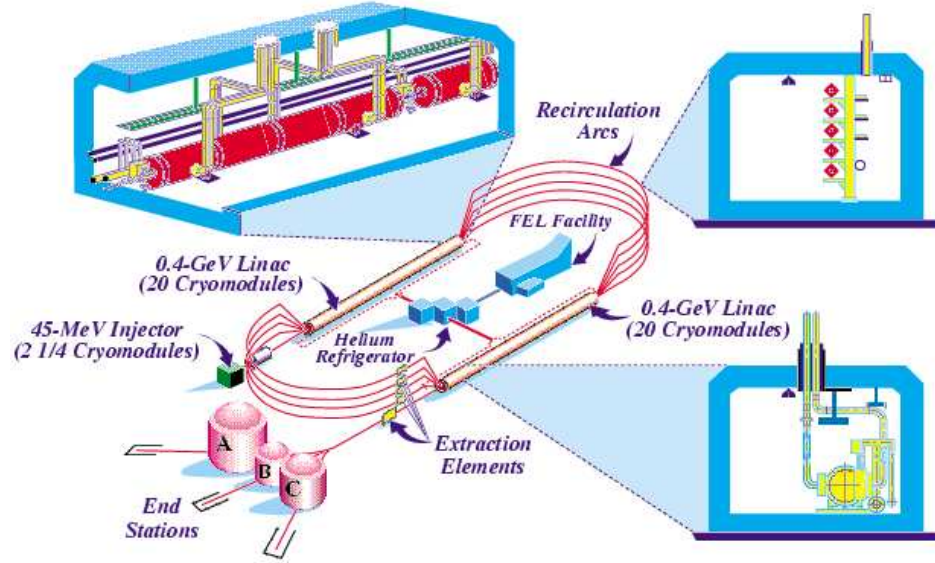
Figure 2.1: Diagram of The CEBAF accelerator at Jefferson Lab.

specially designed five cell, super-conducting RF cavities, first developed at Cornell.

The polarized electrons are produced by shining a laser on a GaAs cathode. By using circularly polarized laser light to produce the electrons, they are given a linear polarization. Historically, pure GaAs cathodes were used. These had the drawback that the maximum electron polarization which could be achieved was 50%. This is a consequence of an energy degeneracy in the electron states which are excited in the cathode by the laser. The heavy hole (HH) valance band electrons (the heavy hole valance band is the band with a higher effective mass) are excited from a $m = 3/2$ state to a $m = 1/2$ in the conduction band by a $m = -1$ circularly polarized photon. The light hole (LH) valance band electrons (the light hole valance band is the band with a lower effective mass) however, have the exact small energy gap from the valance up to the conduction band, but in the LH case, the electrons go from $m = 1/2$ to $m = -1/2$ with excitation by a $m = -1$ photon. The polarization of 50% results from excitation of HH band being three times more likely than LH. This degeneracy
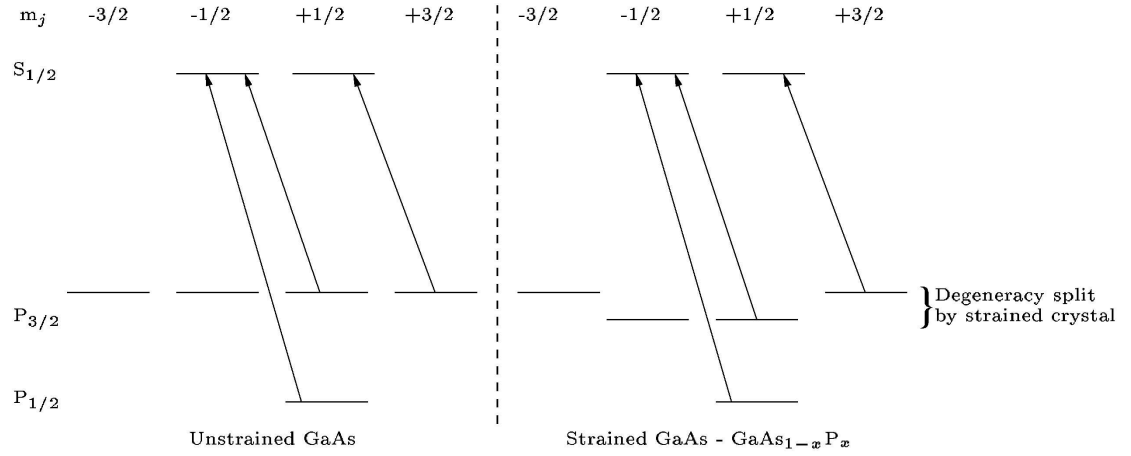
Figure 2.2: Splitting of the degeneracy by the straining of the GaAs lattice. The conduction band is shown on top, and the valance band is shown on bottom.

can be broken by straining the GaAs lattice [23]. This is done by growing the GaAs lattice on a substrate of $GaAs_{0.72}P_{0.28}$. At the interface between the two lattices, a strain is created on the GaAs due to the smaller lattice spacing of the substrate. This strain lifts the degeneracy in the excitations to the HH and LH states for electrons (see the drawing in Fig. 2.2). By selecting the wavelength of the laser to provide just enough energy to excite the transition from the valence $m = 3/2$ state to the conduction $m = 1/2$ state, but not from the valence $m = 1/2$ state to the conduction $m = -1/2$ state, polarizations greatly in excess of the 50% maximum associated with pure GaAs can be achieved. In the case of the source used for CEBAF, the electron polarization can be 80% or greater. All of these transitions are valid for light with $m = 1$ or equal $m = -1$, meaning that either polarization of light can be used to produce either polarization of electron.

The spin of the electrons is affected by the beam optics, particularly the bending magnets in the recirculation arcs due to the precession of the electron spins in the presence of magnetic fields. In order to make sure that the polarization of the electrons

that enter the experimental halls is along the beam direction, the orientation of the spins can be adjusted as they enter the beam line using a Wein filter to precess the spins of the electrons. The Wein filter consists of perpendicular electric and magnetic fields which are in turn perpendicular to the direction of the beam. The magnetic field causes the electron spins to precess, while the perpendicular electric field preserves the momentum of the electrons by compensating for the deflection which would be caused by the magnetic field.

The helicity of the electrons can be changed quickly by using a Pockel cell to reverse the helicity of the light and therefore the helicity of the electrons. The helicity of the light can also be reversed systematically by the insertion of a half-wave plate. Both of these methods are used, the combination of fast and slow reversals serving to minimize the systematic errors that can be caused by differences in the beam between one helicity state or the other, which might not otherwise be properly taken into account.

The electron beam is delivered to three experimental halls, A, B and C. Hall A and Hall C each contain two spectrometers which can be positioned at variety of angles to perform experiments at different kinematic settings. Hall B has CLAS (CEBAF Large Acceptance Spectrometer), a nearly 4π acceptance detector designed to work with an electron or tagged photon beam. The eg1b run occurred in experimental Hall B and used the CLAS detector. Much of the beam line equipment in Hall B will be discussed, and are shown in Fig. 2.3.

At the upstream side of the hall is a Møller polarimeter, which is used to determine the electron polarization. The Møller polarimeter consists of a 20 μm iron foil in a magnetic field, generated by a Helmholtz pair, placed in the beam line. The free electrons in the iron polarize in the magnetic field. Electrons scatter off of the foil, sometimes scattering off of these polarized electrons. The scattered and recoil elec-

trons are deflected away from the primary electron beam by means of a quadrupole magnet and are detected in coincidence by two scintillation counters down stream. The measurement of both of the electrons in coincidence allows for a clean separation between electrons from Rosenbluth scattering and electrons from Møller scattering. By comparing the asymmetry in counts, from when the beam is polarized parallel to the direction of momentum of the beam versus anti-parallel to it, to the known asymmetry for polarized electron-electron (Møller) scattering, the polarization of the electron beam can be determined. The asymmetry for Møller scattering is a well known function [24] of the electron polarizations and the scattering angle, shown in Eq. 2.1. The $\hat{y}$ direction is chosen such that the target polarization lies in the $\hat{y} - \hat{z}$ plane ($\hat{z}$ is along the beam), P is the beam polarization, and P^T is the target polarization.

$$A = \frac{\sin^2 \theta}{(4 - \sin^2 \theta)^2}(\sin^2 \theta P_y P_y^T - (8 - \sin^2 \theta)P_z P_z^T) \qquad (2.1)$$

There are also a series of beam position monitors that are used to make sure that the beam passes through the center of the target, and the beam raster magnets, (which are essential to the operation of a solid polarized target) two pairs of dipole magnets cause the location of the beam spot to move over the face of the target.

Downstream of CLAS is a Faraday cup, which is used to determine the total number of electrons that have been delivered to the Hall for any given time period. This is essential for the measurement of asymmetries, as it allows for normalization of the counts by the luminosity.

Several pieces of information are sent from the accelerator which are necessary for the analysis of the data. The most important of these are the helicity pulse and the RF signal. The RF signal tells the Hall when electrons are being sent into it (they are sent
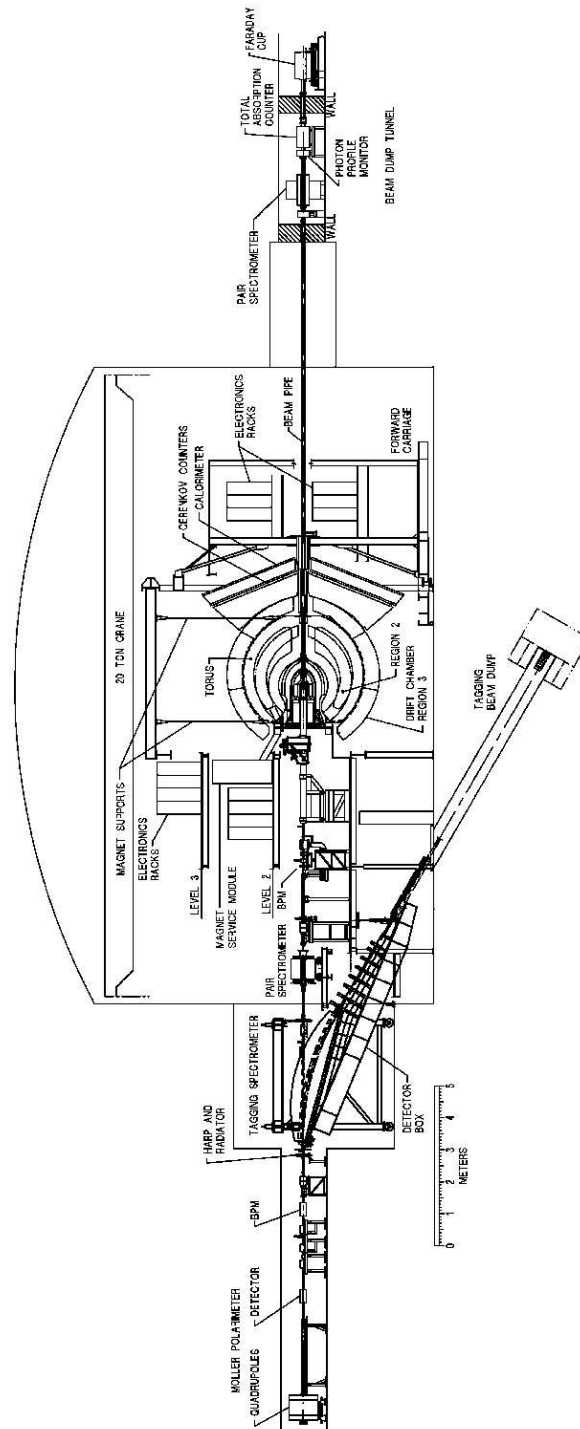
Figure 2.3: A drawing of up and down stream beam-line components of Hall B, along with CLAS. Prominent are the tagger system up stream of CLAS and the Faraday cup and beam dump down stream

to the three different halls in groups). This information is useful in determining the start time for events, so that different particles are properly grouped into appropriate events. The second piece of information is the helicity synchronization pulse. This is actually two pulses, one of which tells when the helicity state is being changed, and one that tells what the helicity state is. Both pulses are necessary to determine the helicity state of the beam, since the helicity of the beam is changed in a pseudo-random pattern on a pair-by-pair basis. The first helicity state of a pair is set at random, while the second state is always the complement of the first state. This guarantees an equal number of pulses for each state, as well as keeping complementary pulses close to each other in time to help cancel any time dependent effects. Additionally the pseudo-random nature ensures that the pairs of helicity states are not always in the same order.

2.3 CLAS

CLAS is the CEBAF Large Acceptance Spectrometer [25]. This is the primary detector package used in Hall B at Jefferson Lab. It was designed to be used in a variety of experiments, using both electron and photon beams, and with several types of targets, including polarized nucleon targets. The individual detector elements will be discussed, as will the particle tracking system.

2.3.1 Torus

In order to measure the momentum of charged particles, it is necessary to analyze their trajectories in the presence of a magnetic field. In the case of CLAS, the magnetic field is supplied by six super-conducting coils arranged in a toroidal configuration about the beam line as shown in Fig. 2.4. This divides the detector into six identical
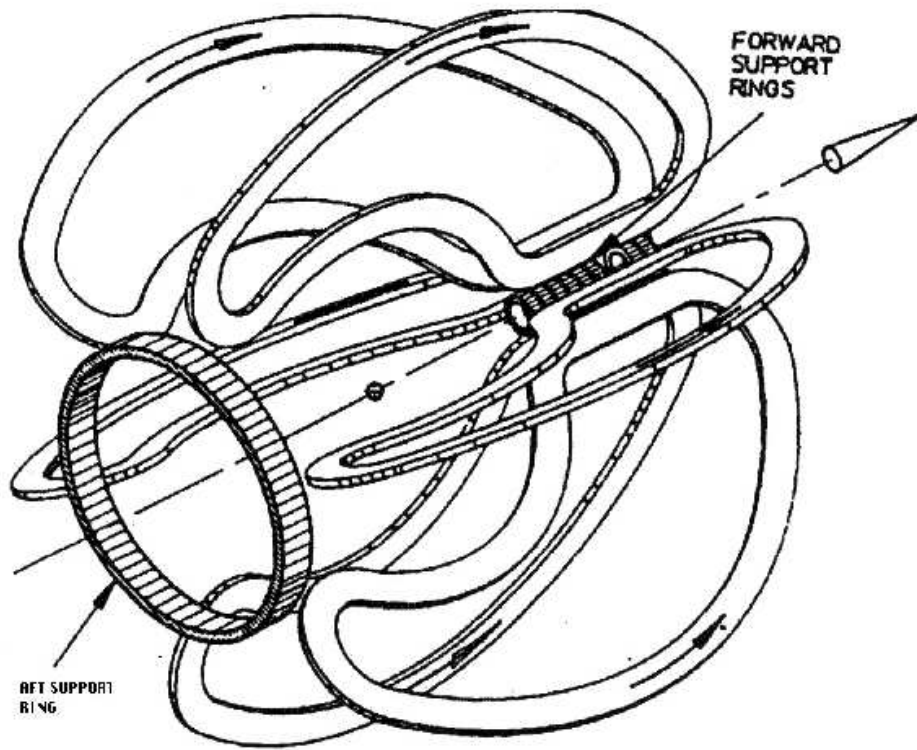
Figure 2.4: Sketch of the CLAS torus magnet. When energized, the forces exerted on each coil by its neighbors is considerable, hence the presence of the support rings.

sectors, each in a different azimuthal region. These coils supply a magnetic field that points in the ϕ direction (azimuthal to the beam). The toroidal configuration is used so that a field free region is preserved around the center axis of CLAS, allowing for operation of a polarized target. The field generated by these magnets is directly proportional to the current supplied.

The coils themselves have a very specific shape. They are engineered to keep the magnetic field as close as possible to zero around the center axis of CLAS, thereby allowing polarized targets to be used.

For the eg1b experiment the current in the torus was changed depending on the beam energy, lower current corresponding to lower energy. This allows the maximum acceptance of the spectrometer to be used for each setting. In addition, data was

taken at several energy settings with the torus polarity reversed (the nominal torus currents used for each energy setting are shown in Table 2.1). The standard configuration in which CLAS is used is such that the negatively charged particles are bent in toward the beam line. When the torus polarity is reversed, the negatively charged particles are bent away from the beam line. The result is an altered kinematic coverage (low Q^2 events when the electron is produced at a low angle can be detected because the electron trajectory is bent out into the detector, whereas in the standard configuration the electrons would have been bent into the beam line and therefor not be detected) and a change in the efficiency of the detector (since some of the detector elements are not optimized for the out-bending electron configuration). In addition to changing the kinematic coverage, it is often advantageous to change the torus polarity in order to study the positron rates. The positron rates can be used to estimate the contamination of the scattered electron counts by counts from electrons from pair production of e^+e^-. Comparing positron and electron rates from opposite torus polarities cancels the detector contributions to the ratio of electron to positron production. This correction to the electron counting rates is unimportant in the analysis of most exclusive channels, as the detection of additional final state particles makes it possible to eliminate any electrons that are not the primary scattered electron. However, measurement of this contamination is essential to the analysis of inclusive reactions.

2.3.2   Detector Elements

CLAS includes several kinds of detectors that allow for particle identification, momentum measurement, and time of flight measurements. The detector elements that were used for the eg1b run were the drift-chambers, Čerenkov detector, time of flight

Beam Energy (GeV)	Torus Current (Amps)
1.6	1500, -1500
1.7	-1500
2.5	-1500
2.3	1500
4.2	2250, -2250
5.6	2250
5.73	2250, -2250
5.76	-2250

Table 2.1: Torus currents used for different eg1b beam energies.

scintillators, and the forward calorimeters. Fig. 2.5 shows a diagram of CLAS with each of these detectors labeled. The detectors are in six sectors (each corresponding to a region in ϕ) which can be analyzed independently. Each detector element will be described, starting from center of CLAS and working out.

Drift Chambers

The momentum of a charged particle in CLAS is determined using a series of multi-wire drift chambers [26]. Each sector contains its own set of drift chambers grouped into three regions. Region 1 is located very close to the center of CLAS, region 2 is located between the torus coils, and region 3 is located outside the torus coils (see Fig. 2.6). Each region contains twelve layers of wires, grouped into two sets of six layers each. The innermost of these sets (referred to as super-layers) in each region is oriented so that in the center of the sector the wires are in the ϕ direction. The outer super-layer of each region is turned by 6° so that information about the azimuthal position of the particle can be determined. Due to spatial constraints, the outer super-layer of region 1 has only four layers.

Each layer is made of a sense wire surrounded by four field wires. Adjacent

Large-angle Calorimeter

Electromagnetic Calorimeter

Drift Chambers
Region 1
Region 2
Region 3

TOF Counters

Cerenkov Counters
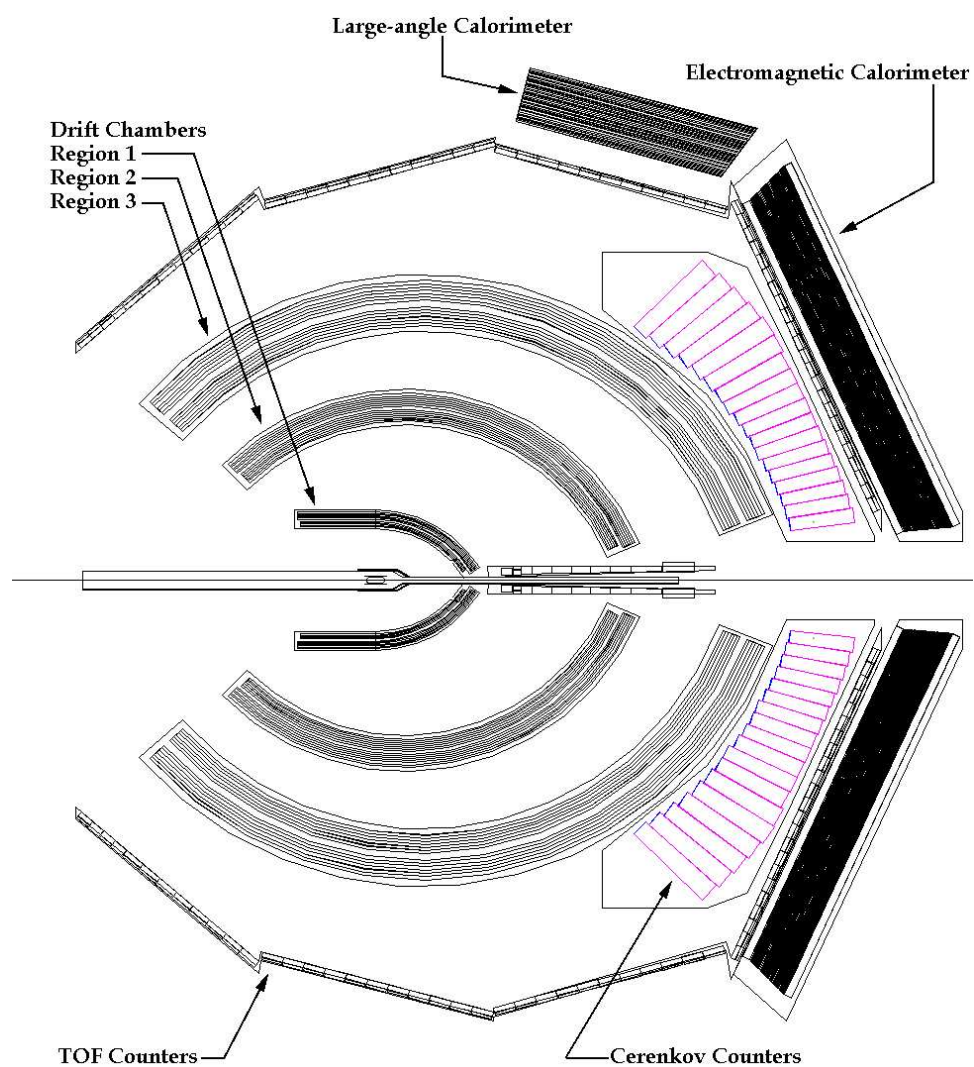
Figure 2.5: Drawing of CLAS in cross section with each of the detector elements labeled.
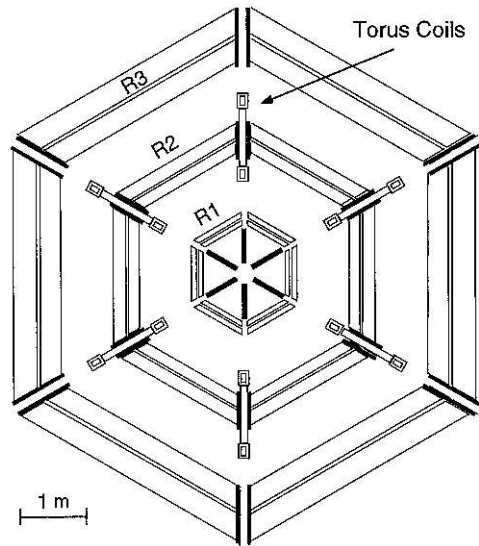
Figure 2.6: Drawing showing the location of the three drift chamber regions, looking along the beam line.
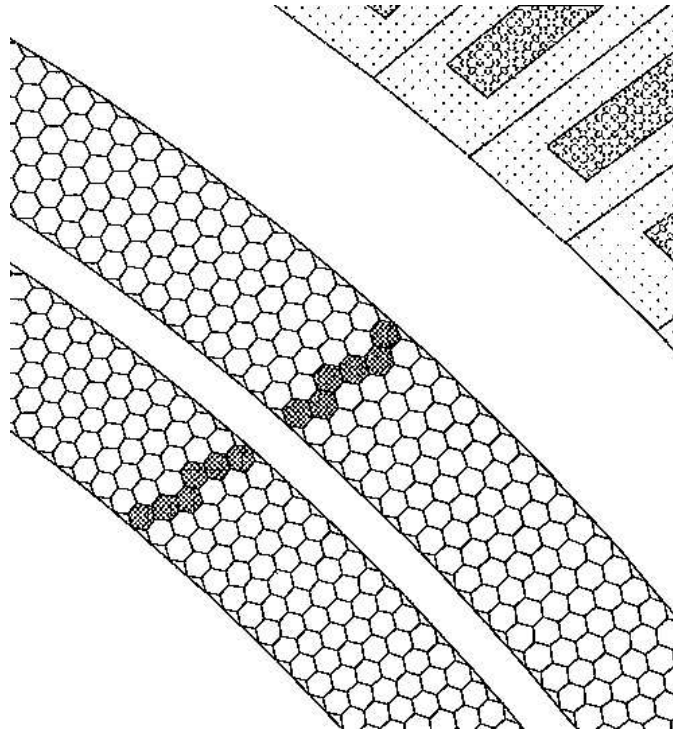
Figure 2.7: Drawing showing two super-layers of the drift chamber. The sense wires are located at the center of the hexagons and the field wires being located at the vertices of the hexagon.

layers are shifted by half of the distance between the sense wires. This results in a configuration, for the entire super-layer, of a sense wire surrounded by six field wires (four from the layer that the sense wire is in, and one wire from each of the two adjacent layers) in a hexagonal pattern as shown in Fig. 2.7. The space between the field wires and sense wires is filled with a constant pressure of gas (a mixture of 88% argon and 12% CO_2) that is continuously being recycled through each region. The sense wires are at a positive potential while the field wires are at a negative potential, with and absolute value of half of the potential on the sense wires. This keeps the total potential of the drift-chamber at zero, minimizing interference with other detector elements. Signals from each sense wire are sent to discriminators and TDCs (time-to-digital converters).

During data taking, it is necessary to monitor the rates in the drift chamber and the current on each of the sense wires to ensure that the entire drift chamber is being supplied with the necessary high voltage and that none of the TDCs or wires have failed.

Čerenkov Detectors

Outside the drift chambers lie the Čerenkov detectors [27]. The Čerenkov detectors are of a threshold type, segmented in θ, and are used to identify the charged particles. For most beam energies in the eg1b experiment, scattered electrons will emit Čerenkov radiation in the detector while produced pions will not. The Čerenkov is filled with gas (C_4F_{10}) at atmospheric pressure in order to obtain the desired index of refraction. The threshold for electrons is very low ($\sim$9 MeV) while the threshold for pions is quite high ($\sim$2.5 GeV). The gas in the Čerenkov detector is constantly recirculated, and the pressure is held constant using a system of pumps and valves.

Each segment of CLAS has its own Čerenkov detector. The detector consists of
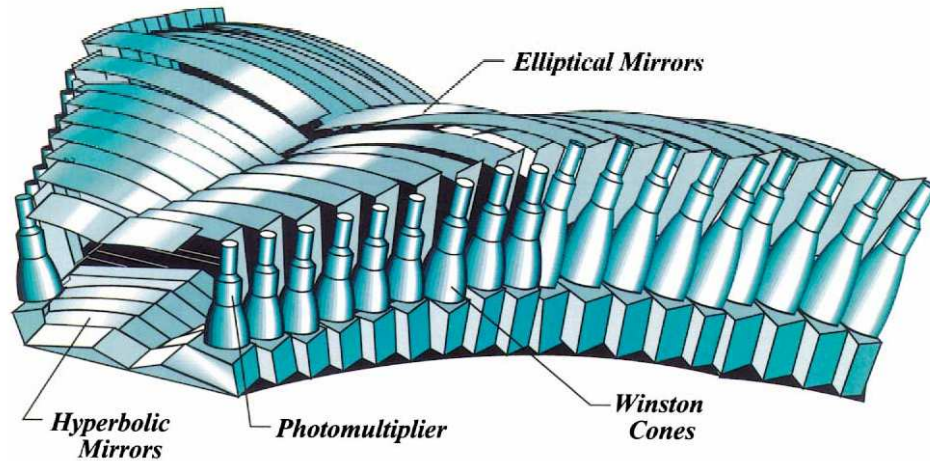
Figure 2.8: Drawing of one sector of the Čerenkov detector.

a series of 18 pairs of photo-multiplier tubes (PMTs) and mirrors, see Fig. 2.8. The detector uses two mirrors to reflect the Čerenkov light into the PMTs (see Fig. 2.9). This arrangement allows the PMTs to be behind the torus coils (which block the scattered particles), maximizing the useful acceptance of the Čerenkov, at the possible expense of sensitivity (due to losses associated with the mirrors). Each of these pairs of mirrors creates a segment that lies at a line of relatively constant θ. The width of these segments increases as θ increases, ensuring the entire forward region of the sector is covered. The segmenting of the detector in θ allows the Čerenkov information to be compared to the flight path of the the particles to help determine which particle in an event caused the signal in the Čerenkov.

Time of Flight

The time of flight system [28] consists of a series of scintillating paddles in the outer part of CLAS with pairs of PMTs attached to light guides. The time of flight of the particle is calculated by comparing the time at which a particle struck the scintillator
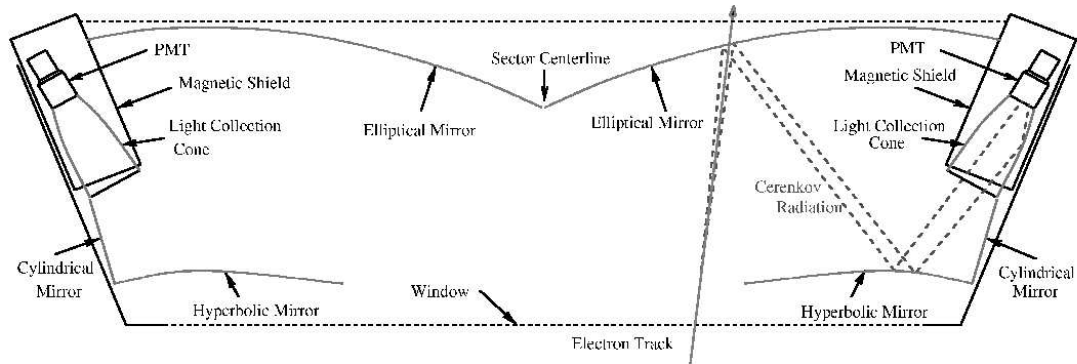
Figure 2.9: The mirror configuration used in each segment of the Čerenkov detector.

to the time at which the interaction occurred at the target. CLAS does not provide any information about this interaction time, so it is necessary to calculate it. This is done by identifying the primary electron in an event (using the Čerenkov detector and the calorimeter) and using its flight path length (as determined by the drift chamber) to calculate the time that it must have left the target. The speed of the electron is well known, as all of the scattered electrons are of a high enough energy that their velocity is nearly indistinguishable from the speed of light. In this fashion, the electron can be used to provide the time at which the interaction occurred for all of the particles in the event. If there is no electron detected in an event, it is impossible to find the start time for that event (for photon runs, an additional scintillating counter is placed in the center of CLAS to provide the start time for particles).

The paddles are located outside the drift chambers, between the Čerenkov detector and the calorimeters. The PMTs and other hardware are located in the shadows of the torus magnet, much like the Čerenkov detector PMTs. There are 48 total paddles, arranged in 4 planes in each sector (Fig. 2.10). The first 23 paddles are located in a single plane in the front of the detector covering the range between about 8 and 45 degrees. They are referred to as the forward-angle paddles. These forward angle paddles are all 15 cm wide, 5.08 cm thick, and have increasing length with their
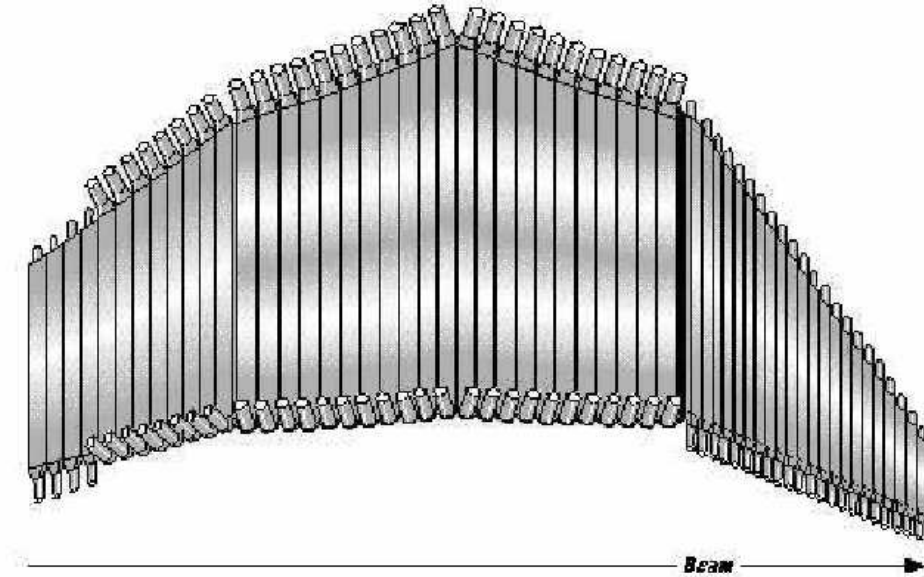
Figure 2.10: Time of flight scintillators for one sector. The forward angle paddles have 2 inch PMTs attached to straight light guides while most of the large angle paddles have bent light guides in order to fit 3 inch PMTs into the available space.

distance from the beam line so as to cover the entire azimuthal range. The remaining paddles are arranged in three more planes which are collectively referred to as the large angle paddles. These paddles are of varying width, but all are about the same 5.08 cm thickness. The length of these paddles is also different from paddle to paddle in order to keep the same azimuthal coverage as the drift chambers. All of the PMTs in the time of flight system are protected from the magnetic field produced by the torus system by cylindrical μ-metal shields.

Each paddle has a silica optical fiber located at the center. This allows laser light to be sent to the paddles from four ultra-violet lasers. This is necessary for the calibration of the time of flight system electronics.

Calorimeters

The forward electromagnetic calorimeters of CLAS [29] are used as part of the primary electron trigger as well as being used to discriminate electrons from hadrons and measure neutral particles. This is possible due to the different mechanisms by which electron and hadron deposit energy in the calorimeter. Electrons deposit energy primarily by radiating photons, which in turn produce positron-electron pairs which can themselves radiate. This results in an electromagnetic shower. The result of this is that the electrons tend to deposit a fraction of their initial energy in the calorimeter. In comparison, hadrons such as pions are minimum ionizing. This means that they interact in the calorimeter mostly by ionizing the atoms in the scintillator. This produces a fixed amount of energy, regardless of the momentum of the particle.

The calorimeters are in the shape of equilateral triangles (one per sector) placed in the forward section of CLAS. Each calorimeter is composed of 39 layers of lead and scintillator. The scintillator layers are composed of 36 strips of scintillator oriented parallel to one of the sides of the triangle. The strips in adjacent layers are rotated $120°$, as shown in Fig. 2.12. Positions of particles can be determined by comparing intersections of hits in the three different orientations. A layer of lead is placed between each layer of scintillators (Fig. 2.11). The light produced in the scintillators is sent to PMTs by a fiber light guide, and the signal from the PMTs is sent to ADCs and TDCs for analysis. For each of the three possible orientations, the layers are put into either an inner (inner 5 layers) or outer (outer 8 layers) group. This allows for improved ability to discriminate between pions and electrons.

The calorimeter can also be used to measure and identify neutral particles, but that ability is not used in this analysis due to the limited efficiency in detecting neutrons and the relatively good momentum resolution for the electrons and pions.
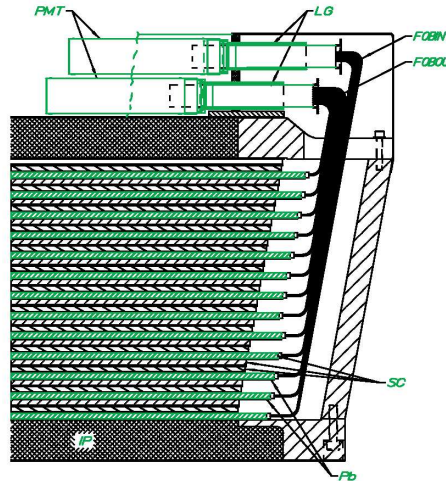
Figure 2.11: Cross section of the forward calorimeter showing the sandwich of lead and scintillator.
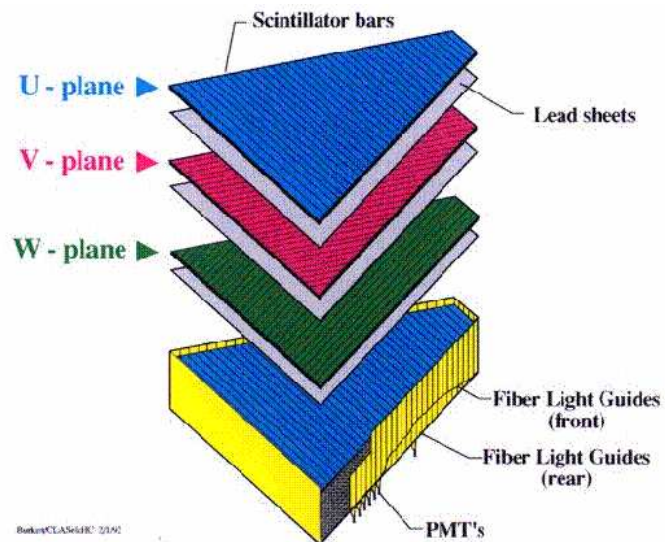
Figure 2.12: Exploded diagram of the electromagnetic calorimeter showing the orientation of the different layers as well as the location of the fiber light guides and PMTs.

The method used for identifying the events in which a neutron was present for the analysis will be discussed latter in section 4.5.

There is also a pair of large angle calorimeters which can be used to measure the energy of particles at very large polar angles. The construction of these calorimeters is much the same, but since they are not used in this analysis, they will not be discussed.

2.3.3   Calibration

The data from each detector element must be calibrated and used to calculate the physical properties of each of the particles. The Čerenkov detectors have the simplest calibration, as all that is necessary is to gain-match all of the PMTs in the system. This is done well before the experiment begins. The calibration of the drift chambers is also done ahead of the experiment, and is an ongoing project, as the properties of the drift chambers are affected by small changes in the wires of the chamber or the pressure of the gas. The other detector elements all require data to be taken in order for the calibration to be performed.

Time of Flight

The calibration of the time of flight system [30] is essential to this analysis because it is this system which is used to identify the positive pions in each event. For this reason, it is worthwhile to discuss this procedure in some detail.

The first step is a check to determine the status of each paddle in the TOF system during each energy and torus configuration. The ADC pedestal values (values that the ADC reads when there is no signal present) are then determined using dedicated pedestal runs. The pedestal values are recorded and taken into account directly when the data is taken. This alleviates the need for a software calibration to be done after

the experiment.

The ADC time walk correction (a correction for the offset of the pulse from a discriminator caused by a finite rise time of the pulse) and TDC calibration are performed with data taken during special light pulser runs. Further calibrations are performed using normal data files. These include determining the delay between the left side and right side PMTs for each paddle, a correction of the different energy deposited depending on the angle at which a particle enters the paddle, a time offset to the RF signal from the accelerator, and, very importantly, a paddle to paddle time offset correction. Many of these steps need to be repeated over and over to improve the values. The RF offset and paddle to paddle correction specifically have a large impact on the calculated start times and velocities and therefore great care must be taken to make these corrections as accurate as possible.

Calorimeters

The calibration of the calorimeters must be done before production data is taken, since the calorimeter is used in the electron trigger. If different parts of the calorimeter have different readings for a fixed amount of energy deposited, then the trigger could pick up a position dependent bias. The matching of the PMT signals is done using cosmic muons, the muons being chosen since they are minimum ionizing and therefore the deposited energy in the calorimeters is well known. These cosmic runs are taken at the beginning of the experiment, and the calorimeter PMTs gains are adjusted accordingly.

2.4   Data Acquisition and Trigger

2.4.1   Trigger

The trigger in Hall B consists of two levels. The level 1 trigger looked for hits in the time of flight system, the Čerenkov detector and sufficient energy deposited in the forward calorimeter (above a pre-set threshold) separately in each sector. The signals from the PMTs were used to gate the electronics and as start times for the TDCs. Rough checks were done to determine if the hits matched approximately in angle. Other geometrical requirements can be added depending on the experiment, such as requiring a coincidence of hits in opposite sectors, or rejecting events with hits in too many sectors. If it is desired, it is possible to add the level 2 trigger. The level 2 trigger requires that the hits that caused the level one trigger match up with a probable track in the drift chamber. If no probable track is found, then the event is cleared and the system is set to receive a new event. In the eg1b run, the level 1 trigger was used without the level 2 trigger.

2.4.2   Data Acquisition

The data acquisition system for CLAS was designed for rates of 4 MHz, but since then has been constantly improved upon. The data flow proceeds through three steps, the event builder (EB), event transport (ET), and the event recorder (ER). The event builder receives information from all of the devices in the hall over fast ethernet connection, combines them together for each event, then sends this information to event transport. The ET system gives access to this information to various on-line processes and also sends it to the event recorder. The event recorder saves the data on a RAID array located in the counting house, and also sends it to be recorded on
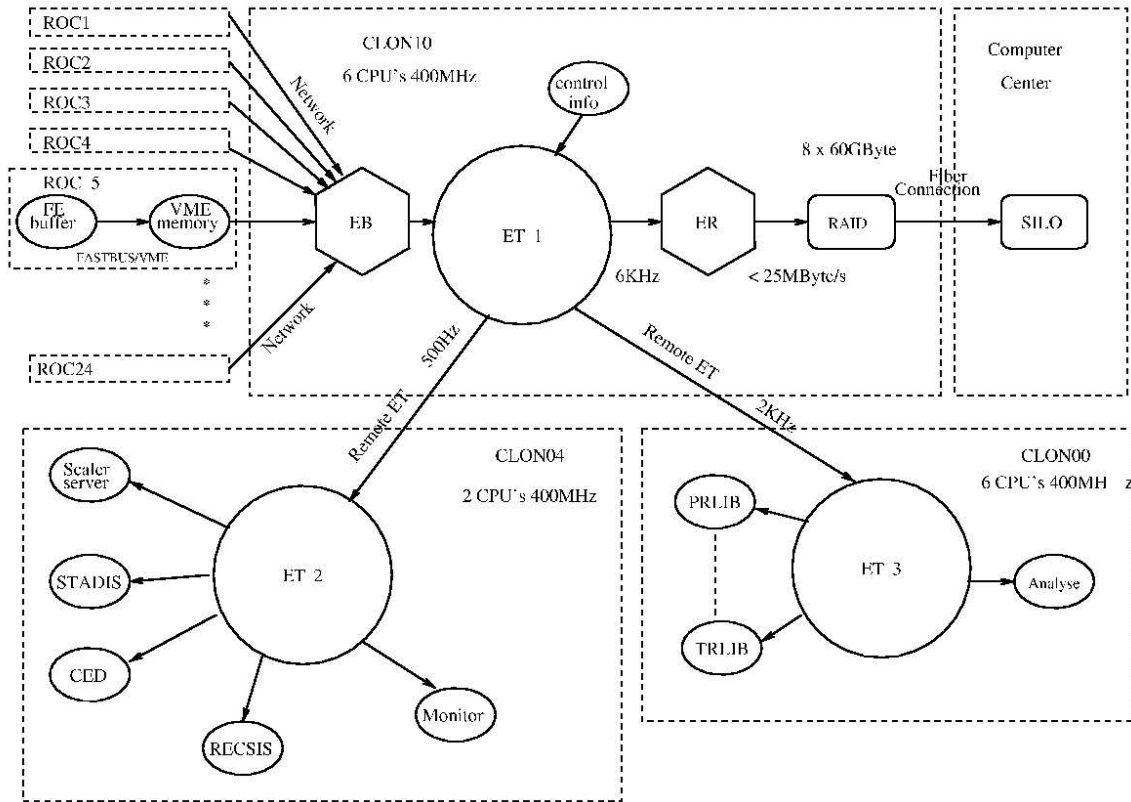
Figure 2.13: A diagram of the data flow for CLAS, showing the main data flow though acquisition to recording as well as parallel data flow for on-line programs and others.

the central tape silo. A diagram of the data flow is shown in Fig. 2.13.

2.5 Charged Particle Tracking

Tracking of charged particles starts with the identification of areas in each of the super-layers where there are adjacent hits. These clusters of hits are then compared to a database to determine which correspond to a possible particle track, represented in Fig. 2.14. This produces a series of line segments in each super-layer of the DC. The line segments are then compared to a database of possible tracks to see which line segments from the different super-layers come from the same particle. At this
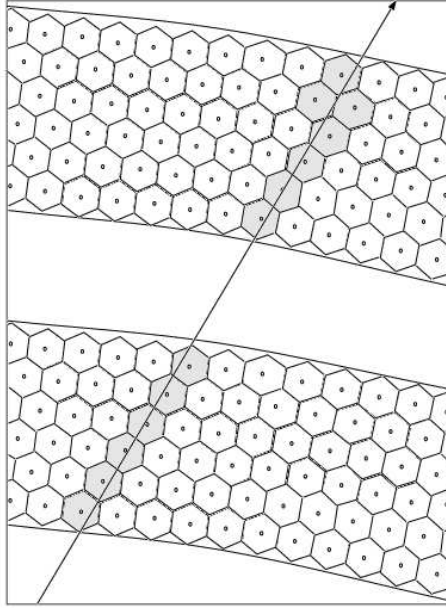
Figure 2.14: Drawing showing a possible particle trajectory through two super layers of the drift chambers and the correspond wire hits.

point, the segments have been linked together to form suspected tracks. These tracks are then adjusted with information from the time at which each of the readings was received from the DC sense wires. The drift times are used to determine the distance from the track to the sense wire. There is no way to tell which side of the sense wire the track passed from the timing information alone, but by comparing the results from all of the wires within a super-layer, and fitting a straight line to every one of the possible combinations of the track being on one side of the wire or another, it is possible to determine precisely the track of the particle through each layer. This process of correcting the tracks using the drift times is referred to as time based tracking (TBT). This information is then used for the final fitting of the track to the positions in all of the super-layers in the DC.

Tracks for particles can then be matched up with hits in the other detector elements (as in Fig. 2.16). The Čerenkov detector and time of flight systems have only
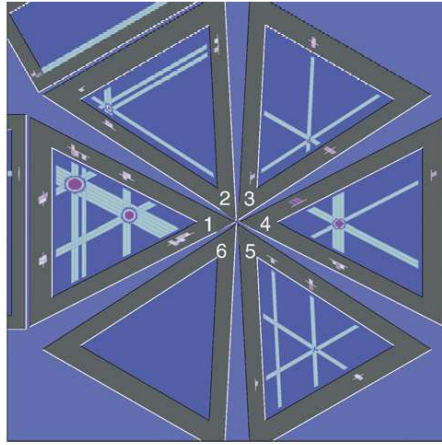
Figure 2.15: A view of the on-line reconstruction of the calorimeter hits showing how the orientation of the scintillator strips allows the location of the particle in the calorimeter to be determined.

polar angle information, so obviously that is all that is used to determine whether or not hits in these detectors go with a given track. The calorimeter is better in this regard, as the polar and azimuthal angles can be used together to match hits between the detectors (Fig. 2.15).

The path length (along with the time of flight information) is used to calculate the velocity β of the charged particles. The momentum of charged particles is determined by comparing the paths to a pre-generated look-up table of trajectories for given beam energy and torus magnetic field.

2.6 Further Information

Much more detailed information is available on the CLAS detector, including all of the subsystems and the data acquisition system, from the Nuclear Instruments and Methods paper by Mecking and others [25].
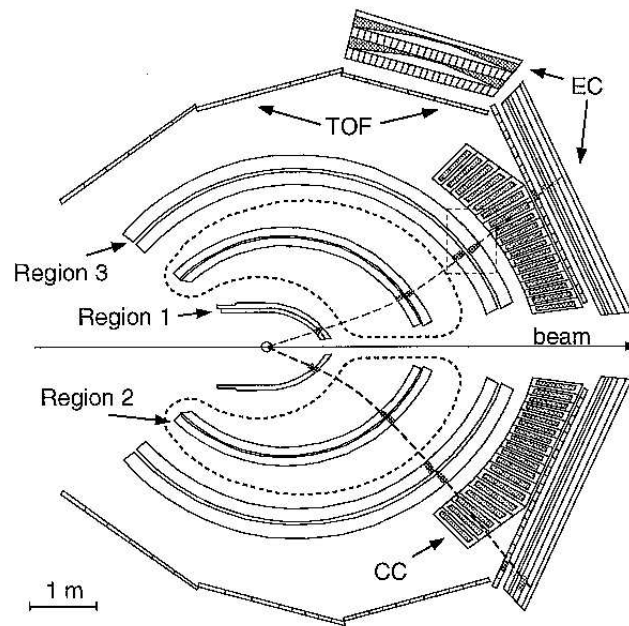
Figure 2.16: Cut view of all of the detector element with particle tracks showing the matching of the tracks from the drift chambers to the other detector elements.

Chapter 3

Polarized Target

3.1 Introduction

In order to measure the double spin asymmetry, it is necessary to have a polarized
nucleon target. The error on the asymmetry is proportional to the inverse of the
square of the polarization, so high polarizations are essential for precise measurement.
The eg1b experiment used a sample of NH_3 as a target, polarized through a process
known as DNP (dynamical nuclear polarization). A target using DNP has several
components that are required to operate. Among these are a high magnetic field ($\sim$
5 Tesla in the case of eg1b), low temperatures ($\sim$ 1 Kelvin for eg1b), a microwave
source, and a suitable target material, such as NH_3, which has had paramagnetic
centers added to it (paramagnetic centers are unpaired electrons which are free to
polarize in the magnetic field). Each of these systems will be discussed in detail,
along with a description of DNP.

The target apparatus was designed and built for the eg1a experiment. It has been
modified from original design used in SLAC [31] and JLab Hall C [32] to allow it to
fit into the CLAS detector.

3.2   DNP

The polarization that would naturally occur in a system of protons placed in a high magnetic field and low temperature is far too low for effective asymmetry measurements (it can be calculated for a given magnetic field and temperature using Eq. 3.1).

$$P_{TE} = \frac{e^{\frac{\mu B}{kT}} - e^{\frac{-\mu B}{kT}}}{e^{\frac{\mu B}{kT}} + e^{\frac{-\mu B}{kT}}} = \tanh\frac{\mu B}{kT} \tag{3.1}$$

Dynamic nuclear polarization was the process used in this experiment to enhance the polarization of the protons. In dynamic nuclear polarization (DNP) the target material is placed in a high magnetic field, and at a low temperature. Paramagnetic centers have been added to the material, in this case through irradiation. These radicals polarize in the magnetic field, and the polarization is then transferred to the protons by applying microwaves. There are two ways in which the process can be described, using the solid state effect and using the equal spin temperature theory. NH_3 is a hybrid material which does not follow either description exactly, but rather has aspects of both. The spin temperature description is more complicated, but is a more accurate description of the system. The solid state description is much easier to understand, and results in all of the correct conclusions being drawn in terms of the apparatus needed and expectations of results.

3.2.1   Solid State Approach

In the simplest picture, the microwaves transfer polarization to the proton by flipping both the proton and electron spins. The electron then relaxes quickly, while the proton remains polarized for a much longer period of time. The electron can then be used to flip more protons. By constantly flipping the protons, at a rate faster than their

decay, the target polarization is gradually increased.

The electron spins can be flipped using microwaves that are at the EPR (electron paramagnetic resonance) frequency of the electron in the magnetic field. The EPR frequency is the frequency that corresponds to the energy required to flip the orientation of a electron spin from anti-parallel to the magnetic field, to parallel to the magnetic field.

If the EPR frequency is used, however, the protons will not polarize. The proton spins need to be flipped simultaneously with the electron spins by supplying microwaves with a slightly higher or lower frequency than the EPR frequency. If the microwaves have a frequency, ν_μ, that is lower than the EPR frequency by an amount equal to the NMR (nuclear magnetic resonance) frequency of the proton, $\nu_\mu = \nu_{EPR} - \nu_{NMR}$, then the transition $e_\downarrow p_\downarrow \rightarrow e_\uparrow p_\uparrow$ occurs (where $e_\downarrow p_\uparrow$ is the lowest energy state, corresponding to a electron spin anti-parallel to the magnetic field and a proton spin parallel to the magnetic field). After a short period of time, the electron relaxes, $e_\uparrow p_\uparrow \rightarrow e_\downarrow p_\uparrow$ (these transitions are shown in Fig. 3.1). The electron can then be used again to polarize a different proton. Over time, the population of $p_\uparrow$ builds, increasing the positive polarization. The same apparatus can be used to increase negative polarization without the need to change the target field by using microwaves that have a frequency $\nu_\mu = \nu_{EPR} + \nu_{NMR}$. These microwaves are absorbed causing the transition $e_\downarrow p_\uparrow \rightarrow e_\uparrow p_\downarrow$. The electron then relaxes to $e_\downarrow p_\downarrow$. In this case, the population of $p_\downarrow$ builds, increasing the negative polarization.

This process only works under certain circumstances related to the relaxation times and concentrations of the paramagnetic centers and the protons [33]. These conditions can be derived from Eq. 3.2 which describe the rate of polarization change for the electron system and the proton systems, where N_S is the number of paramagnetic centers, N_I is the number of protons, P_S is the electron polarization, P_I is
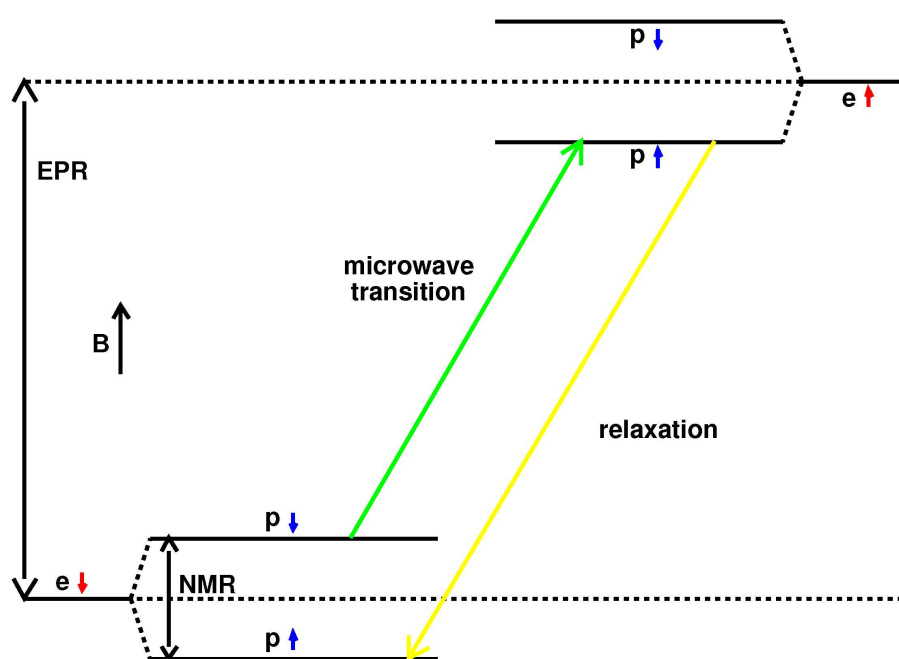
Figure 3.1: Energy levels from the solid state approach, the green line represent the transition excited by the microwaves, the yellow line represents the relaxation of the electron.

the proton polarization, T_S is the relaxation time of the electron, T_I is the relaxation time of the proton, V is the probability (per unit time) of a proton flipping along with the electron in the presence of the microwave radiation, and the super-script L denotes the values for the polarization when the system is in thermal equilibrium, meaning that there are no microwaves present. P_S^L is much greater than P_I^L due to the relatively low magnetic moment of the proton.

$$
\begin{aligned}
\frac{dP_S}{dt} &= -V(P_S - P_I) + \frac{1}{T_S}(P_S^L - P_S) \\
\frac{dP_I}{dt} &= \frac{N_S}{N_I}V(P_S - P_I) - \frac{1}{T_I}(P_I - P_I^L)
\end{aligned}
\tag{3.2}
$$

The polarization value at maximum can then be determined by setting the derivatives in Eq. 3.2 to zero resulting in the equations shown in 3.3. The largest values of P_I will occur when N_I/T_I is much less than N_S/T_S, meaning the the total rate of relaxation is much greater for the electron system compared to the proton system. In this case, the polarizations of the two systems can be approximated as in Eq. 3.4.

$$
\begin{aligned}
P_S &= \frac{P_I^L \frac{N_I T_S}{N_S T_I} + P_S^L (\frac{N_I}{N_S T_I V} + 1)}{\frac{N_I}{N_S T_I V} + \frac{N_I T_S}{N_S T_I} + 1} \\
P_I &= \frac{P_I^L (\frac{N_I T_S}{N_S T_I} + \frac{N_I}{N_S T_I V}) + + P_S^L}{\frac{N_I}{N_S T_I V} + \frac{N_I T_S}{N_S T_I} + 1}
\end{aligned}
\tag{3.3}
$$

$$
\begin{aligned}
P_S &\approx P_S^L \\
P_I &= \frac{P_I^L \frac{N_I}{N_S T_I V} + P_S^L}{\frac{N_I}{N_S T_I V} + 1}
\end{aligned}
\tag{3.4}
$$
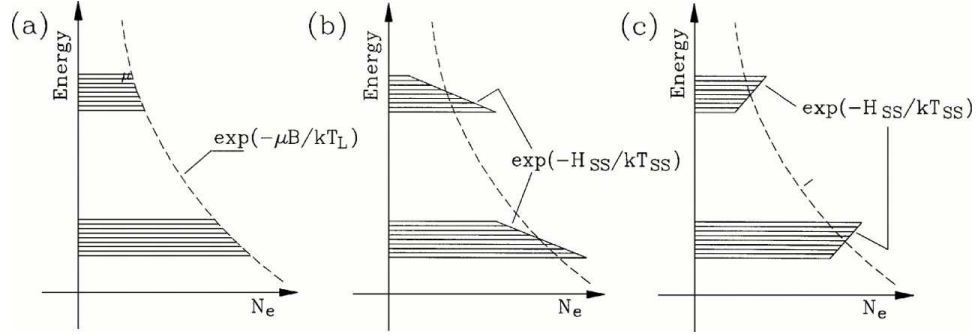
Figure 3.2: Energy levels in Equal Spin Temperature theory [34].

If, additionally, the rate of protons being flipped with the electrons by the microwaves $(N_S V)$ is much greater that the total relaxation rate of the protons (N_I/T_I) then the polarization of the protons can reach the the thermal equilibrium polarization of the electrons.

3.2.2   Thermodynamic Approach

The solid state view of the system in convenient because it offers a simple to understand description of the system. But, in target materials like ^{6}LiD, NH$_3$, ND$_3$, butanol and other alcohols, the solid state approach cannot be used to accurately describe the system. When the concentration of the paramagnetic centers is high, Equal Spin Temperature theory [34] must be used to describe the system.

The interaction of the free electrons can not be neglected, due to the abundance of these centers. The result is that the system no longer has discrete energy levels. Instead the system of electrons is described by two sets of continuous energy states. The system is described by Boltzmann distributions with temperatures T_{SS} and T_Z for the spin-spin interaction and electron Zeeman energy respectively. The Zeeman interaction determines the overall population of the two continuous spin states, and the spin-spin interaction determines the Boltzmann distribution within each state.

At thermal equilibrium, $T_{SS} = T_Z = T_l$ where T_l is the temperature of the lattice (Fig. 3.2A).

DNP proceeds by first using microwaves (again at a frequency slightly above or below the Larmor frequency of the electron, which is the same a the EPR frequency in the limit of free electrons) to increase or decrease T_{SS}. The electron system absorbs an amount of energy from the microwaves that is equal to $h(\nu + \delta)$ where $h\nu$ is the Zeeman energy for the electron. The energy $h\delta$ is absorbed by the spin-spin thermodynamic system and $h\nu$ is absorbed by the electron Zeeman system. If $\delta < 0$ the spin-spin system has to emit this energy, causing the system to cool (Fig. 3.2B). If $\delta > 0$ the spin-spin system has to absorb this energy, so the spin-spin system is heated. T_{SS} can also become negative (Fig. 3.2C). Negative temperature corresponds to negative polarization. In general, when a reduction in temperature, or cooling, is referred to it means a reduction in the absolute value of the temperature [35]. It is important to note, however, that for a system of negative temperature to cool, it must absorb energy.

The protons also form a Boltzmann distribution characterized by the Zeeman energy of the proton. The proton system is cooled by a double spin flip of the electron spins, along with a single spin flip of the protons. The spin of the electron system remains the same and therefore the energy of the electron Zeeman system remains the same, while the proton system emits (or absorbs) $h\nu_p$ where ν_p is the Larmor frequency of the proton. The energy is provided by the electron spin-spin system.

The proton Zeeman system, characterized by T_{Z_P}, moves to thermal equilibrium with the spin-spin system, $T_{Z_P} = T_{SS}$. The proton polarization constantly increases, as T_{Z_P} decreases. If the temperature of the spin-spin system had been made negative by the microwaves, then the thermal contact between the spin-spin system and the

proton Zeeman system would result in a negative value for T_{Z_P}, which corresponds to negative polarization. Meanwhile, the temperature of the electron spin-spin system is being maintained by means of the microwaves and the electron Zeeman system. The polarization of the proton system is the value that is determined from a simple Boltzmann distribution for the given temperature (as shown in Eq. 3.5).

$$P = \frac{e^{\frac{\mu B}{kT_{Z_P}}} - e^{\frac{-\mu B}{kT_{Z_P}}}}{e^{\frac{\mu B}{kT_{Z_P}}} + e^{\frac{-\mu B}{kT_{Z_P}}}} \tag{3.5}$$

3.3 NH_3 as Target Material

The essential characteristics for a polarized target material are high proton polarization and high dilution factor (percentage of the nucleus mass that is made up of polarizable protons). The best target in terms of dilution would obviously be H_2. Unfortunately, at low temperatures, pure H_2 is in a spin zero state, and not polarizable. Other materials were developed which have a high concentration of protons which can be polarized. Several materials are currently in use for different proton and deuteron experiments. These include ^{6}LiD, butanol, ND_3 and NH_3. ND_3 and ^{6}LiD are deuteron target materials, and not appropriate for this reaction. It is also possible to use ^{7}LiH, but it has the disadvantage that it takes a very long time to polarize. Butanol is not the preferred target material for this type of electron scattering experiment because it is very susceptible to radiation damage (depolarization caused by the electron beam, described in Section 3.8).

NH_3 was used as the target material in this experiment. It has been used as a source of polarized protons in a wide variety of experiments [32] [36]. It has a good combination of resistance to radiation damage, dilution factor, and polarizability. For this experiment $^{15}NH_3$ was used instead of naturally occurring $^{14}NH_3$. This was done

because ^{15}N is spin 1/2 as opposed to ^{14}N, which is spin 1. Additionally, the spin of the ^{15}N is carried mostly by a single proton. This makes the contribution of the polarized ^{15}N relatively easy to account for.

3.3.1 Material Preparation

Freezing

The NH$_3$ was frozen into a cylinder in a bath of liquid N$_2$ (LN$_2$) and then broken up into approximately 2mm size granules. This was done by flowing gaseous NH$_3$ into a sealed Teflon cylinder that was in a bath of LN$_2$. The NH$_3$ froze into one solid slug. The slug was crushed through a series of screens to form irregular beads of the desired size of about 2mm. It is necessary to use these small pieces for the target material, as one large chunk would not be able to be cooled sufficiently throughout.

Irradiation

The NH$_3$ requires the addition of paramagnetic centers to be polarized. Paramagnetic centers are free electrons which are free to align their spins in a magnetic field (NH$_3$ is diamagnetic under normal conditions). These centers can be added through chemical doping of the target material (this is usually done with alcohol targets) or through irradiation. In this experiment, paramagnetic centers were added to the NH$_3$ through irradiation [37] with an electron beam. The electrons from the beam knock out a proton from the NH$_3$ forming a NH$_2$ ion with a free electron usable as a paramagnetic center.

The target is exposed to a electron beam with a high current and irradiated at relatively warm temperatures (usually it is done under liquid argon). A further irradiation takes place in the experiment when the target is at liquid ^{4}He temperatures.

When an accelerator is not available to perform the warm irradiation, the cold irradiation, alone, is sufficient. In the eg1b experiment, most of the NH_3 was subject to irradiation in the CEBAF beam, at 1.3K in the polarized target cryostat.

3.4   Cryogenics

The polarized target is designed to run at temperatures at or below 1.3K. Previous data has shown that the maximum achievable polarization is greater for lower temperatures. Therefore, it is desirable to reach as low of a temperature as possible.

A ^{4}He evaporation refrigerator was used in this experiment, a drawing of which is shown in Fig. 3.3. By lowering the pressure of the helium through evaporation, the temperature of the liquid is lowered. The refrigerator consisted of several parts. There was a separator, heat exchangers, and a target chamber. Liquid ^{4}He entered the refrigerator through a vacuum insulated transfer line from the magnet reservoir. The transfer line was connected to a tube at the bottom of the separator section of the refrigerator. The separator consisted of a cylindrical volume with a sintered plate dividing the bottom and top sections. A metal bellows pump was attached to the top of the separator, and run at a high flow rate in order to draw the ^{4}He in through the tube. The tube passed through the sintered plate to the top section of the separator, where the ^{4}He sprayed out the open end of the tube. At this point the ^{4}He was a mixture of gaseous and liquid state. The liquid ^{4}He passed through the sintered plate and collected in the bottom of the separator, while the cold vapor was pumped away. The liquid in the bottom of the separator passed through one of two small tubes into the target chamber. The flow of liquid was controlled by two needle valves (one for each tube). Under normal operating conditions, the liquid moved through a tube that was attached to a series of heat exchangers (perforated copper plates). These

cooled the liquid down as it approached the target chamber. If liquid was needed in the target chamber very quickly, during the initial cooling of the target material for example, the other tube could be used, which bypassed the heat exchanges and instead sent liquid or cold vapor directly to the target chamber.
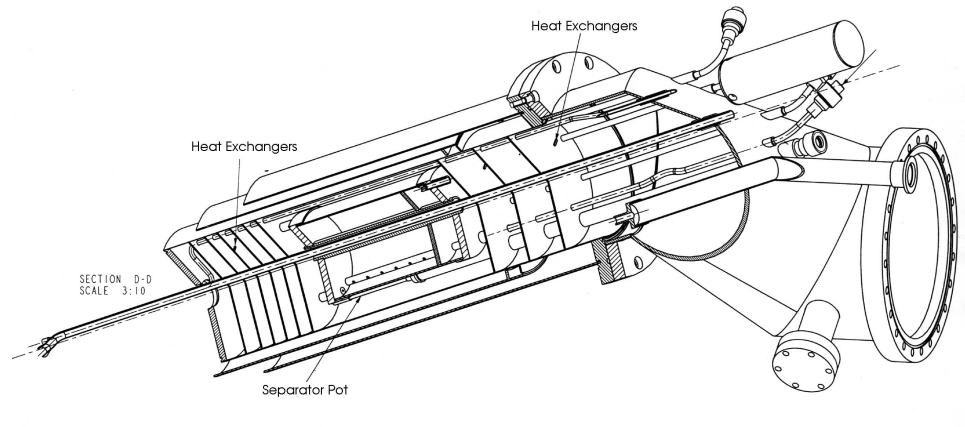
Figure 3.3: Drawing of the ^{4}He evaporation refrigerator [38].

The liquid in the target chamber was pumped on by a series of rotary vane and Roots pumps. The pump system is shown in Fig. 3.4. These pumps lowered the pressure of the liquid in the target chamber, thereby cooling it. The gas that is pumped away from the target chamber passed around the heat exchangers, cooling them. To maintain the liquid level in the target chamber, it was necessary to adjust the flow rate of cold vapor out of the separator, and the position of the needle valve controlling the supply of liquid to the chamber. This was done by using PID (proportional integral differential) loops to control the position of the needle valve, and the valve between the separator and the metal bellows pump. The ^{4}He evaporation refrigerator is capable of providing about 1 Watt of cooling power at 1.0K. This cooling power allows the temperature to remain relatively constant even with the heating from the beam and the microwaves.
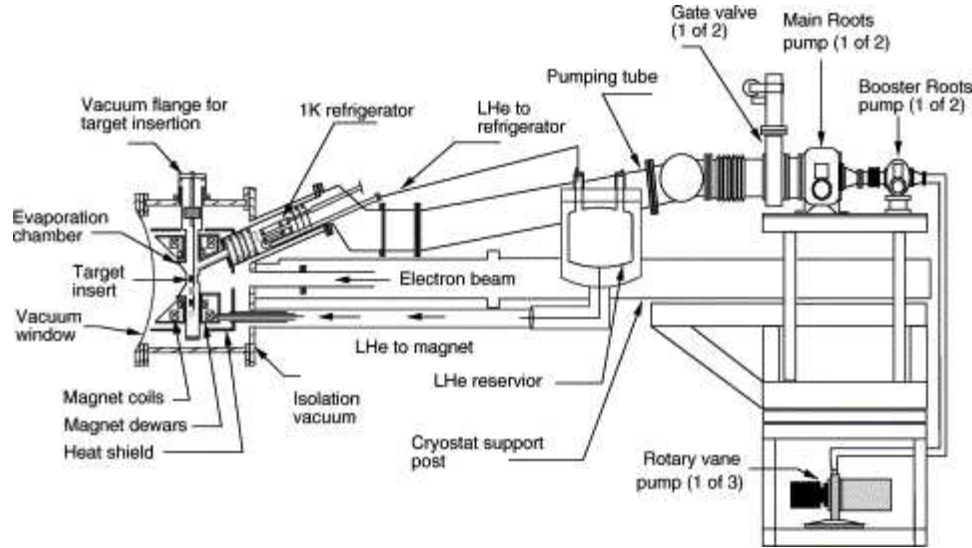
Figure 3.4: Drawing of the ^{4}He evaporation refrigerator and pump set with the cryostat [38].

3.5 Microwaves

A 140 GHz Varian EIO (extended interaction oscillator) tube was used to generate the microwaves used to polarize the target. The microwaves are transmitted to the target through a D-Band (110 GHz to 170 GHz) rectangular wave guide that leads to a microwave horn positioned next to the target. The power and frequency of the microwaves were continuously monitored by the use of a thermistor (for the power measurement), and a harmonic mixer (for the frequency measurement). These devices were coupled to the wave guide between the target and the EIO tube.

3.6 Magnet

There are two necessary characteristic of the magnetic field in the region of the target. The first is that the strength of the field be high. This is a requirement of DNP. The maximum target polarization generally increases as the magnet field increases. The

second characteristic is uniformity. The target field must be uniform to 10^{-4} in order for the NMR system to be used effectively. If the field is less uniform than this, the NMR signal (discussed in section 3.10) becomes too broad and distorted to be in the linear region of the NMR Q-curve. The uniformity is also necessary for DNP to be used. If the uniformity is bad, then different regions of the target would require different microwave frequencies to polarize. This frequency difference can be achieved by frequency modulating the microwaves over a small range.

In eg1b, target material was polarized in a 5 Tesla magnetic field, parallel to the beam direction. The field was created by the use of a super-conducting magnet submerged in ^{4}He. In order to place the target in the magnet, and allow both the beam and scattered particles to pass without striking the magnet coils, it was necessary to use a split Helmholtz pair (produced by Oxford Instruments) to produce the magnetic field. The uniformity of the magnet was 10^{-4} in a 2 centimeter diameter by 2 centimeter length cylinder at the center of the target.

The magnet was run in a persistent mode. This means that the leads of the magnet were shorted together with a superconductor. This effectively isolated the magnet from the power supply, which then can the be turned off. This benefits of this are that the power consumption of the system was minimized, and the heat added to the system by the power supply was lessened. The less heat that was added into the magnet the better, as it lowered the helium consumption of the system. This helped with the running of the refrigerator as well, as the refrigerator took its supply of liquid ^{4}He from the magnet reservoir. Additionally, with the magnet running in persistent mode, the magnetic field is much more stable than it would be otherwise, since drifts in the power-supply electronics will not affect the current in the coils.
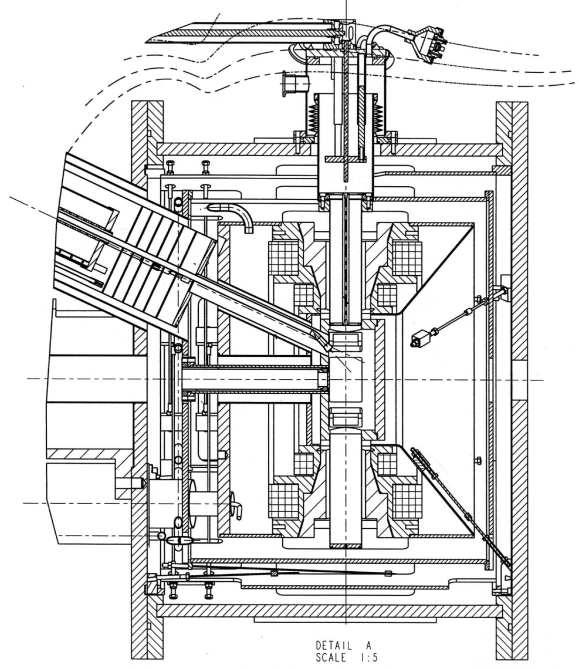
Figure 3.5: Cross section of the eg1 magnet cryostat.

3.7 Cryostat

The cryogenic and magnet systems of the target are contained in a cryostat, shown in Fig. 3.5. The purpose of the cryostat is to keep the magnet submerged in liquid ^{4}He and to provide heat shielding for the refrigerator. The ^{4}He level in the cryostat was maintained by connected reservoir of liquid ^{4}He. The reservoir was outside of CLAS. This was necessary for the cryostat to fit into the center of CLAS. The target was placed as close to the center of the CLAS detector a possible. The position of the target was 0.5m upstream of the center of CLAS during eg1b, a diagram is shown in Fig. 3.6. The helium that evaporated in the magnet passed through a heat exchanger which was used to cool the radiation shields of the magnet cryostat (the shields where cooled to $\sim$75 Kelvin). After passing through the heat exchanger, the gaseous helium was recovered and transferred back to the CEBAF liquefier.
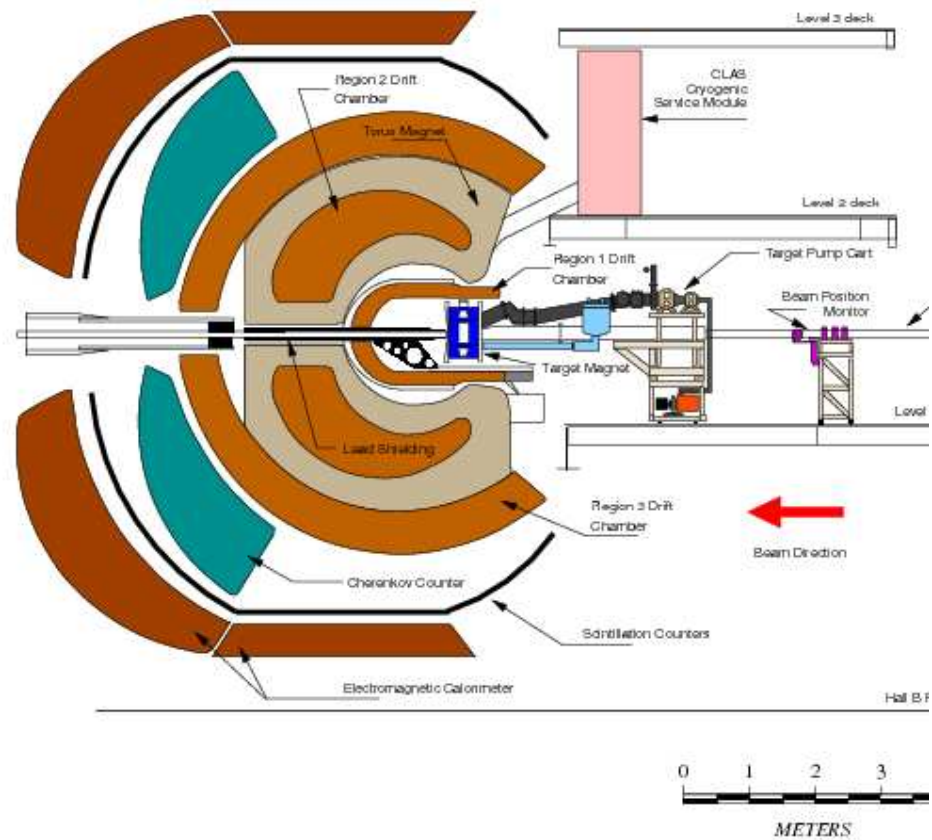
Figure 3.6: EG1 polarized target in CLAS.

3.7.1 Banjo

The refrigerated target chamber which was in the path of the beam was called the banjo due to its shape. It held the target insert, the microwave horn, and the 1K liquid ^{4}He. The banjo consisted of a cylinder, coaxial with beam line, with a vertical pipe at the top. There were thin vacuum windows in the beam line for the electrons to pass through, as well as thin walls about the radius of the cylinder for high angle particles to escape. The refrigerator was attached to the banjo on the upstream end. A tube met the upstream face of the banjo at a angle, allowing the refrigerator to pump on the liquid ^{4}He bath. The liquid was supplied with a small fill tube from the refrigerator. The banjo itself sat in the center of the magnet cryostat. Fig. 3.7 shows a drawing of the banjo.

3.7.2 Insert

Many different targets materials were used during the course of the experiment. To study the background, an empty target and a ^{12}C target were used. The experiment also took data with a deuteron target, made of ^{15}ND$_3$. Only one target at a time could be in the path of the beam. It was necessary to change the target on a regular basis.

Accessing the banjo was a time consuming process. The beam line had to be disassembled, the magnets de-energized, and the cryostat removed from CLAS. The refrigerator had to be filled with an over-pressure of helium gas. To avoid undergoing this procedure every time the target was changed, the different targets were all kept in the banjo at once. They were arranged on a rigid frame referred to as the insert, or target ladder. This ladder had four KEL-F cells, each with removable windows. The top cell could be filled with the small beads of frozen ^{15}ND$_3$ and the third cell form
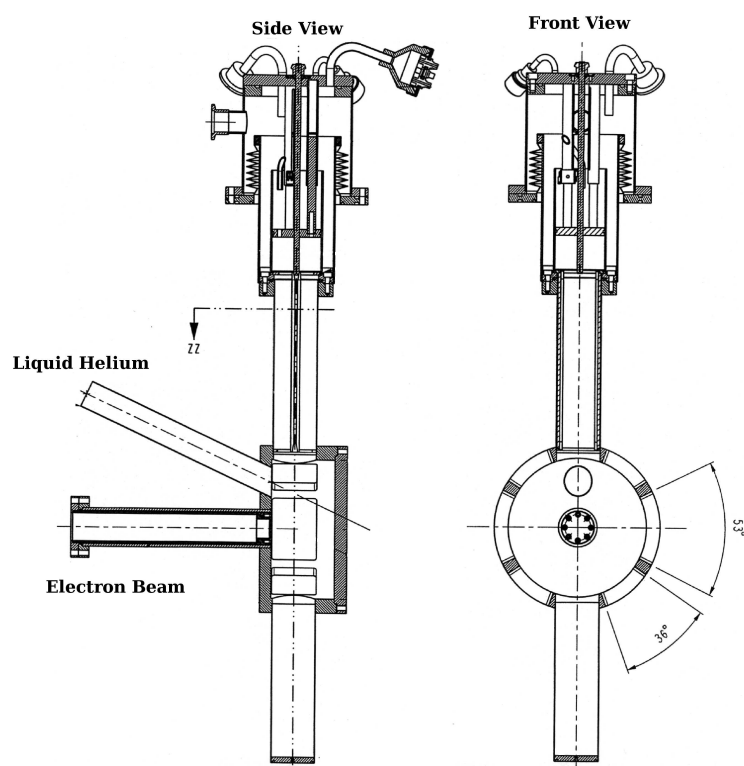
Figure 3.7: Banjo section of the target. Side and front views show the electron beam pipe, location of pipe for liquid helium from the refrigerator, and the thin windows.

the top could be filled with $^{15}NH_3$. The material was held in place using a removable Kapton window. The back of each cell was sealed with a thin piece of aluminum. The second cell from the top contained the ^{12}C and the empty target was at the bottom. The ^{12}C consisted of a graphite disk. The cell that was in the path of the beam could be changed remotely. The target ladder was attached at the top a worm gear which lead to a feed through at the top plate of the banjo. A stepping motor controlled the movement of the worm gear, raising or lowering the ladder into the proper position. Additionally, the position of the ladder in the banjo was stabilized by guide rails in the banjo, one on either side of the insert ladder. The position of the target was measured with an encoder on the stepper motor.

The ladder was attached to a brass plate which made thermal contact to the 75K shield of the cryostat.

3.8   De-polarization

Exposure to the electron beam can de-polarize the target material. This is referred to as radiation damage and is true for both chemically doped and irradiated materials.

In either type of target, the beam causes more paramagnetic centers to appear. The electron beam ionizes molecules in the target, producing free, polarizable, electrons. This usually occurs when the electron knocks a proton out of the molecule ($NH_3 \rightarrow NH_2^-$). This increase in the number of centers has a negative effect on the polarizability of the system (primarily through the broadening of the EPR transition and the increase in the number of relaxation paths for the protons). In the case of the chemically doped material, the chemical centers (TEMPO for example) can also be destroyed in the beam. For the irradiated target materials, the extra centers that are created are of a similar type to the centers that were introduced purposefully, the
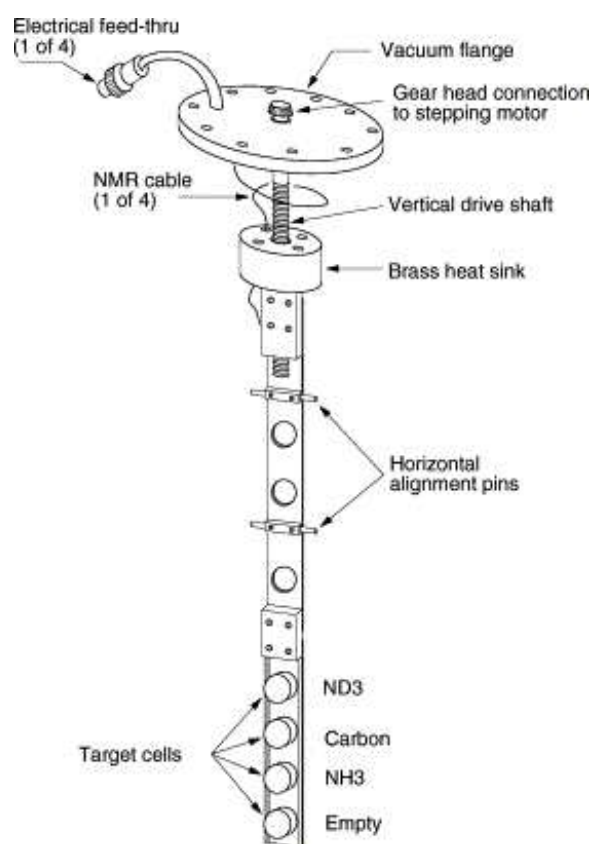
Figure 3.8: Drawing of the eg1 polarized target insert.

problem merely comes from the over abundance of the centers. In the case of the chemically doped materials, the new centers are of a different type and will have a slightly different frequency associated with them. This means that the new centers can not be used simultaneously with the old to polarize. The extra centers can be removed by heating the target, annealing, which will be discussed later. The centers that were destroyed in the chemically doped material cannot be regained however, so the annealing process cannot restore the polarization of chemically doped material.

3.9   Annealing

Annealing the target allows the polarization lost through radiation damage to be recovered. The target was annealed by raising its temperature of the target material to approximately 80K for 1-30 minutes. The method for raising the temperature was to use an electric heater on the insert. The heater warmed the helium that flowed past the target, which in turn warms the NH_3. At the increased temperature, the ions that have been formed by the radiation damage can recombine. For example $NH_2^- + H^+ \rightarrow NH_3$. Care was taken not to over anneal. That would have allowed all of the centers to recombine, and the material would have need to be irradiated again. By annealing target material, the total number of target material changes was reduced, increasing the total time that experiment could take data.

3.10   NMR

The polarization of the target was determined by measuring the NMR (nuclear magnetic resonance) signal.

NMR is the result of the nucleons flipping their spins in the magnetic field. To
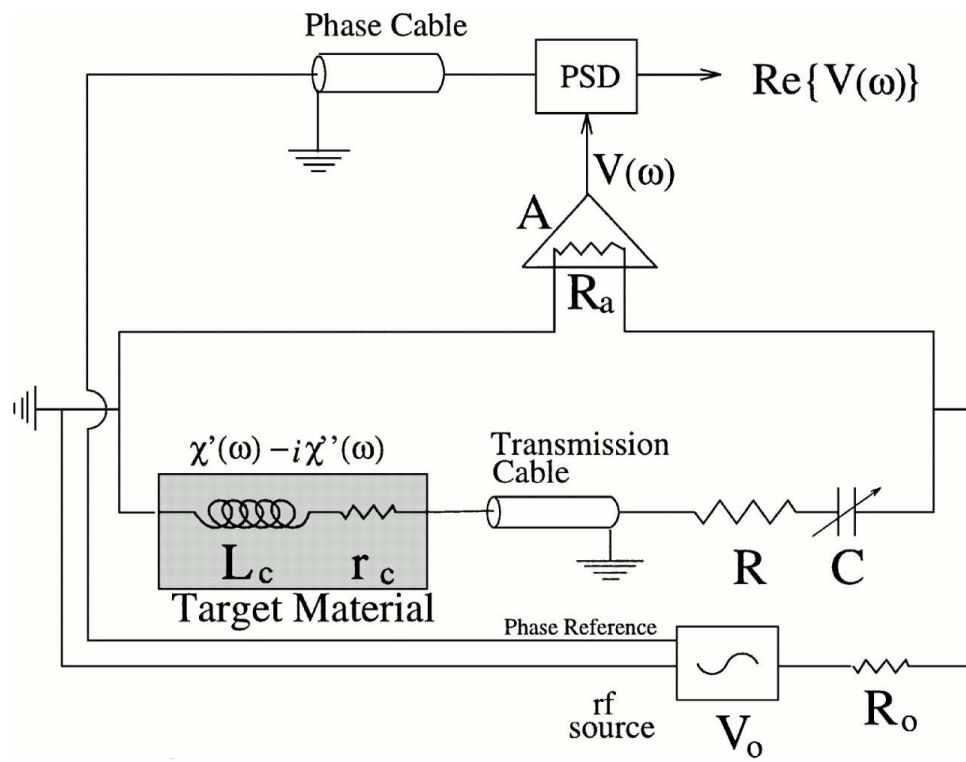
Figure 3.9: Diagram of the LCR circuit and Q-meter used to measure the polarization of the target [34].

do this, the nucleons (in this case protons) much either absorb or emit an amount of energy that corresponds to the Larmor frequency of the nucleon. The NMR system for this experiment consisted of an frequency modulating RF power-supply and a Liverpool Q-meter [39]. A diagram of these is shown in Fig. 3.9.

In the case of the eg1b polarized target, the target material was placed inside the inductor of a series tuned LCR circuit. In absence of target material, the measurement of the power as a function of frequency in the LCR circuit results in a simple Q-curve the shape of which represent the frequency response of the LCR circuit. When target material is present, however, it alters the inductance of the circuit due to the frequency dependent magnetic susceptibility $\chi(\omega)$ of the material. The magnetic susceptibility consists of an dispersive term, $\chi'(\omega)$, and an absorptive term, $\chi''(\omega)$, as shown in Eq. 3.6.

$$\chi(\omega) = \chi'(\omega) + i\chi''(\omega) \tag{3.6}$$

The magnitude of the absorptive term is directly proportional to the polarization of the material.

The LCR circuit was tuned to the Larmor frequency of the proton at the target magnetic field (213 MHz) using an RF diode to roughly measure the power as a function of frequency. Frequency modulated RF was applied to the circuit at a central frequency that was also the Larmor frequency of the proton. The power in the circuit was measured using a PSD (phase sensitive detector). In the case of the Liverpool Q-meter, the PSD is a balanced ring modulator (BRM) which outputs to an integrating circuit. The BRM requires a reference RF source, which must be in phase with the RF which is being measured. This was supplied by splitting the RF at the source, and adding delay to the reference end to match the phase. The reference
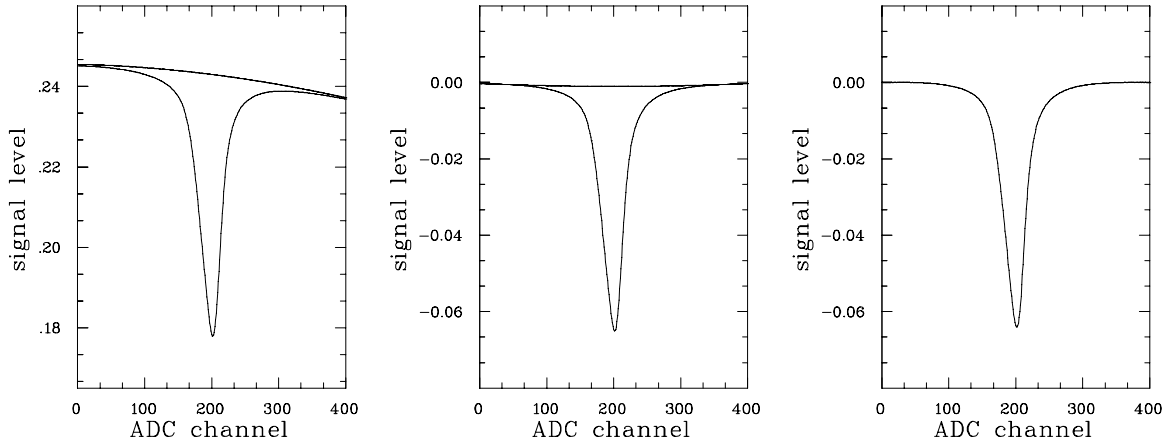
Figure 3.10: NMR signal before any baseline subtraction, after baseline subtraction, and after polynomial subtraction. Polynomial subtraction improves the backgound subtraction greatly, and helps account for drifts between the baseline and the signal. The signals shown are from E155x experiment at SLAC [40] but are typical of proton NMR signals showing enhanced polarization.

was then supplied to the BRM.

The Q-meter measures the Q-curve with either the added or subtracted peak at the Larmor frequency, corresponding to the power absorbed or emitted as a result of this dispersive term. The area of the peak was measured by first digitizing the Q-meter output in the absence of target material. This represented the background of the signal, referred to as a baseline. The baseline was subtracted from signals where there was material present, showing the contribution from the protons as a simple peak at the Larmor frequency (see Fig. 3.10). The area of this peak is directly proportional to the total absorbed/emitted power. Therefore, the area of the curve is also proportional to the polarization. The constant of proportionality is, unfortunately, very difficult to calculate. It depends on the exact properties of the target and the circuit. In order to determine this constant, the system must be calibrated with a known polarization.

3.10.1   TE Measurements

The only point at which the polarization can be determined exactly is when the target is in thermal equilibrium with the lattice. When the target is in this state, the polarization can be determined exactly through Boltzmann statistics as shown in Eq. 3.7.

$$P_{TE} = \frac{e^{\frac{\mu B}{kT}} - e^{\frac{-\mu B}{kT}}}{e^{\frac{\mu B}{kT}} + e^{\frac{-\mu B}{kT}}} = \tanh \frac{\mu B}{kT} \tag{3.7}$$

This was used to calibrate the NMR. The area of the signal was measured very carefully when the target was at thermal equilibrium. This measured area was compared to the calculated polarization to determine the constant of proportionality between area and polarization. This constant is used to determine the polarization of the enhanced signals.

Thermal equilibrium was achieved by warming the target up slightly, and waiting until the area of the NMR signal had stabilized. The polarization as it relaxes can be described as a function of time:

$$P(t) = Ae^{-\frac{t}{t_1}} + P_{TE} \tag{3.8}$$

where P_{TE} is the thermal equilibrium polarization. Thermal equilibrium is achieved as $Ae^{-\frac{t}{t_1}} \to 0$. This occurs when time $t \gg t_1$ where t_1 is the characteristic relaxation time of the proton spins.

The value of t_1 is dependent on the magnetic field, and various properties of the material, but also is inversely related to the temperature of the system. This means that the time that is needed to do TE measurement will be less if the target is warm, but P_{TE} and therefore the size of the signal, will be smaller. It is necessary to

strike a balance between the time necessary to do a TE measurement and the quality of the TE signal. Typically, TE measurements for the eg1 target where done at a temperature of 1.8K. This resulted in a t_1 on the order of ten minutes.

3.10.2 Beam Effects

Due to limitations in the CLAS drift chambers, the NMR coil could not be in the path of the beam, nor could the wall of the target cell. If the beam struck either the coil or the cell walls, the increased rate would cause the high voltage in the drift chambers to fail. Additionally, the small size of the target meant that if the coil had been placed inside the target cell, the scattering of the electrons off of the coil would have dominated the measurement. To avoid these problems, the NMR coil was placed outside of the cell, and the beam being rastered only over the inner part of the cell. This lead to a problem in determining the polarization with the NMR system. As the total accumulated beam charge that has passed through the target increases, the polarization decreases (radiation damage). The NMR was affected because it did not measure just the polarization at the beam spot, but for the whole target. If there was radiation damage to the center of the target, the NMR would over-estimate the polarization. The effect was made larger by the fact that the NMR was more sensitive to the material which was near it, which was the material that was not struck by the beam. This caused the NMR to give a reliable number for the polarization before the beam is turned on, but become less reliable as the dose increases. Therefore, for the data analysis, the elastic asymmetry was used to determine the product of the beam and target polarization.

3.11 Results

The polarization of the NH_3 was determined by comparing the measured elastic asymmetry to the known elastic asymmetry. The details of this process will be discussed in section 4.7. The results from the NMR are reliable for initial polarization, which was $> 90\%$.

Chapter 4

Analysis

4.1 Introduction

The double spin asymmetry A_{et} for $ep \rightarrow e\pi^+ n$ has been determined from the eg1b data. All of the energy settings from the eg1b run have been analyzed separately. In this section, the procedure used to analyze the data will be described.

4.2 Asymmetry

The polarization-dependent cross section for π^+ electro-production has the form as shown in Eq. 4.1

$$\sigma = \sigma_0 + P_B \sigma_e + P_T \sigma_t - P_B P_T \sigma_{et} \tag{4.1}$$

where σ_0 is the polarization independent part of the cross section, σ_e is the part of the cross section that depends on the polarization of the electron, σ_t is the part of the cross section that depends on the polarization of the target, and σ_{et} is the part of the cross section that depends on both the target and electron polarization. P_B and

P_T are the electron and target polarizations, respectively.

The eg1b data were taken in four helicity configurations, with the electron and the target spins alternating between positive and negative helicities. The electron helicity was reversed often (about once per second), and the value of the polarization of the electrons is independent of the helicity, meaning that the positive and negative electron polarizations can be treated as being the same. The target polarization, however, was only reversed about once for each energy setting and can have a large helicity dependence. Therefore it is necessary to define the polarization for the target and the beam in two regions, corresponding to the time when the target polarization was positive or negative, P_B^+, P_B^-, P_T^+, and P_T^-.

P_B^+ and P_B^- are the electron polarizations for the periods when the target had positive and negative polarization, respectively. P_T^+ and P_T^- are the target polarization magnitudes in the same periods. It is convenient to define ratios of the beam (Eq. 4.2) and target (Eq. 4.3) polarizations in the different target helicity states.

$$R_B = \frac{P_B^+}{P_B^-} \tag{4.2}$$

$$R_T = \frac{P_T^+}{P_T^-} \tag{4.3}$$

The number of detected events in each helicity state can then be written as:

$$N_{++} = D_{++}[\sigma_0 + P_B^+ \sigma_e + P_T^+ \sigma_t - P_B^+ P_T^+ \sigma_{et}] \tag{4.4}$$

$$N_{+-} = D_{+-}[\sigma_0 + P_B^- \sigma_e - P_T^- \sigma_t + P_B^- P_T^- \sigma_{et}] \tag{4.5}$$

$$N_{-+} = D_{-+}[\sigma_0 - P_B^+ \sigma_e + P_T^+ \sigma_t + P_B^+ P_T^+ \sigma_{et}] \tag{4.6}$$

$$N_{--} = D_{--}[\sigma_0 - P_B^- \sigma_e - P_T^- \sigma_t - P_B^- P_T^- \sigma_{et}] \tag{4.7}$$

where N_{++} is the number of detected events in the case of both target and beam having positive helicity or polarization, N_{+-} is the case where the electron has positive helicity and the target has negative polarization, N_{-+} is the case when the electron helicity is negative and the target polarization is positive, and N_{--} is the number of counts when the beam helicity and target polarization are both negative. D_{++}, D_{+-}, D_{-+}, and D_{--} are the luminosities in the respective helicity states. Since the absolute luminosity will be canceled in the asymmetry, it is only necessary to use the relative luminosities in the different helicity states. This is done by measuring the accumulated beam charge in each of the four helicity states by means of a scaler readout on the Faraday cup. It is convenient to normalize the counts by the luminosities and define new quantities (Eq. 4.8).

$$N'_{++} = N_{++}, \ N'_{+-} = \frac{D_{++}}{D_{+-}}N_{+-}, \ N'_{-+} = \frac{D_{++}}{D_{-+}}N_{-+}, \ N'_{--} = \frac{D_{++}}{D_{--}}N_{--} \tag{4.8}$$

In terms of these quantities, the three relevant spin asymmetries are extracted:

$$A_e = \frac{\sigma_e}{\sigma_0} = \frac{1}{P_B^+} \frac{(N'_{++} - N'_{-+}) + R_B R_T(N'_{+-} - N'_{--})}{(N'_{++} + N'_{-+}) + R_T(N'_{+-} + N'_{--})} \tag{4.9}$$

$$A_t = \frac{\sigma_t}{\sigma_0} = \frac{1}{P_T^-} \frac{(N'_{++} + N'_{-+}) - (N'_{+-} + N'_{--})}{(N'_{++} + N'_{-+}) + R_T(N'_{+-} + N'_{--})} \tag{4.10}$$

$$A_{et} = \frac{\sigma_{et}}{\sigma_0} = \frac{1}{P_B^+ P_T^-} \frac{(N'_{-+} - N'_{++}) + R_B(N'_{+-} - N'_{--})}{(N'_{++} + N'_{-+}) + R_T(N'_{+-} + N'_{--})} \tag{4.11}$$

4.3 Run Selection

In order to measure the asymmetry accurately, it is necessary to ensure that only runs which contain good data are used. For this analysis, good data consists of runs which used an NH_3 or carbon target, had suitable beam parameters, the detector was functioning properly, and the data in the files has been cooked (running the calibration code on the data is referred to as "cooking" the data). These criteria are checked by performing a number of tests on the cooked data files, and comparing the results of the tests to the information about that run that was saved in the logbook and CLAS database.

4.3.1 Target Material

The first check is to see if the inclusive electron count rates are appropriate for the target information in the logbook. The different targets have slightly different densities and total cross sections, meaning that the count rates can be used to determine the target material.

4.3.2 Beam Helicity Switching

The beam polarization was changed in a pseudo-random pattern. Periods where the electron helicity was constant are referred to as helicity "buckets". The the helicity of the first bucket in a pair is determined in a random fashion, while the helicity of the second bucket in a pair is always the the opposite of the first bucket. This ensures roughly equal statistic for each helicity state as well as helping in the cancellation of any time-dependent effects on the rate, since data from both helicities is always taken in very close proximity in time. On occasion, helicity buckets will not follow this pseudo-random pattern, often due to a resetting of the accelerator, or a misread

helicity synchronization signal. In this case, the events from that particular pair of helicity buckets are rejected.

4.3.3 Target and Beam Helicity Sign

The sign of the inclusive asymmetry is well known, for different values of W. This means that a very simple calculation of the asymmetry can be used to verify the sign of the target polarization and the status of the half-wave plate. This has been done for all runs. The results are shown in Fig. 4.1.

4.3.4 Total Rates

One of the best ways to check the operation of the detector and the cooking of the data files is to look at the rates in each of the sectors for every file. If there is a large change in the rates from sector to sector or file to file, that is indicative of a problem with the detector or the cooking. An example would be if the high voltage in the drift chambers faulted for a long period of time. This would reduce the drift chamber rates dramatically for the corresponding file. Looking at these rates would allow that file to be flagged as "bad" and the data in it would not be analyzed. The rates for all of the different detector elements were checked on a file-by-file basis for all of the runs. The files were in general rejected if the rates differed from the average rate in that run group by more than 5%.
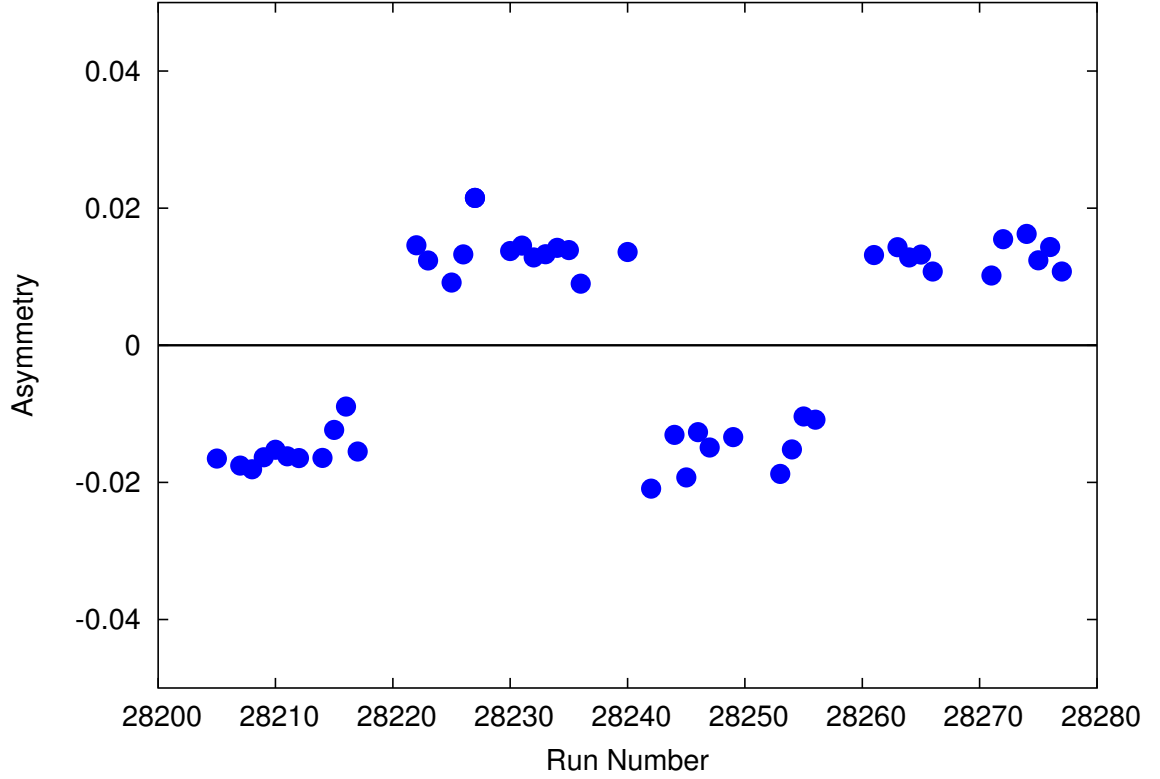
Figure 4.1: A plot of the asymmetry used to determine the sign of the beam helicity. The inclusive asymmetry is measured in all of the W region outside of the Δ resonance. The sign of this asymmetry should be the same as the sign of the target polarization. The Δ resonance is excluded to enhance this asymmetry (the asymmetry has the opposite sign in the region of the Δ).

4.4   Particle Identification

4.4.1   Electrons

There are several requirements for a particle to be identified as an electron. The first is that it must have negative charge. Also, it must produce a signal in the Čerenkov detector. This is used because all but the highest momentum pions are traveling too slow to produce Čerenkov radiation in the detector. The segment of the Čerenkov where the signal was detected must also lie near the path of the particle as determined by the drift chambers. This additional requirement minimizes the possibility that a

pion will be detected along with an unrelated signal in the Čerenkov and misidentified as an electron. The energy deposited in the calorimeter must also be an appropriate fraction (in this case $> 1/5$ was used) of the momentum of the particle. This cut is useful because the pions are minimum ionizing, meaning that any will deposit a fixed amount of energy regardless of its momentum. The standard electron cuts are shown in Table 4.1.

Kinematic Variable	Accepted Range
p_e (GeV/c)	$p_e > E_{beam}/10$
χ^2_C (Radians)	$\chi^2_C < 0.12$
N_C	$N_C > 2$
EC_{inner} (GeV)	$EC_{inner} > 0.06$
EC_{total}/p_e	$EC_{total}/p_e > 0.2$

Table 4.1: The electron identification cuts. p_e is the momentum of the electron. E_{beam} is the incident beam energy. χ^2_C is the difference in radians of the position of the Čerenkov detector segment and the path of the particle as determined by the drift chambers. N_C is the number of photo-electrons produced in the Čerenkov detector. EC_{inner} is the energy deposited in the inner layer of the calorimeter and EC_{total} is the total energy deposited in the calorimeter.

These cuts are not optimal in the event that the momentum of the particle is high (greater that about 2.5 GeV/c). This is because at that momentum, the pions exceed the threshold in the Čerenkov. Since the Čerenkov photo-electron cuts are therefore useless in that range, the cut is loosened dramatically for particles with momentum greater than 3 GeV/c, and the EC_{total} cut is slightly restricted to try and compensate for the extra pion contamination. The cuts used for particle of momentum greater than 3 GeV/c are shown in Table 4.2. The EC_{total}/p_e values are shown as a function of particle momentum in Fig. 4.2

Kinematic Variable	Accepted Range
p_e (GeV/c)	$p_e > E_{beam}/10$
χ^2_C (Radians)	$\chi^2_C < 0.12$
N_C	$N_C > 0.5$
EC_{inner} (GeV)	$EC_{inner} > 0.06$
EC_{total}/p_e	$EC_{total}/p_e > 0.24$

Table 4.2: The electron identification cuts used for high momentum particles, the EC_{total}/p_e cut and the N_C cut have been changed.

4.4.2 π^+

The particle identification for π^+ is made primarily by comparing the time at which the particle struck the TOF scintillator to the time that it would have struck the scintillator if it had the path length and momentum measured from the drift chambers, and the mass of a π^+. This time difference is evaluated using Eq. 4.12

$$\Delta_t = (TDC_{time} - START_{time}) - \frac{l}{c\sqrt{\frac{p^2}{p^2+m_\pi^2}}} \qquad (4.12)$$

where Δ_t is the time difference, TDC_{time} is the TDC reading from the TOF scintillator for the particle being evaluated, $START_{time}$ is the time at which the particle left the target, l is the path length of the particle trajectory as determined from the drift chambers, c is the speed of light in appropriate units (cm/ns), p is the momentum of the particle, also determined by the drift chamber, and m_π is the mass of the π^+. The value of $START_{time}$ is determined by using the path length and time of flight for the scattered e^-, whose speed is very close tot he speed of light and largely independent of momentum. This means that π^+ can not be identified through this method if the scattered e^- is not detected.

In order to optimize this cut, the range of Δ_t that was allowed for a particle to be
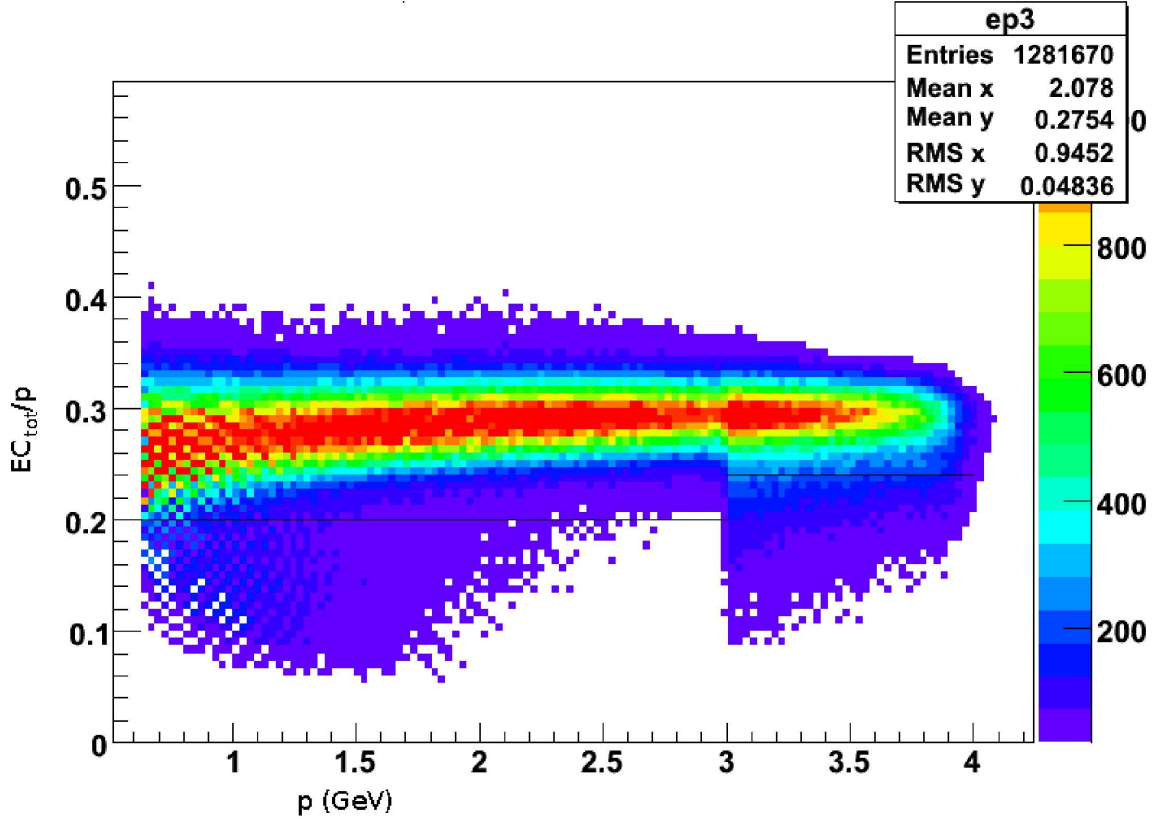
Figure 4.2: A plot of EC_{total}/p_e versus p_e for a run from the 4.2 GeV in-bending data set after Čerenkov cuts have been applied. The enhancement in the spectrum above $p_e = 3$ GeV can be clearly seen as the Čerenkov cut becomes less restrictive.

classified as a pion was determined for each of the paddles in the time of flight system independently. This allows for the variations in the time resolution of the different paddles to be taken into account automatically. Generally, the absolute value of Δ_t is required to be less than 1.2 ns, although this can vary greatly for some of the paddles, often due to slight mismatches in the timing between the left and right PMT signals for the paddle. A small mismatch will result in a broadening or shifting of the peak, while larger mismatches are usually removed in the time-of-flight calibration process.

Additionally, for the particle to be identified as a π^+, it must not pass the electron identification cuts on the calorimeter energy and the Čerenkov signal, and it must

have positive charge. The requirement that the particle fails the electron cuts helps to minimize the positron contamination in the π^+ sample. Also, particles are rejected if they are produced with a physical angle θ from the beam line greater than 48°. This is to avoid particles that may have passed through the edge of flange on the exit of the target cryostat. A plot of the value of Δ_t is shown in Fig. 4.3 for particles that conform to the other requirements of the π^+.
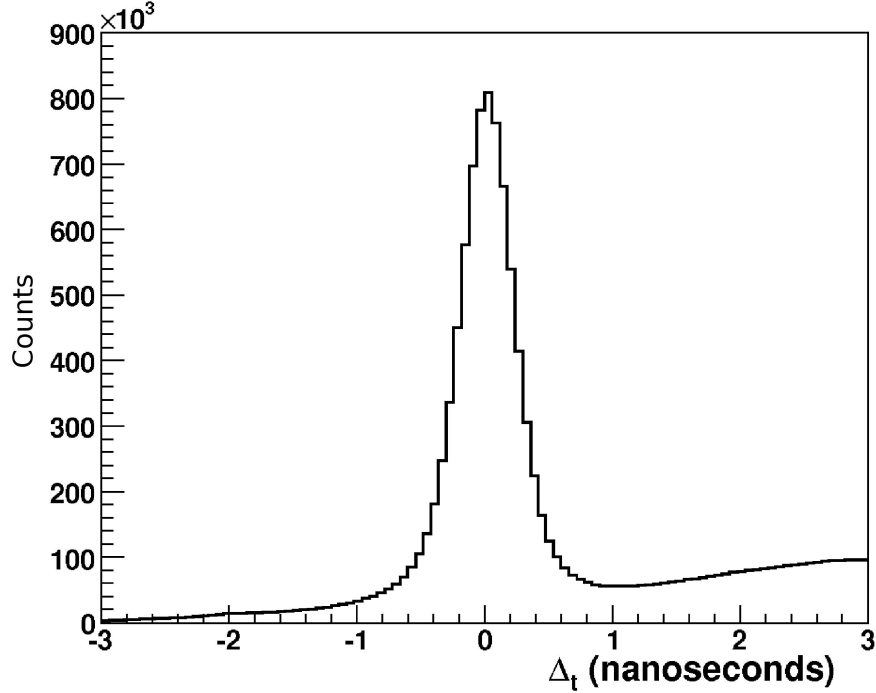
Figure 4.3: Difference between expected time of flight of a π^+ and the measured time of flight of the positive charged particle. The peak from the π^+ particles can clearly be seen, centered around zero.

4.4.3 Proton

The particle identification for the proton is made using the time of flight system in the same manner as for the π^+, with the substitution of the mass for the proton, m_p into the equation for Δ_t (Eq. 4.13). The particle is also required to have positive

charge. The protons are only used in exclusive elastic events, meaning that more complicated proton identification cuts are unnecessary, as the elastic exclusive cuts will remove particles which are not protons.

$$\Delta_t = (TDC_{time} - START_{time}) - \frac{l}{c\sqrt{\frac{p^2}{p^2+m_p^2}}} \tag{4.13}$$

4.5 Exclusive $ep \to e\pi^+ n$ Channel

For this analysis it is necessary to extract only the exclusive $ep \to e\pi^+ n$ events. A series of kinematic requirements was used to ensure that the events detected are truly from the $ep \to e\pi^+ n$ reaction. These included cuts on the number and types of particles detected, a z vertex cut on all of the charged particles in the event, and, since there is no requirement that the neutron be detected, a cut is applied to the missing mass of the un-measured particle in the final state.

4.5.1 Detected Particles

For an event to count as exclusive $ep \to e\pi^+ n$, the first requirement was that the event contain no more than three detected particles. Furthermore, one of the particles was required to be an electron (as properly identified by both the tracking software and the definition from the previous section), one of the particles was required to be a π^+ (as previously defined) and the third particle (if detected) was required to be neutral. Since the efficiency of detecting neutral particles is low in CLAS, there was no requirement that the third particle be detected at all. Instead, the presence of the neutron was determined by measuring the missing mass M_X in the reaction $ep \to e\pi^+ X$ and requiring it to be that of a neutron.

4.5.2 Missing Mass

M_X was determined through conservation of energy and momentum as shown in Eq. 4.14.

$$M_X^2 = ((E + M_p) - (E' + E_{\pi^+}))^2 - (\vec{k} - (\vec{k'} + \vec{p}_{\pi^+}))^2 \qquad (4.14)$$

The M_X^2 values for events form a distribution which is peaked at the mass of the neutron. This spectrum is used for both the identification of exclusive events, and for the calculation of the dilution factor, as described in section 4.6. An event is defined as exclusive $ep \rightarrow e\pi^+ n$ if it has a value of M_X such that $0.90\text{GeV} < M_X < 1.05\text{GeV}$. The spectrum for $^{15}\text{NH}_3$ (integrated over all kinematic bins for display purposes) is shown in Fig. 4.4.

4.6 Dilution Factor

In order to calculate the asymmetry from the relative number of counts in the different helicity states, it is necessary to know the fraction of the counts that result from polarized e^- scattering from one of the polarized H in $^{15}\text{NH}_3$. Scattering from unpolarized material dilutes the value of the asymmetry, which must be corrected as shown in Eq. 4.15, where f_D is the dilution factor, defined in Eq. 4.17. For the exclusive analysis, this factor is determined by comparing the spectrum of the missing mass of the neutron in the $ep \rightarrow e'\pi^+ n$ for the $^{15}\text{NH}_3$ and the ^{12}C targets. For the $^{15}\text{NH}_3$ target, the missing mass spectrum has sharp peak at the mass of the neutron. The broad background underneath the peak is the contribution from the ^{15}N. The peak itself is results from scattering from the H. The shape of the ^{15}N spectrum is closely approximated by the ^{12}C spectrum. The difference in the amplitudes of the
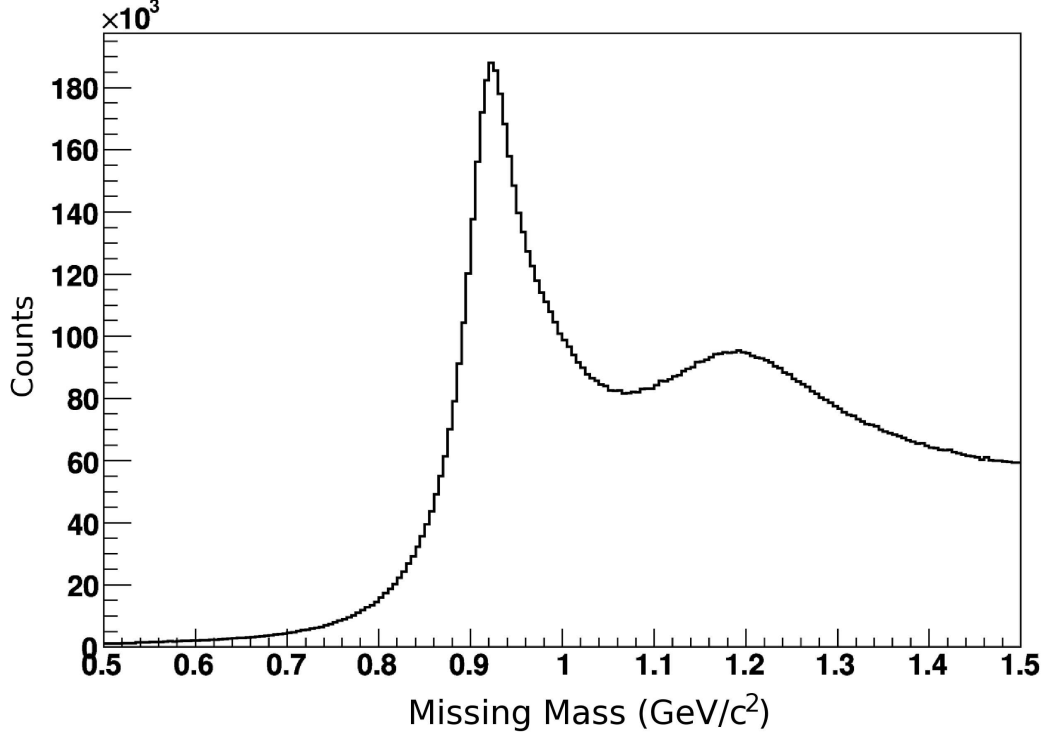
Figure 4.4: The missing mass spectrum for ^{15}NH$_3$.

spectra is caused by the ratio of the cross section for π^+ production on ^{15}N and ^{12}C. In order to normalize the ^{12}C to the ^{15}NH$_3$ spectrum, both were integrated in the range well below the neutron peak. A ratio of the counts from the ^{15}NH$_3$ to ^{12}C was calculated in this region as shown in Eq. 4.16. The number of counts in the region of the neutron mass is then determined for both the ^{15}NH$_3$ and ^{12}C. The counts from ^{12}C are multiplied by the normalization ratio to approximate the contribution of the ^{15}N in the region of the neutron peak. These scaled ^{12}C counts were then used in Eq. 4.17 to calculate the dilution factor f_D.

$$A_{phys} = \frac{1}{f_d \cdot P_B P_T} A_{meas} \qquad (4.15)$$

$$r = \frac{\sigma_{^{15}N}}{\sigma_{^{12}C}} = \frac{N_{W<0.8\,^{15}NH_3}}{N_{W<0.8\,^{12}C}} \tag{4.16}$$

$$f_d = \frac{N_H}{N_{^{15}NH_3}} = \frac{N_{^{15}NH_3} - N_{^{15}N}}{N_{^{15}NH_3}} = \frac{N_{^{15}NH_3} - r \cdot N_{^{12}C}}{N_{^{15}NH_3}} \tag{4.17}$$

The constant of proportionality between the ^{12}C and ^{15}N spectra was calculated for each energy setting as a function of $\cos\theta^*$. Since the asymmetry uses the counts in different helicity states, normalized to the accumulated charge in those states, and to the relative target polarizations, the ^{15}N counts were normalized to these same factors:

$$r = \frac{(N'_{-+} - N'_{++}) + R_B(N'_{+-} - N'_{--})}{(N'_{++} + N'_{-+}) + R_T(N'_{+-} + N'_{--})} N'_{^{12}C} \tag{4.18}$$

Notice that the beam polarization ratio that is in the numerator of the asymmetry is not used. That is because the ^{15}N contribution in the numerator of the asymmetry is canceled automatically without need for the dilution to be considered.

This value was then used to calculate the dilution at each point where the asymmetry was calculated. The error associated with the dilution consists of two parts. The first is a systematic error that is from the ratio of ^{12}C to ^{15}N, this error will be discussed along with the other systematic errors in a later section. The other error is a statistical error from the ^{12}C counts underneath the neutron peak. This error has been fully propagated into the statistical error on the asymmetry.

4.7 $P_B P_T$

The protons were identified for the purposes of determining the product of beam and target polarization for each energy setting. The value of $P_B P_T$, where P_B is the
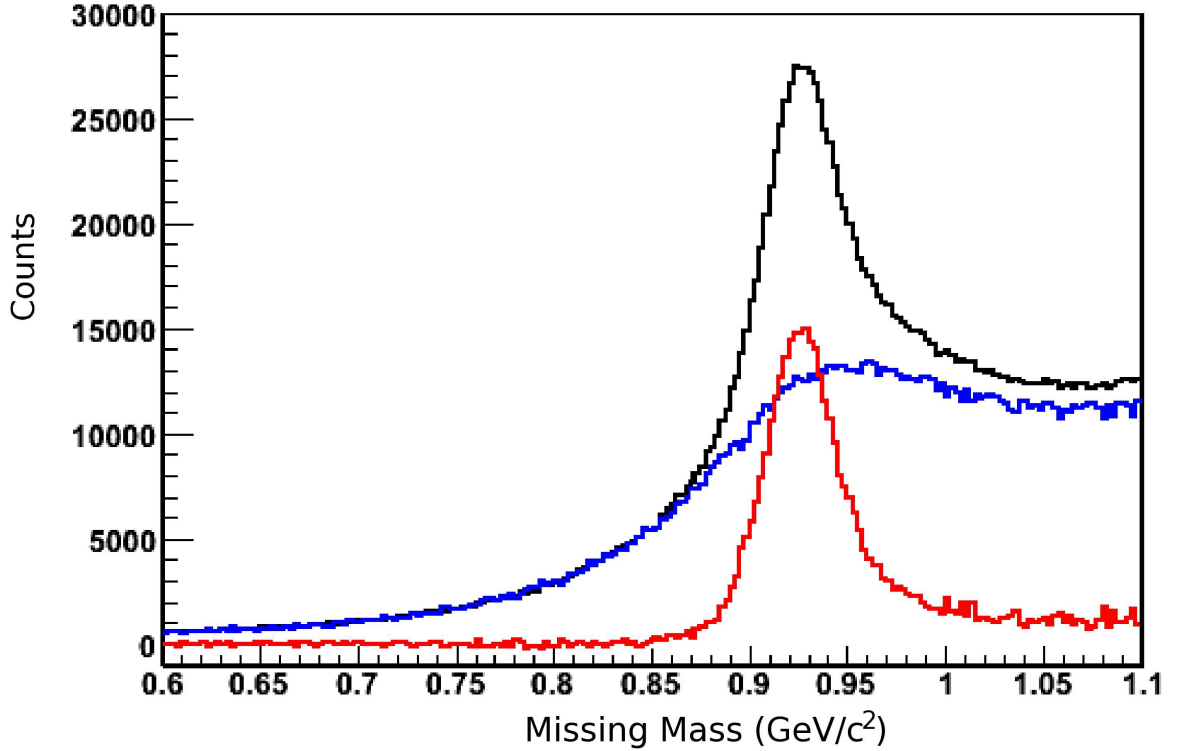
Figure 4.5: The missing mass spectrum for $^{15}NH_3$ (black), ^{15}N as approximated by ^{12}C (blue), and the proton (red).

beam polarization and P_T is the target polarization, was determined by measuring the asymmetry for elastic $ep \rightarrow ep$ scattering and comparing it to the known asymmetry.

For this analysis, only exclusive elastic $ep \rightarrow ep$ scattering was used to determine $P_B P_T$. This was done to minimize the contribution of the unpolarized target material to the measurement of $P_B P_T$. Exclusive events were separated from non-exclusive ones by a series of cuts. The first cut is the most straight forward one, exclusive events were defined as events in which only the proton and electron were detected. Further kinematic cuts were then applied. The first was a loose cut on W in the region of the elastic peak. The momentum and energy conservation allow for the calculation of the momentum and energy of an elastically scattered proton. The expected energy of the elastic proton, $E_{expected}$ was calculated by means of Eq. 4.19. The measured energy of

the proton was required to be within 150 MeV of this value. The angle $\theta_{expected}$ was calculated in Eq. 4.20 and the measured θ was required to be within 2° of this value.

The last cut was on the difference between the azimuthal angle of the scattered electron, ϕ_e, and the azimuthal angle of the proton ϕ_p. This cut checks the co-planarity of the electron and proton, as if the event is truly elastic, component of momentum perpendicular to the beam line must be equal and opposite for the electron and proton. The distribution of this value was also used to subtract the background events that result from the ^{15}N in the ^{15}NH$_3$. The dilution previously calculated for $ep \to e\pi^+ n$ cannot be used in these circumstances, since the cross section for elastic scattering is very different than the cross section for π^+ production. The distribution of events in $\phi_e - \phi_p$ is shown in Fig. 4.6. If the target was made of pure H, then the distribution would be a peak at 180°. The broad and rather flat background is caused by scattering off of the ^{15}N. The background is assumed to be linear in the region underneath the peak. This means that the background can be determined by integrating the distribution in the region nearby the peak, and using that to deter-mine the contamination under the peak. The advantage of analyzing the exclusive reaction becomes apparent, as the background is very simple, and more importantly, the background itself is very small, meaning that the error in the calculation of $P_B P_T$ is relatively independent of the dilution.

$$E_p = E_{Beam} + M_p - \frac{M_p E_{Beam}}{M_p + 2E_{Beam} \sin^2 \frac{\theta_e}{2}} \tag{4.19}$$

$$\theta_{expected} = \cos^{-1} \left(\frac{E_{Beam} - (E_{Beam} + M_p - E_{expected}) \cos \theta_e}{\sqrt{E_{expected}^2 - M_p^2}} \right) \tag{4.20}$$

The value of $P_B P_T$ was calculated by comparing the measured asymmetry for elastic scattering (Eq. 4.21) to the expected values of the asymmetry. $N_{anti-parallel}$

Table 4.3: Exclusive Proton Cuts.

Kinematic Variable	Accepted Range
W (GeV)	$0.85 < W < 1.035$
E_{proton} (GeV)	$|E_{proton} - E_{expected}| < 0.15 GeV$
θ_{proton} (Degrees)	$|\theta_{proton} - \theta_{expected}| < 2.5°$
$\phi_{proton} - \phi_{electron}$ (Degrees)	$178° < \phi_{proton} - \phi_{electron} < 182°$

and $N_{parallel}$ are the counts (with the background subtracted) from when the beam and target polarizations are anti-parallel and parallel, respectively. For this analysis, the asymmetry is always constructed with a fixed sign of the target polarization and an alternating sign for the beam helicity. A detailed description of the method can be seen in [41]. The expected value of the asymmetry was determined using Eq. 4.22 where $\tau = \frac{Q^2}{4m_p^2}$, $\epsilon = \frac{1}{1+2(1+\tau)\tan^2 \frac{\theta}{2}}$, and $r = \frac{G_M^p}{G_E^p}$. The ratio r was chosen to be $r = \frac{2.79}{1-(\frac{Q^2}{6})}$ to model the value of r as obtained from recoil polarization experiments [42].

$$A_{meas} = \frac{N_{anti-parallel} - N_{parallel}}{N_{anti-parallel} + N_{parallel}} \tag{4.21}$$

$$A_{calc} = 2\tau r \frac{\frac{m_p}{E_{beam}} + r(\tau \frac{m_p}{E_{beam}} + (1+\tau)\tan^2 \frac{\theta^2}{2})}{1 + \tau \frac{r^2}{\epsilon}} \tag{4.22}$$

$$P_B P_T = \frac{A_{calc}}{A_{meas}} \tag{4.23}$$

$P_B P_T$ was measured independently for the case where the target had a negative or positive polarization with respect to the beam-line. $P_B P_T$ was calculated in each of the standard Q^2 bins. This was done as a check on the process as the actual value of $P_B P_T$ was a physical property of the beam and target and therefore cannot depend on any kinematic variables. The result of $P_B P_T$ as a function of Q^2 was fit to a flat
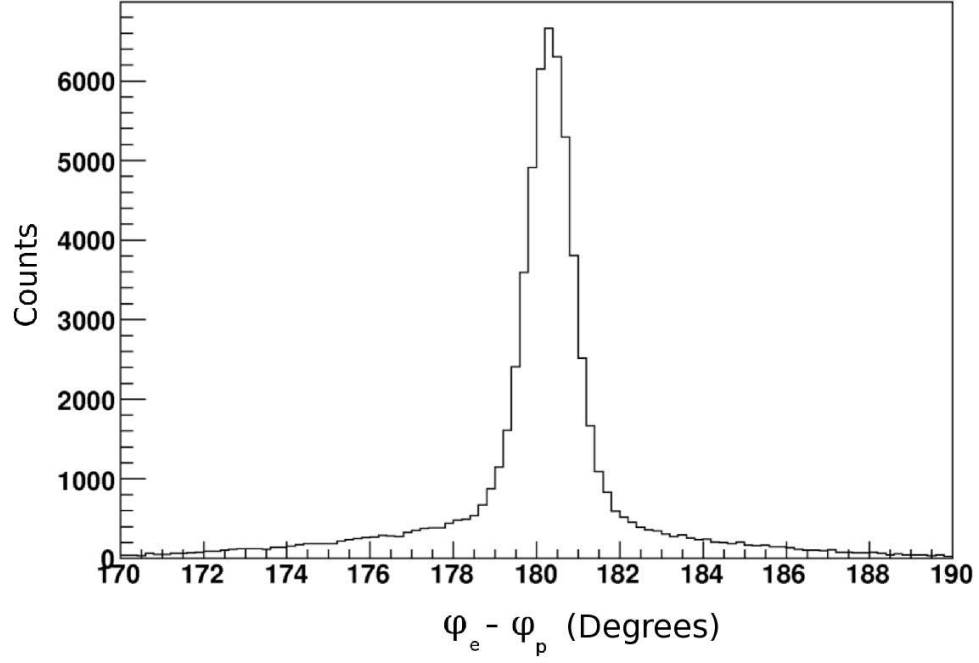
Figure 4.6: Co-planarity plot for the electron and the proton. The difference in the azimuthal angles $(\phi_e - \phi_p)$ is 180° for elastic events.

line as shown in Fig. 4.7. The $P_B P_T$ used for the analysis was obtained through an error weighted sum of the values at each Q^2. The result of the average $P_B P_T$ value for the 4.2 GeV energy runs as well as the error on the average are shown in Table 4.4.

Table 4.4: $P_B P_T$ for 4.2 GeV data.

Torus Polarity	Target Helicity	$P_B P_T$	$\sigma_{P_B P_T}$
In-bending	+	0.507	0.018
In-bending	-	-0.484	0.018
Out-bending	+	0.557	0.023
Out-bending	-	-0.458	0.02
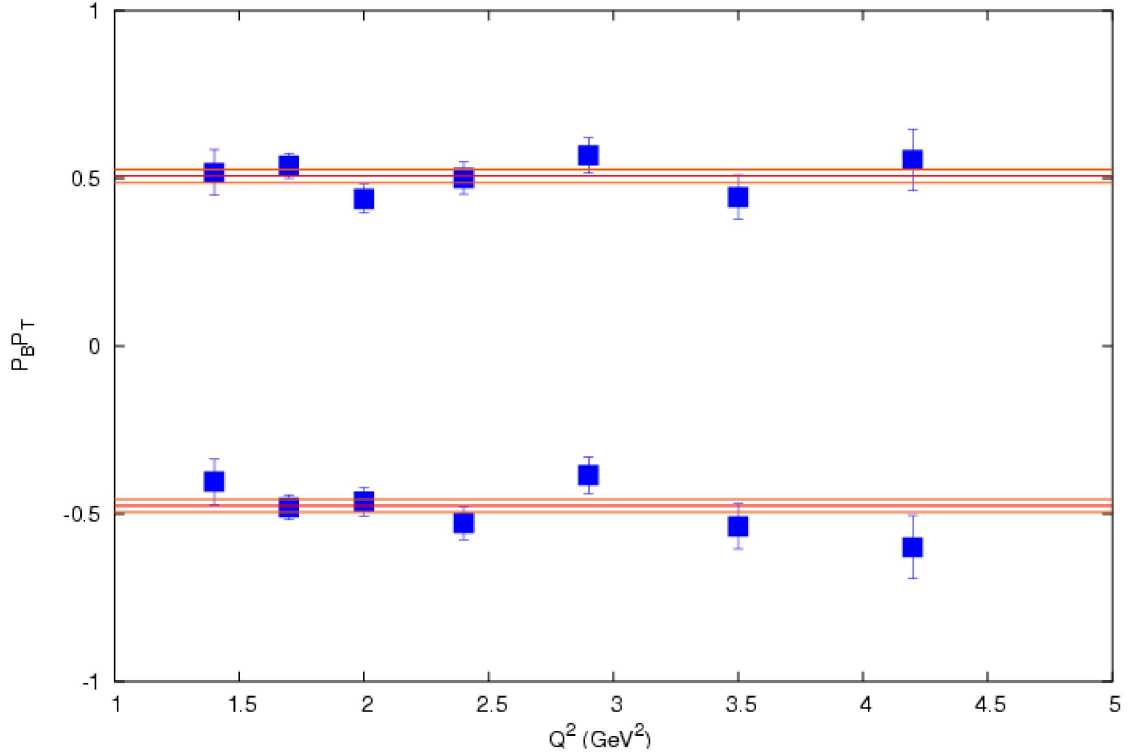
Figure 4.7: A plot of the measured $P_B P_T$ values for a specific setting (in this case 4.2 GeV, in-bending electrons) as a function of Q^2. As expected, the values for $P_B P_T$ have no Q^2 dependence. The lines represent the error weighted sums of the points for each target configuration (positive or negative target polarization) and the statistical error associated with each of these averages.

4.8 Raster Correction

In order to reduce effects on the polarization that can occur from beam heating, or as mentioned in section 3.8, the depolarization that is associated with the accumulated beam charge on the target, it is necessary to raster the beam over the surface of the target. Rastering the beam is the process of moving the beam by small amounts, perpendicular to the beam line relatively quickly in time, in a pattern that traces out the same amount of area on the target face per unit time regardless of where the beam spot is. This distributes the beam over the surface of the target. The tracking assumes

that the x and y positions (the directions perpendicular the direction of the beam) of the beam are zero when it calculates p_x (the momentum in the x direction, p_y (the momentum in the y direction, or v_z (the point in z at which the scattering occurred). The fact that the x and y positions were not zero can result in a miscalculation of p_x, p_y, and v_z meaning the particle travels a different distance through the target magnetic field than that used by the tracking software to reconstruct the path. For charged particles, this means that the particles trajectories were bent for a different amount than was accounted for. This effect can be accounted for by knowing the position of the beam at each event [43]. This information was obtained by using the stored ADC values for the raster magnet currents on an event by event basis to determine the x and y positions of the beam spot, as described in section 4.8.3.

4.8.1 z vertex

The z vertex, v_z, must be corrected by a factor:

$$V_z' = V_z + \frac{x'}{\tan \theta} \tag{4.24}$$

where V_z' is the corrected z vertex position, V_z is the z vertex position found by the tracking software, θ is the angle of the particle trajectory relative to the beam line, and x' is the total distance that the particle traveled which the tracking software neglected.

$$x' = \frac{x \cos \phi_0 + y \sin \phi_0}{\cos \phi - \phi_0} \tag{4.25}$$

where ϕ is defined as the azimuthal angle of the particle $(\tan^{-1} \frac{p_y}{p_x})$, and ϕ_0 is the angle that corresponds to the center of the sector where particle was detected.

4.8.2 Azimuthal Angle

Since the distance that the particle traveled in the target field is different than origi-
nally determined, the tracking software incorrectly calculated the rotation in ϕ caused
by the high magnetic field in the region of the target. ϕ can be corrected, since the
field is known and the correct path length is known. This amounts to a correction to
p_x and p_y that preserves the product $p_t = p_x p_y$ as shown in Eq. 4.26 with q being the
charge of the particle, 50 being the target field in kilogauss, 100 being a conversion
from centimeters to meters, and 33.356 the inverse of the speed of light in appropriate
units.

$$\phi_c = \phi + q \cdot 50 \cdot \frac{x'}{100} / (\frac{33.356}{p_t})$$ (4.26)

4.8.3 Determining x and y

In order to perform the corrections that were just described, it is necessary to know
the x and y positions of the beam spot for each event. Since there is no direct
measurement of this, the values of x and y must be determined from some other piece
of information. The output of the power supplies that controlled the raster magnets
was recorded in an ADC. In order to use these values, it is necessary to translate the
ADC values into position (in x and y). The coordinates were determined by fitting
the z vertex positions of the electron and proton for exclusive events. The z vertex
positions should be identical, but are not, due to the error in tracking caused by the
raster.

The x and y positions are related to the ADC values by:

$$x = (ADC_x \quad - \quad ADC_x^0) \cdot C_x \tag{4.27}$$

$$y = (ADC_y \quad - \quad ADC_y^0) \cdot C_y \tag{4.28}$$

ADC_x and ADC_y are the ADC values for x and y respectively, ADC_x^0 and ADC_y^0 are the ADC values that correspond to the center of the target, and C_x and C_y are the constants that go from ADC counts to centimeters.

For elastic $ep \rightarrow e'p$ events, the difference in vertex positions of the proton and electron is calculated as a function of the parameters ADC_x^0, ADC_y^0, C_x and C_y. The difference was then minimized using MINUIT for each NH_3 run. The values where then fit in the regions where the physical position of the target was stable (the position of the target would often change slightly due to a change of the material) and the beam energy and optics were stable (a change of beam energy would require different raster magnet currents for the same deflection in x or y).

4.9 Momentum Corrections

The reconstruction of particle trajectories and momentums be the tracking software requires a very accurate knowledge of the CLAS detector, especially the drift chambers. The momentum of the particles can be reconstructed incorrectly due the torus field being slightly different from the field map used by the reconstruction software (this is known to be a problem for some runs, and was the result of a software error), or mis-alignment of the wires in the drift chamber (additionally, the wires can sag and shift over time, resulting in additional errors). Both of these sources of error are dependent on the place in the drift chamber that the particle passes through.

The error results in a broadening and shifting of the neutron peak in the missing mass spectrum. The momentum of the particles can be corrected on a an event by event basis to fix this problem. The correction necessary is determined by analyzing multi-particle events. The exact process is discussed in great detail in Ref. [44]. The result is a narrowing of the peak in W spectrum and the missing mass spectrum of the neutral particle in the $ep \rightarrow e'\pi^+ N$ reaction, as shown in Fig. 4.8.
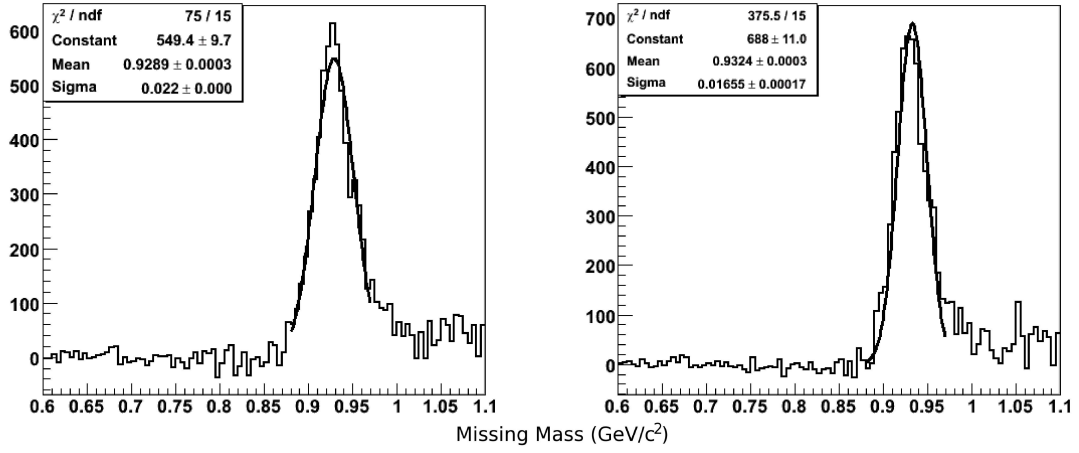

Figure 4.8: The effect of the momentum corrections on the missing mass peak for the neutron. The plot on the left is the peak with no momentum correction applied, the right is with momentum correction applied. In both cases a Gaussian has been fit in the region of the neutron to better highlight the size and position of the peak. The correction narrows the peak substantially as well as adjusting the position of the peak to be closer to the mass of the neutron.

4.9.1 Multiple Scattering and Stray Magnetic Field Correction

In addition to the momentum correction necessary to allow for the mis-alignment of wires in the drift chambers, there is a correction to the momentum of the particles to account for the multiple scattering that can occur in the target. There is also an effect

from the small target field that exists outside of the first region of the drift chamber (the tracking software assumes that the field in this region is zero when calculating momentums and angles).

Much like the raster correction, the angle ϕ for each charged particle must be corrected in order to account for this extra magnetic field. In addition, multiple scattering can result in an offset in the z vertex position for events. This, again, results in an incorrect reconstruction of the momentum of a particle due to the different path length of the particle in the target field. The multiple scattering correction uses the weighted average of all of the reconstructed vertex positions in each event to estimate the amount of energy that would be lost by the scattered particles and correct the momentum, and angles accordingly. All of the corrections have been parametrized as a function of the particle momentum [45], and applied to every charged particle.

4.9.2 Energy Loss

There is an additional correction to account for the energy that the beam can lose upstream of the scattering point. This correction is performed by determining the average reconstructed vertex (this is the vertex which has been corrected for both rastering effects and for multiple scattering and stray field effects) for all of the particles in the event, and assuming that this is likely the location where the scattering actually occurred. The beam energy used in all kinematic calculations is then adjusted to account for the energy lost.

4.9.3 Order of Corrections

It is worthwhile to notice that the momentum corrections, raster correction, multiple scattering correction, stray magnetic field correction and energy loss correction are

not independent of each other. This is immediately apparent by the fact that a great many of them rely on correcting the z vertex position of the event, or using the z vertex position of an event to determine the amount of material that particle passes through. Great care was given to ensuring that the corrections were applied and calculated in the correct order. The correction must be applied in the order they were calculated (for example, the multiple scattering and stray field corrections must be applied after the raster correction, because the parameters for this correction were determined using events which had the raster correction applied).

4.10   Fiducial Cuts

In general, it is useful to place a geometrical cut on the efficient regions of the Čerenkov detector. This makes sure the particles being identified as electrons by the Čerenkov are from a region where the detector is reliable. The fiducial region of the detector must be determined by looking at the expected number of photo-electrons that should be produced by an electron. This number is determined from a model of the Čerenkov response. If the expected number of photo-electrons is too small, then that region is deemed too inefficient to be reliable and is excluded. Similarly, regions which are known to include the PMTs or other obstructions are removed.

For this analysis, the fiducial cuts are not necessary, as the exclusive nature of the event greatly decreases the any pion contamination in the electron sample. In addition, the fact that the data is analyzed in very small bins in four dimensions limits any effect the non-uniform efficiency could have on the asymmetry. The advantage of not using the fiducial cuts in this analysis is that it increases the statistical sample, especially in the regions that are on the edge of the detector acceptance (very low Q^2 for example).

Chapter 5

Results

5.1   The Double Spin Asymmetry, A_{et}

The asymmetry has been determined as a function of W, Q^2, $\cos\theta^*$, and ϕ^* as previously mentioned. The end result of the asymmetry analysis is a large table of values, one value for each of the four dimensional kinematic bins that the asymmetry was measured in. The data was measured in 50 (30MeV) W bins, 40 Q^2 bins, 10 $\cos\theta^*$ bins and 10 ϕ^* bins. This table is useful in constraining models, as it offers a large number of data points over a wide kinematic range. The results of this analysis will be shown, but it is important to note that the plots shown here will always have at least one variable averaged over. In all of the plots, when there has been an averaging over variables, it is the asymmetry that has been averaged, using the error on the asymmetry as a weight. This technique is used because the asymmetry in any given bin is independent of the acceptance of that bin, but only if the acceptance does not change drastically over the width of that bin. In this fashion, the asymmetries can be analyzed without the need for a model of the detector acceptance.

In the four dimensional table, the average kinematic values for each bin are also

calculated. This is done to reflect the possible changes in the value of the asymmetry over the range of a bin. This effect is small, since the bins are small. However, when a given kinematic variable is averaged over, the average of that kinematic value must also be calculated. This is done using a weighted sum of the kinematic value for each bin using the error on the asymmetry as the weight.

The value of A_{et} is shown as a function of each kinematic variable in Figs. 5.1, 5.2, 5.3, and 5.4. In each case, the asymmetry has been averaged in all of the other variables as described above.
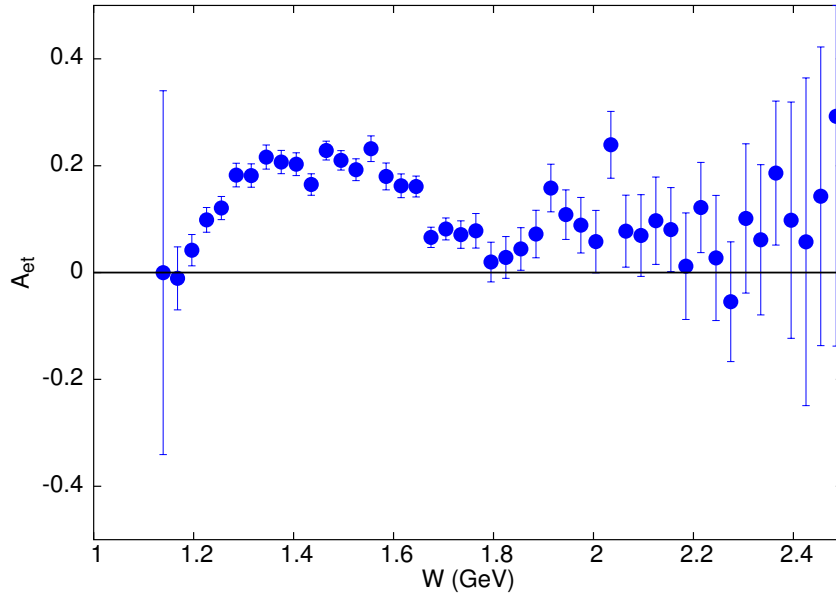

Figure 5.1: A_{et} as a function of W for the 4.2 GeV data set. The asymmetry has been averaged over Q^2, $\cos\theta^*$, and ϕ^*.

While plots of A_{et} averaged over three kinematic variables are useful for displaying the high statistics associated with this measurement, it is more useful to display the results as slices in different kinematic variables. Specifically, it is extremely useful to look at the asymmetry as a function of Q^2, ϕ^* or $\cos\theta^*$ for fixed values of W, as this allows for some insight into how specific resonances are contributing to the asymmetry. Figures B.1 through B.4 in Appendix B show the asymmetry as a function of Q^2,
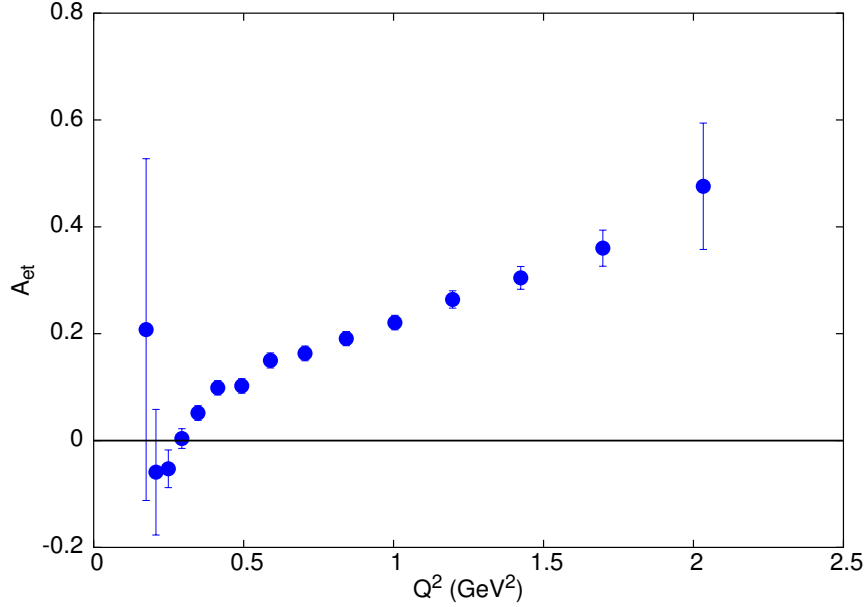
Figure 5.2: A_{et} as a function of Q^2 for the 4.2 GeV data set. The asymmetry has been averaged over W, $\cos\theta^*$, and ϕ^*.

averaged over $\cos\theta^*$ and ϕ^*, for each W bin. These plots show the Q^2 dependence of the response functions for each resonance region. Similarly, the asymmetry can be shown as a function of $\cos\theta^*$ for each bin in W, this time averaged over Q^2 and ϕ^* as in Figures B.5 through B.8 in Appendix B. There are also plots (Figures B.9 through B.12 in Appendix B) with the asymmetry as a function of ϕ^* for fixed values of W, averaged over the other two variables. All of the plots are shown along with the results for the MAID2003 (as mentioned in Section 1.4.3) model for the same kinematics. The results from MAID were calculated in the same four dimensional matrix as the data were measured, at the average kinematic value for each four-dimensional bin.

To display the results for a specific resonance, it is interesting to look at plots of the asymmetry as a function of Q^2, for fixed values of W and $\cos\theta^*$, averaged over ϕ^*. Fixing W at the location of a specific resonance (the Roper resonance, for example), allows the structure of that specific resonance to be measured. The plots in Fig. 5.5 are shown along with the results for the MAID2003 model for the same kinematics
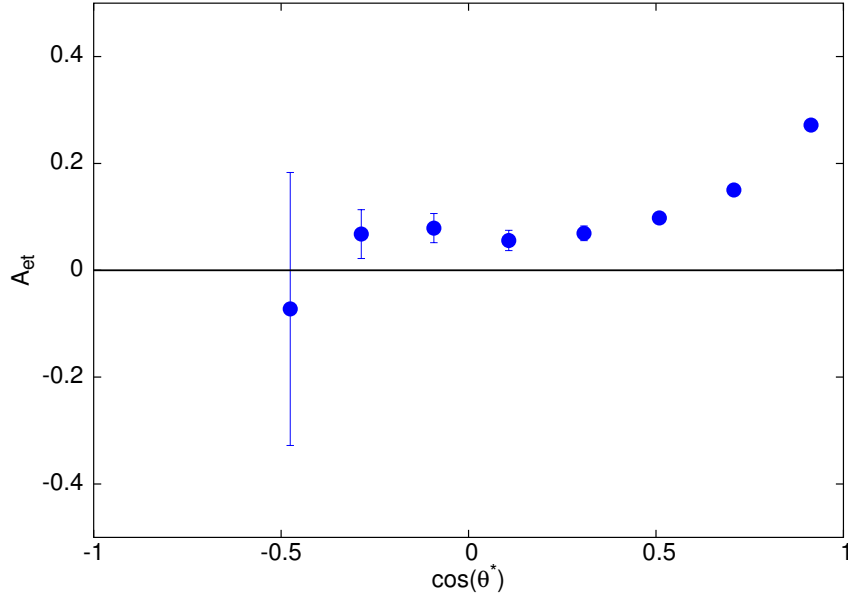
Figure 5.3: A_{et} as a function of $\cos\theta^*$ for the 4.2 GeV data set. The asymmetry has been averaged over W, Q^2, and ϕ^*.

with a fixed value of W for all of the plots, and each plot representing a different $\cos\theta^*$ bin.

The ϕ^* dependence of the asymmetry can also be explored. Since the overall functional form for the asymmetry in terms of ϕ^* is already known from equation 1.16, different parts of the asymmetry can be separated, for instance, by looking at the asymmetry for a fixed value of $\phi^* = \frac{\pi}{2}$. In this case, the contributions of $R^x_{LT'}$, $R^z_{LT'}$, and $R^x_{TT'}$ all vanish, leaving only, $R^y_{LT'}$, and $R^z_{TT'}$. A plot of the asymmetry for $\phi^* = \frac{\pi}{2}$ as a function of W (averaged over Q^2 and $\cos\theta^*$) is shown in Fig. 5.6.

Since it can be difficult to determine the significance of the deviations from the results from MAID, the weighted average of the difference between the measured value of A_{et} and MAID is shown in Fig. 5.7 as a function of W. Deviations much greater than the error would suggest places where MAID can perhaps be improved.
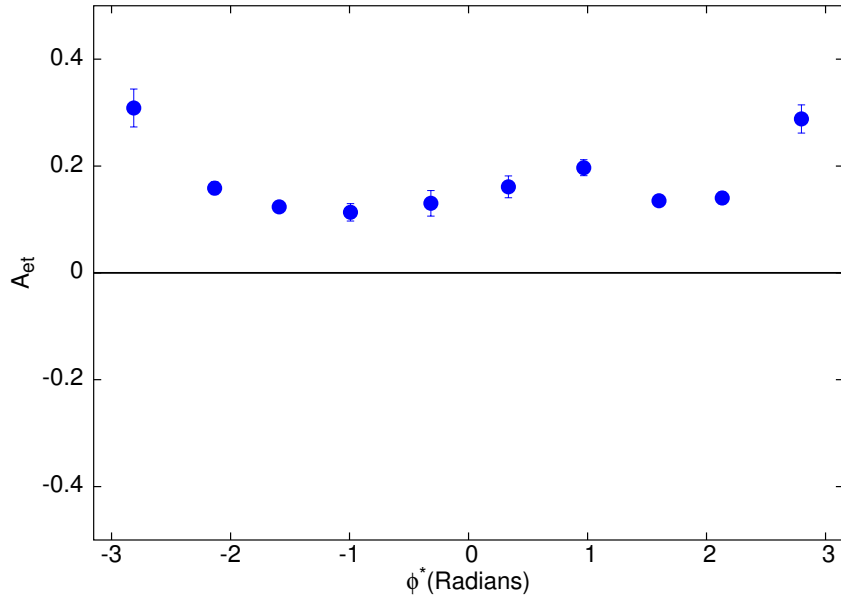
Figure 5.4: A_{et} as a function of ϕ^* for the 4.2 GeV data set. The asymmetry has been averaged over W, Q^2, and $\cos\theta^*$.
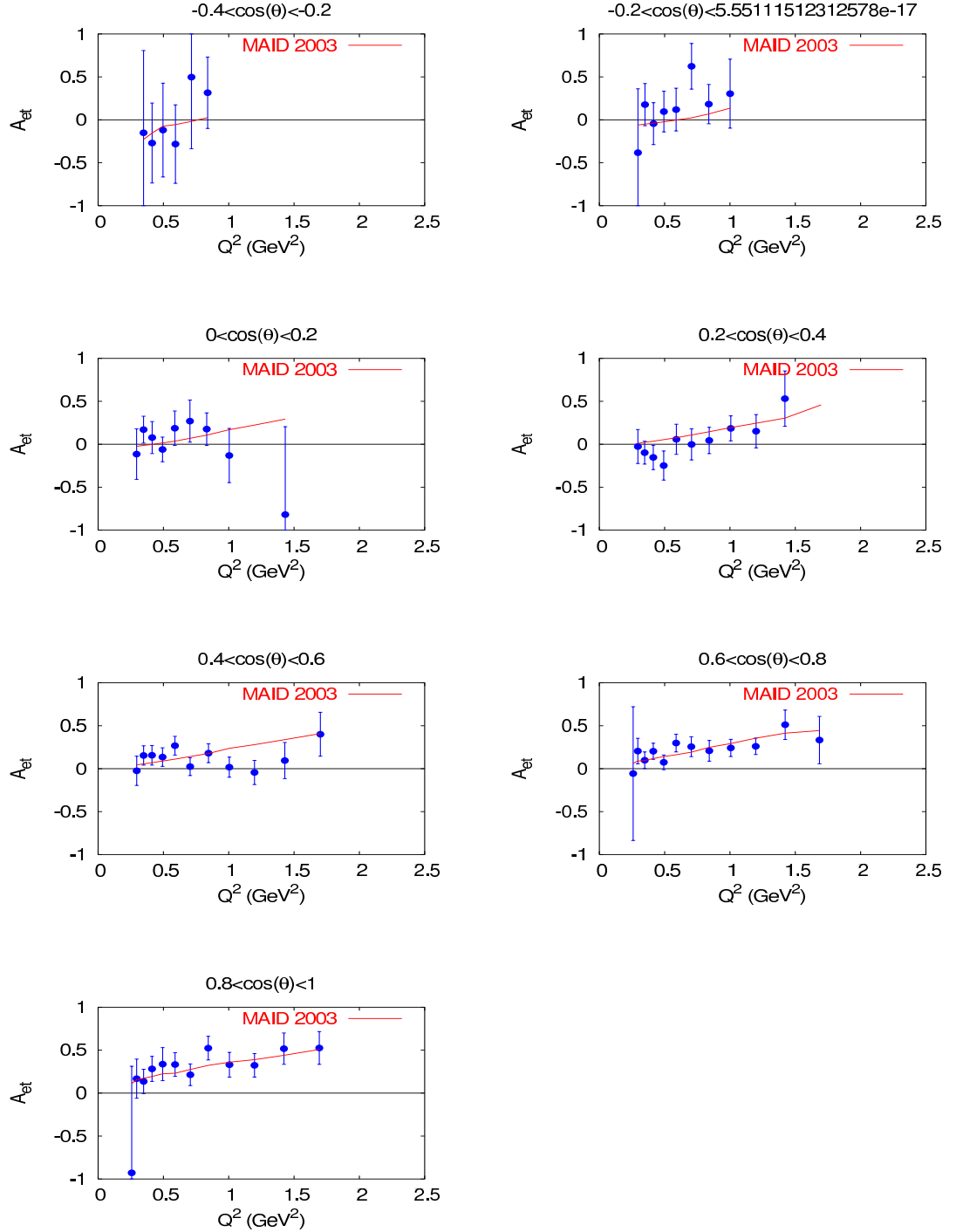
Figure 5.5: A_{et} as a function of Q^2 for each $\cos\theta^*$ bin, with $1.43 < W < 1.46$ GeV. The asymmetry has been averaged over ϕ^*. To compare the results to those from other experiments, the value from MAID2003 is also shown.
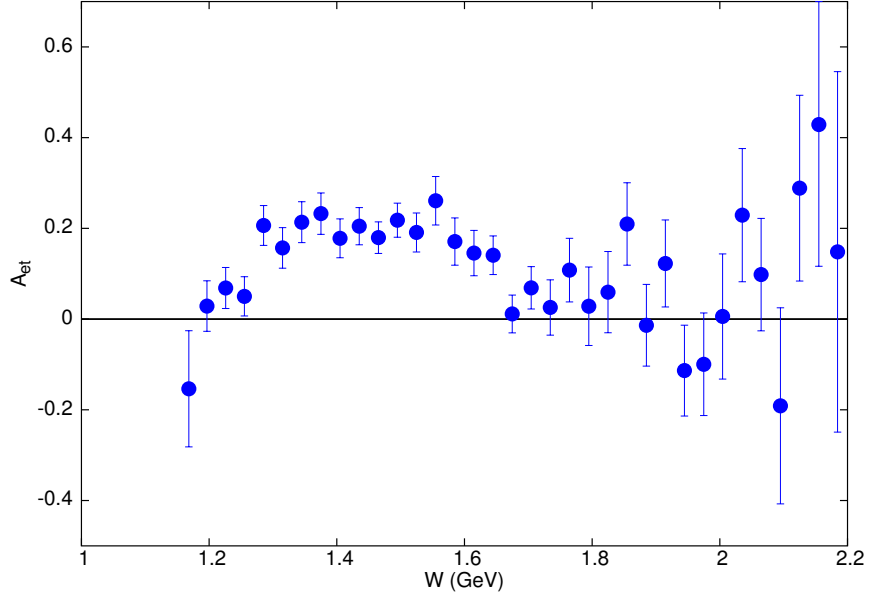
Figure 5.6: A_{et} as a function of W for the 4.2 GeV data set for a fixed value of $\phi^* = \frac{\pi}{2}$. The asymmetry has been averaged over Q^2 and $\cos\theta^*$. For this value of ϕ^* several of the response functions have no contribution to the asymmetry.
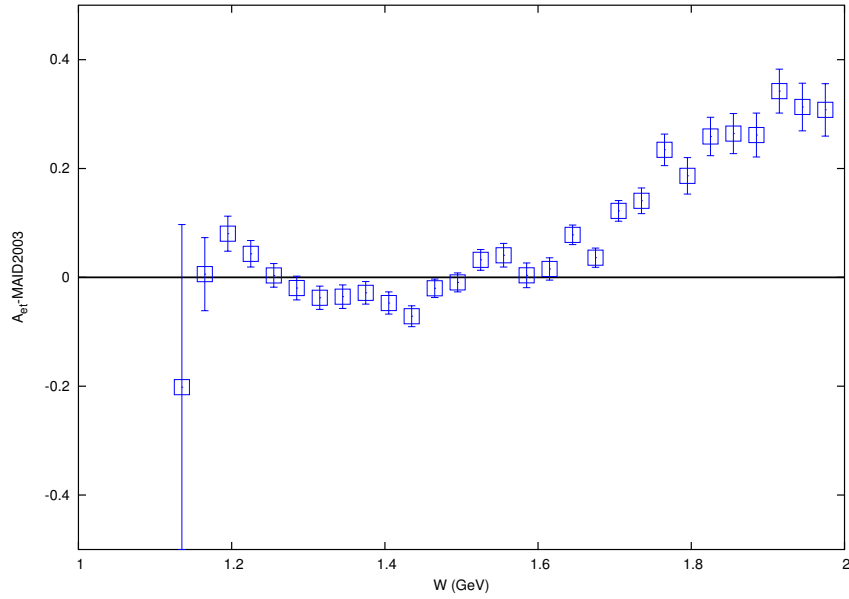

Figure 5.7: The weighted average of the difference between A_{et} as determined from this analysis and the value from MAID2003 as a function of W.

5.2   The Single Spin Asymmetry, A_e

The single spin asymmetry can be constructed from the same data as shown in Eq. 4.9. As mentioned in section 1.4.2, A_e is the best known of the asymmetries. This is due the the lack of a requirement for the target to be polarized, and the fact the the value for σ_e is dependent on a single response function $R_{LT'}$ with a simple $\sin\phi^*$ dependence, as can be seen from Eq. 1.14. The straightforward angular dependence and the relative accuracy to which this asymmetry has been measured makes it useful as a check of the analysis of the double spin asymmetry A_{et} and the single target spin asymmetry A_t. The ϕ^* dependence of A_e is plotted in Fig. 5.8, along with the expected values as determined by MAID2003. Unlike the the double spin asymmetry, A_e is expected to agree extremely well with MAID, since there is much more data on this asymmetry which has been incorporated into the model.

The ϕ^* dependence of the single spin asymmetry can also be exploited as a way to check the various inputs to the asymmetry calculation, for example the relative polarizations from the different helicity states. This can be done by measuring the single spin asymmetry at $\phi^* = 0$ and checking for systematic deviations from zero. If there is a systematic, non-zero asymmetry when $\phi^* = 0$, that indicates an error of some sort in the asymmetry measurement. The asymmetry A_e when $\phi^* = 0$ is shown as a function of W in Fig. 5.9. There does not appear to be any systematic deviation from zero, the χ^2 per degree of freedom between the result and zero is 1.237.

5.3   The Single Spin Asymmetry, A_t

The target spin asymmetry, A_t, can also be extracted, using yet another combination of helicity states as shown in Eq. 4.10. This asymmetry has a much more complicated

dependence upon the response functions than A_e, with terms containing several response functions and different angular dependencies. It does, however, share a trait with A_e in that neither is easily displayed as a quantity which has been averaged over ϕ^*. A_t contains only $\sin\phi^*$ and $\sin 2\phi^*$, both of which would average to zero if the average was conducted over the entire range of ϕ^*. It is straightforward to display the asymmetry as a function of ϕ^* for fixed values of $\cos\theta^*$, as was done for A_e. This is shown in Fig. 5.10.
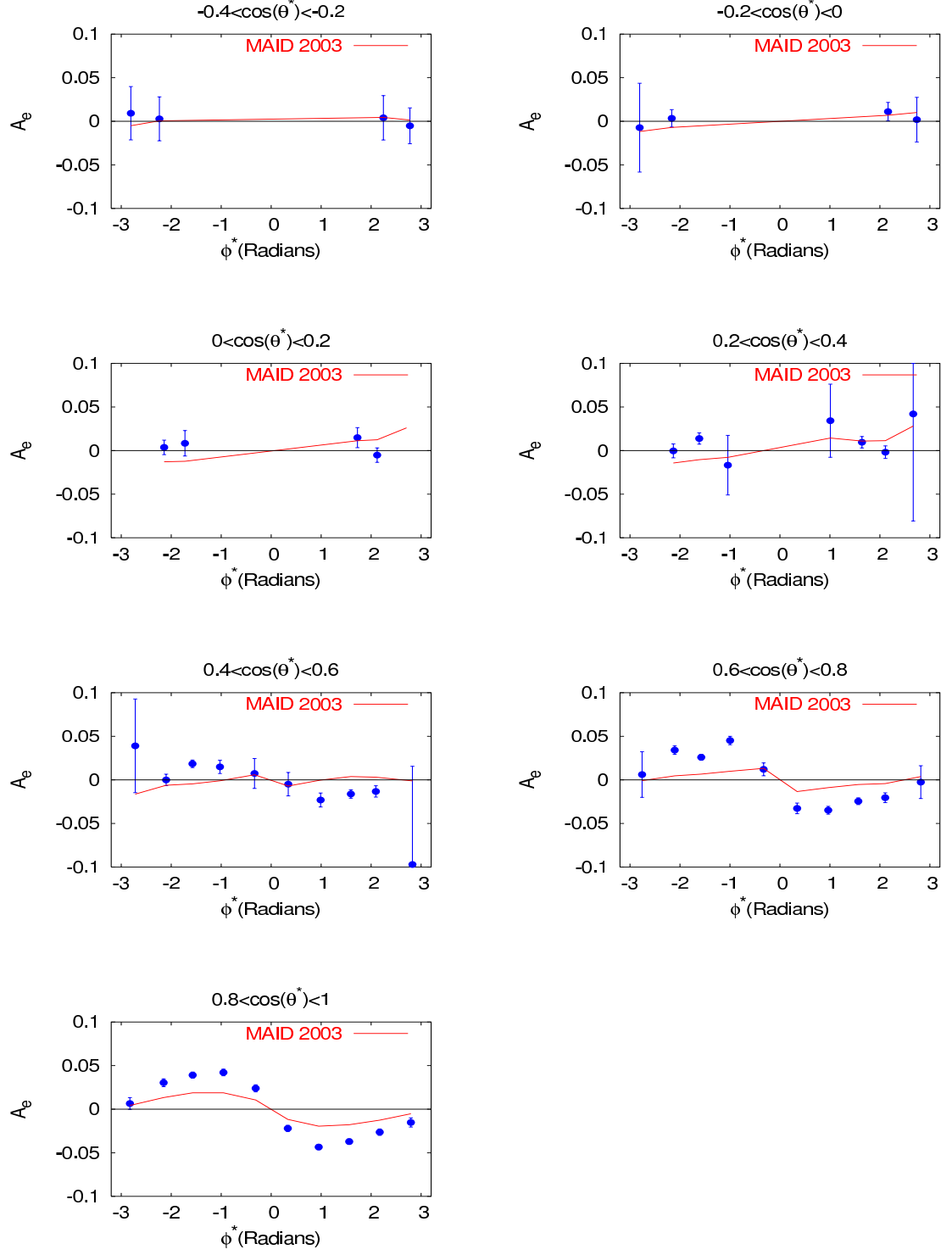
Figure 5.8: A_e as a function of ϕ^* for the 4.2 GeV data set for each $\cos\theta^*$ bin. The asymmetry has been averaged over W and Q^2. The solid line expected values of the asymmetry from MAID.
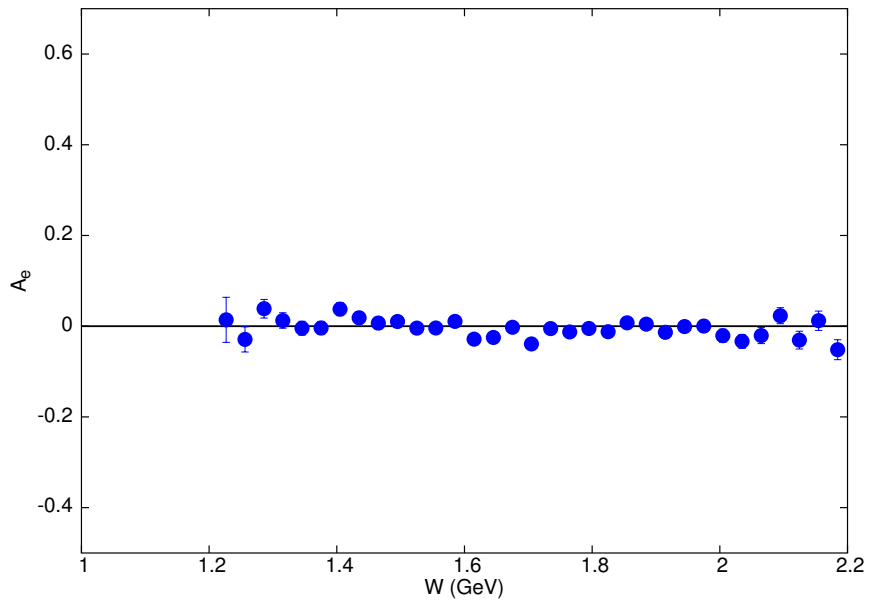
Figure 5.9: A_e as a function of W for the 4.2 GeV data set, with $\phi^* = 0$. The asymmetry has been averaged over Q^2 and $\cos\theta^*$. The value of the asymmetry appears to be consistent with zero, as is expected from Eq. 1.14.
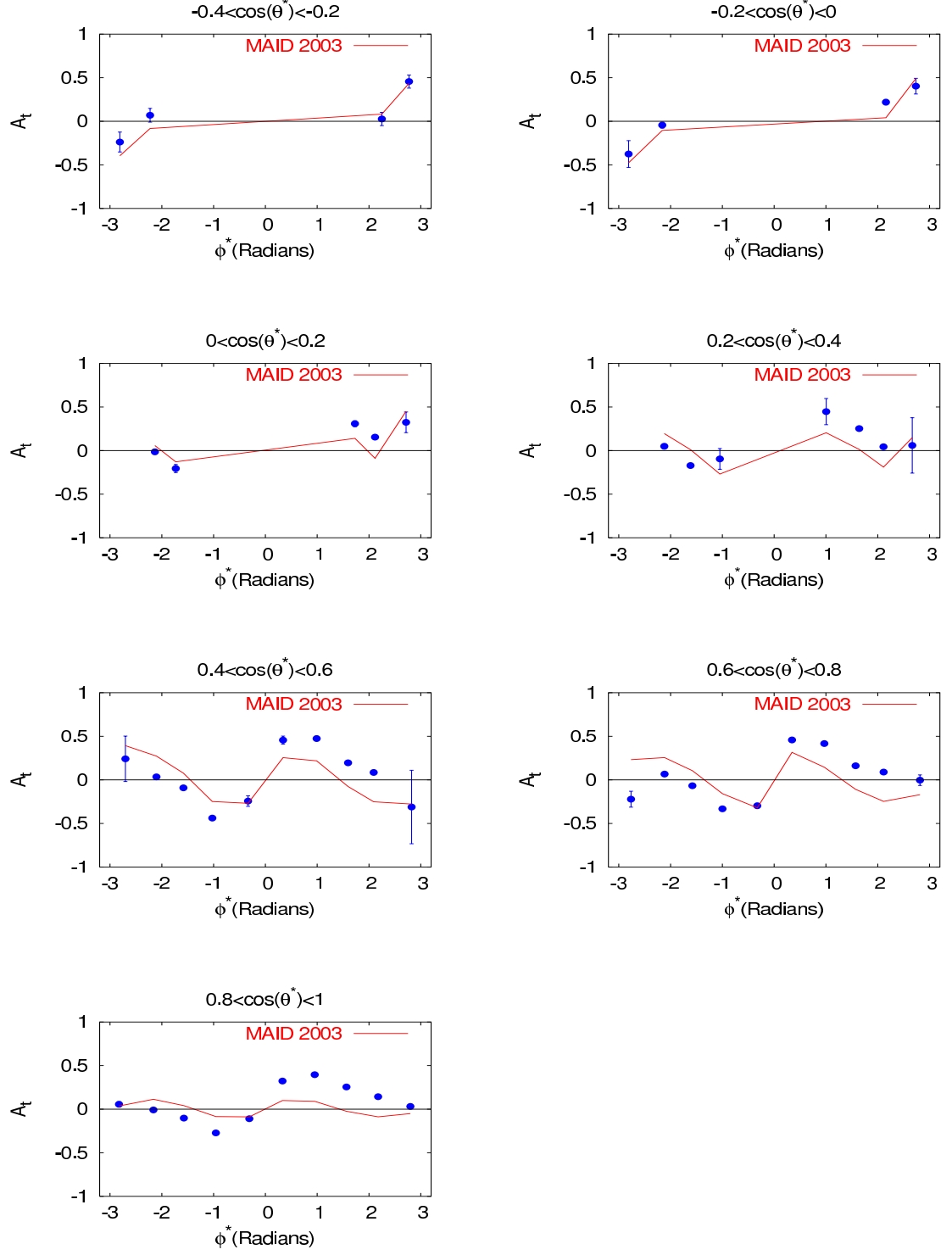
Figure 5.10: A_t as a function of ϕ^* for the 4.2 GeV data set for each $\cos\theta^*$ bin. The asymmetry has been averaged over W and Q^2. The solid line is the expected values of the asymmetry from MAID.

5.4   Systematic Errors

Since there is no model dependence present in the analysis (with the exception of the determination of $P_B P_T$, the error analysis of which will be discussed later) most of the systematic errors are the results of cuts, event selection, and efficiency factors.

5.4.1   Dilution

As discussed in Section 4.6, the ^{15}N background contribution to the scattering has been modeled by scaling the ^{12}C missing mass spectrum to the NH$_3$ spectrum in the the region below the neutron mass. The statistical error associated with the carbon counts in each bin has already been propagated into the overall statistical error for the asymmetry. However, there is also an error associated with the factor used to scale the ^{12}C counts. This scale factor was determined as a function of $\cos\theta^*$ only, as that is the variable that has the largest effect on the value. While this is a statistical error associated with the number of ^{12}C counts and NH$_3$ counts, the fact that the scale only depends on $\cos\theta^*$ means that it needs to be treated as a systematic error in $\cos\theta^*$. The error on the ratio of counts is a simple statistical error, and has a value of 2.5% to 7.3%. The value of this ratio as well as the error is shown, separately for the in-bending and out-bending data in Fig. 5.11.

To evaluate the effect of this error on the asymmetry, that analysis was performed with the ratio varied from the calculated values by the standard deviation. The result of this modified analysis is shown in Fig. 5.12 as a function of $\cos\theta^*$, averaged over the other kinematic variables, compared to the same result for the standard analysis. The results seem to be compatible within statistics with an average difference of $0.0008 +/- 0.01$. This value is heavily weighted toward the region which has the highest statistics on the asymmetry, which also has the lowest error on the ^{15}N to ^{12}C
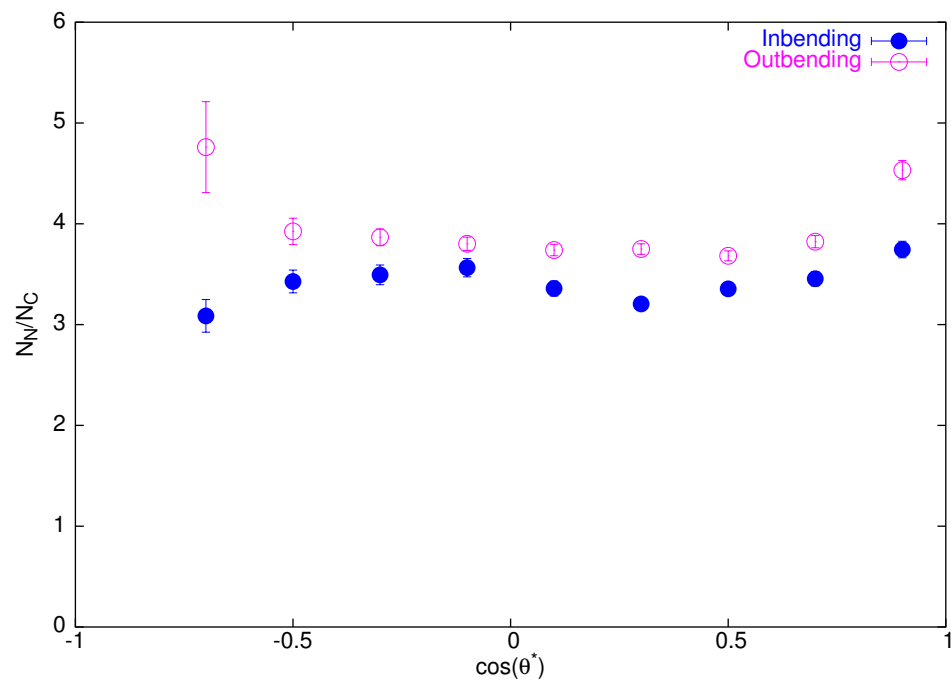
Figure 5.11: The ratio of counts from NH_3 to the counts from ^{12}C from events with a missing mass less than the mass of the neutron. This is the ratio used to normalize the ^{12}C spectrum to the ^{15}N spectrum in order to take the background into account. The statistical error on these points enters as a systematic error on the asymmetry.
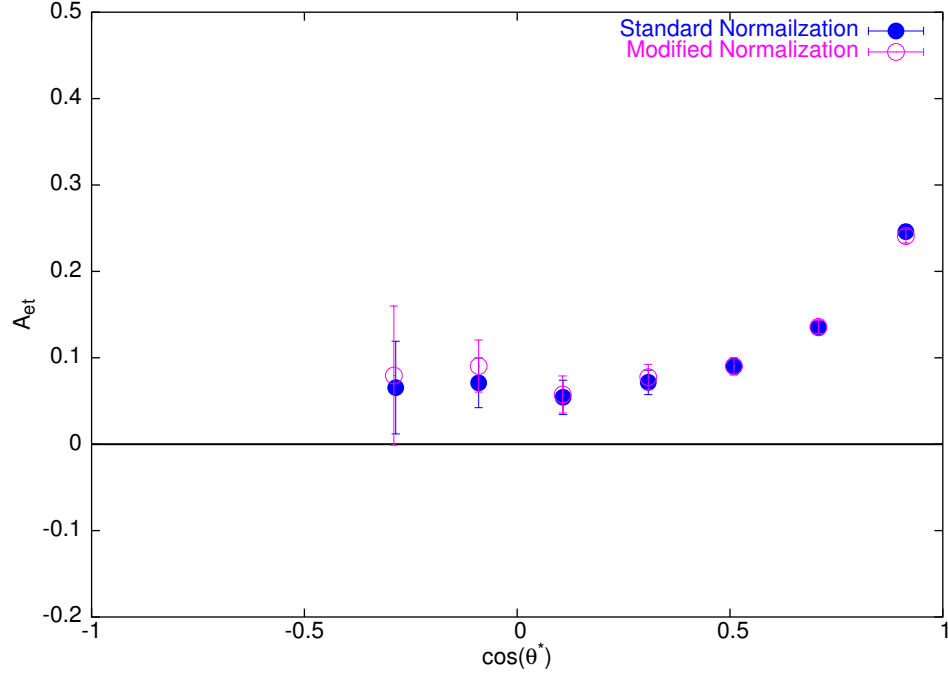
Figure 5.12: A_{et} as a function of $\cos\theta^*$ for the standard analysis compared to the analysis performed with the modified values of the ^{15}N to ^{12}C count ratio.

count ratio.

5.4.2 Efficiency and Acceptance

The asymmetry is independent of the efficiency and acceptance of the detector only so long as the acceptance does not change too dramatically across a given kinematic bin. This is assured for suitably small bins, but the exact size of bin for which the acceptance variation can be ignored is difficult to determine. Some of the acceptance effects that could possibly occur result in a simple shift of the central kinematic value of the bin. These are taken into account by the average kinematic value for the events in each bin being reported, as opposed to the central value of the bin. Still, it is worthwhile to check for additional acceptance effects.

There are some simple tests of the acceptance effects. The first of these is to
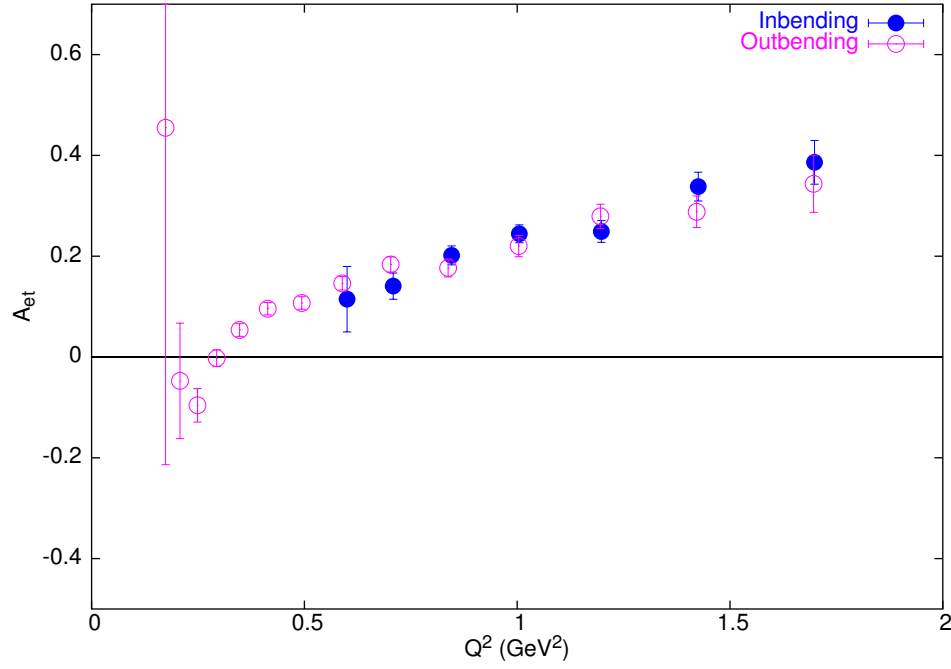
Figure 5.13: A_{et} as a function of Q^2 for the analysis of events from the in-bending torus configuration as well as the out-bending configuration. The two results appear to be within statistical error, and an overall χ^2 analysis supports that conclusion.

compare the data taken in the in-bending torus configuration to the data taken in the out-bending torus configuration. These represent two completely separate statistical samples with very different acceptances for both electrons and pions. Where the two sets of data have overlapping kinematic coverage, a χ^2 test of compatibility between the samples should reveal any effect from detector acceptance. The double spin asymmetry for the in-bending and out-bending torus configurations is shown in Fig. 5.13 as a function of Q^2. The χ^2_ν between these two distributions is 0.587 and the average difference is $0.0241 +/- 0.0164$.

Another useful test is to run the entire analysis with one of the six sectors, sector five is randomly chosen, of the CLAS detector turned off (only accepting events where neither the electron or the pion was detected in sector five of CLAS), and compare this asymmetry to the one obtained with the analysis of events where at least one
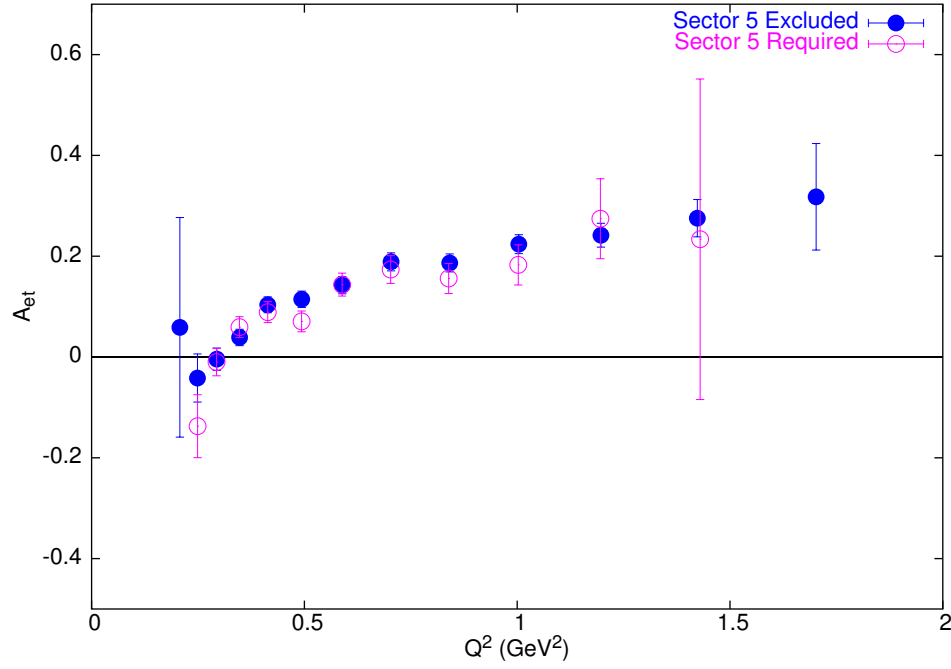
Figure 5.14: A_{et} as a function of Q^2 for the analysis of events where no particle was detected in sector five and the asymmetry for the analysis where one particle was required to be detected in sector five. The results are well within statistical error.

of the particles was detected in sector five. The advantage of this method is that it greatly alters the efficiency of the detector, without actually affecting the kinematic coverage. This has been done, and the asymmetry as a function of Q^2 is shown for both the standard analysis, and the five sector analysis in Fig. 5.14. The agreement is very good, with a χ^2_ν value of 0.61 and a average difference of $0.0361 + / - 0.0124$.

Additionally, the effects of varying acceptance and efficiency can be checked by changing the bin size. The size of the ϕ^* bins was doubled. This should have the effect of exacerbating any affects from the change of the acceptance over a bin, while again keeping the kinematic coverage constant. A lack of difference in the asymmetry would imply that the bins were suitably small to ignore the acceptance in each bin. Fig. 5.15 shows the asymmetry for the normal binning compared to the large binning. Again, the results are well within statistical errors, with a χ^2_ν value of 0.345 and an
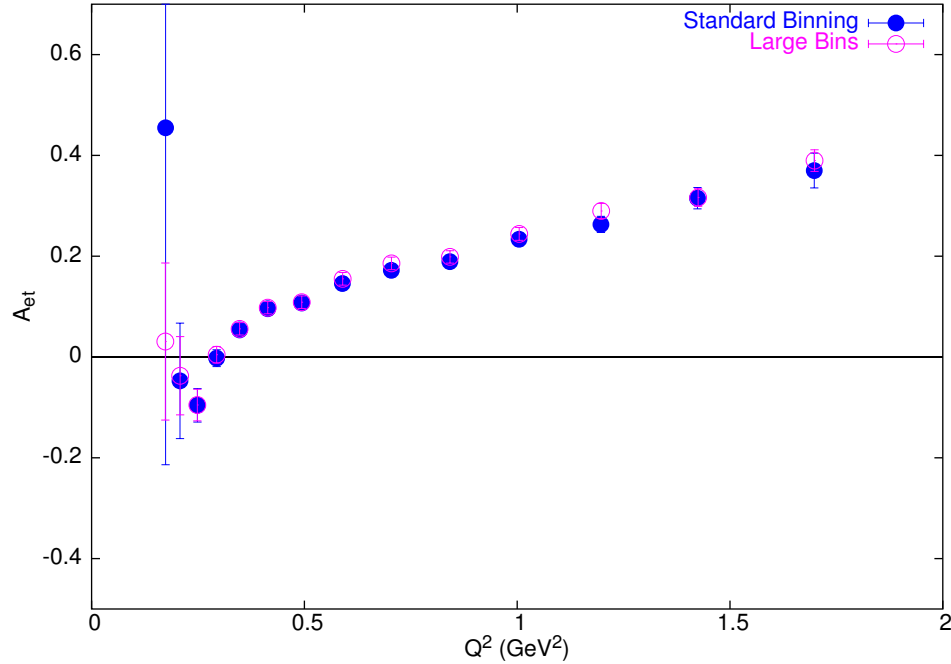
Figure 5.15: A_{et} as a function of Q^2 for the standard analysis and the analysis with large ϕ^* bins. If the variation of the acceptance or the efficiency over the course of a bin were impacting the asymmetry, the effect would be expected to increase as the bins became large. The results appear within statistical error, implying that the bins are small enough, and have a slowly enough variation in acceptance.

average deviation of $-0.0156 +/- 0.0069$. However, since the two results do not represent statistically separate groups of data, meaning that no real conclusion can be drawn from the χ^2_ν value, but a relatively small average deviation is indicative of a small effect.

5.4.3 Event Selection

There can also be systematic effects from the event selection cuts, especially the neutron missing mass cut and the electron identification. The effect of the missing mass cut can be checked by analyzing the asymmetry with a much more narrow missing mass cut, and comparing the results to the asymmetry from events which are included in the standard analysis, but would be excluded from the more restrictive
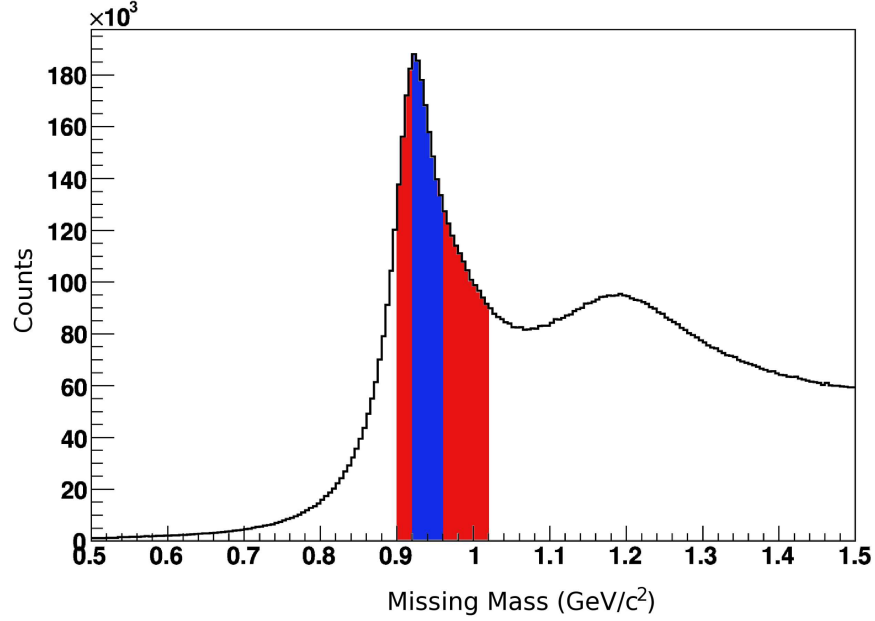
Figure 5.16: The two regions within the standard missing mass cut cut that are used to determine the effects of event selection.

cut. This has been done, with the standard cut of 0.9 GeV$< M_x <$ 1.02 GeV being changed to 0.92 GeV$< M_x <$ 0.96GeV. The regions which are compared can be easily seen in Figure 5.16. The effect on the asymmetry is very small and within statistical error for most of the range, with larger differences for the higher W range. The average difference is $0.0087 +/- 0.0156$ with a χ^2_ν of 0.850. Fig. 5.17 shows this comparison.

5.4.4 $P_B P_T$

The error in evaluating the polarization of the beam and target enters into the error on the asymmetry through the overall normalization of the polarization, as well as the constants α_e and α_t. The statistical error for both polarizations are taken into account independently. In addition, there are systematic errors in the calculation of
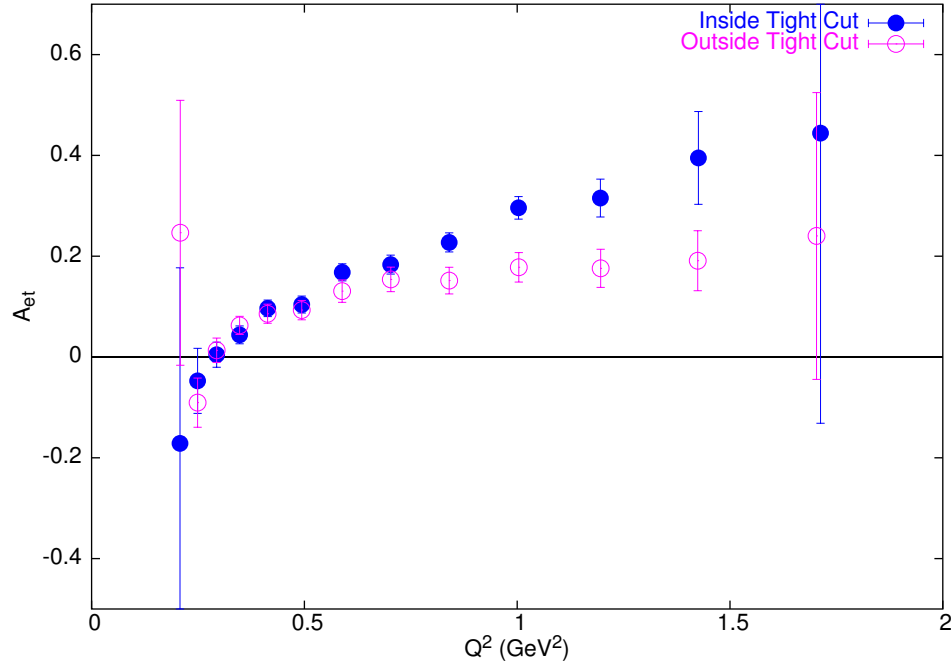
Figure 5.17: A_{et} as a function of Q^2 for the more restrictive cut of 0.92 GeV$< M_x <$ 0.96 compared to the asymmetry from events which fall outside the restrictive cut, but within the standard cut.

$P_B P_T$ to be considered. Most notable is the formula that is used to determine the elastic asymmetry. The value of the asymmetry is dependent on several kinematic factors and the ratio r as defined in Eq. 4.22. The value that was used was determined from recoil polarization experiments, as discussed in Section 4.7, the result of which differ from previous measurements of r, which historically found the the value of r was more of a constant. In order to test the dependence of $P_B P_T$ on this choice, a constant value of $r = 2.79$ was used for comparison. A comparison of the results for $P_B P_T$ are shown in Fig. 5.18 for each Q^2 point that was used in the average. As can be seen, the results are nearly indistinguishable. The difference between the averages is less than 1%, relative.

Much as the event selection cuts for the exclusive analysis were checked for systematic effects, so were the cuts that were used to determine the exclusive nature of
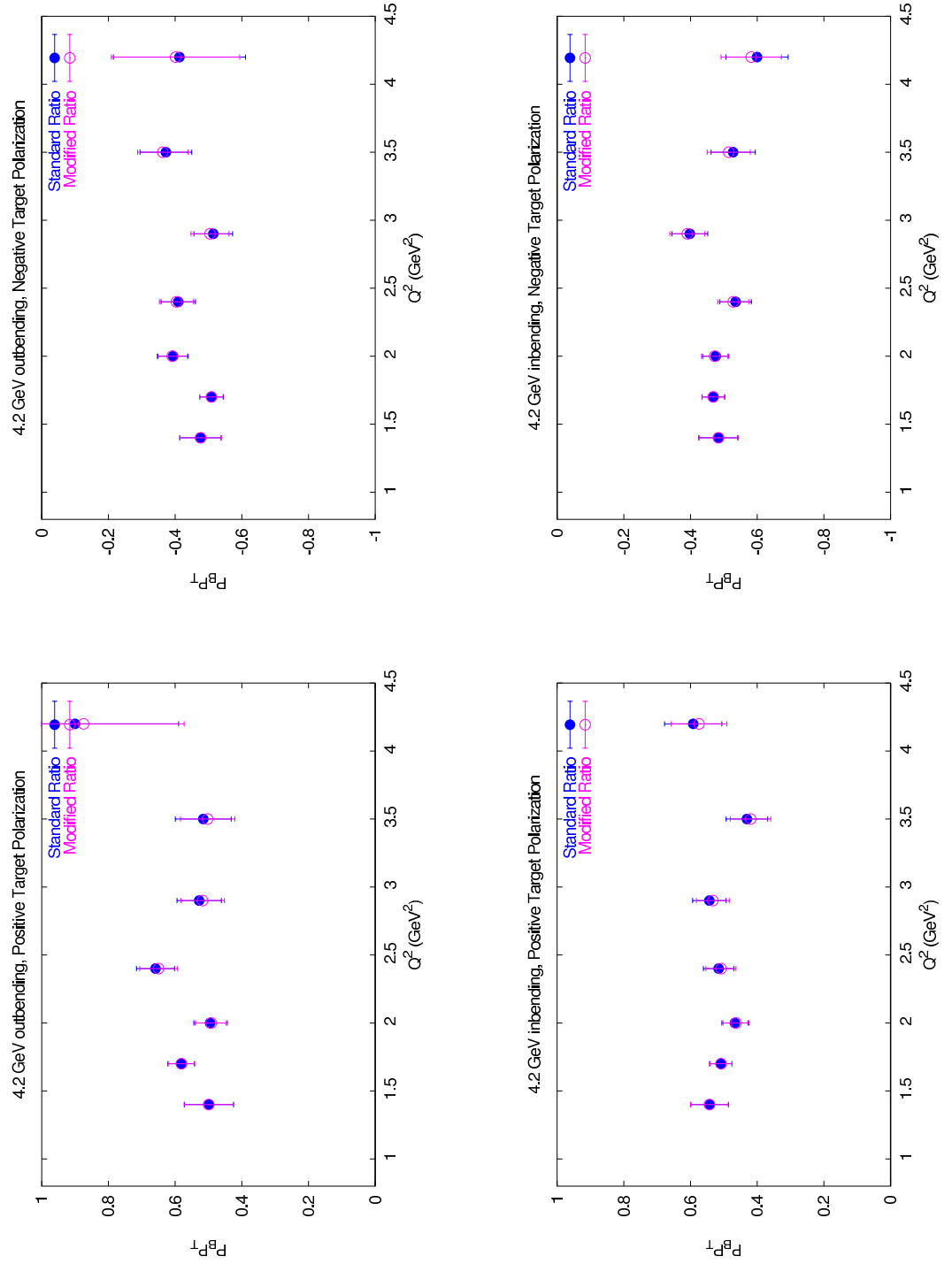
Figure 5.18: $P_B P_T$ for the 4.2 GeV energy data, comparing the results using the standard formula for r to the results using a fixed value of r.

the events used to determine $P_B P_T$. The first test done was to vary the cut values for all of the kinematic variables other than the polar angle difference between the electron and proton. The new values used can be shown in comparison to the old values.

Table 5.1: Modified Proton Cuts.

Kinematic Variable	Standard Cut	Modified Cut
$W(GeV)$	$0.85 < W < 1.035$	$0.765 < W < 1.138$
$E_{proton}(GeV)$	$\lvert E_p - E_{exp} \rvert < 0.15$	$\lvert E_p - E_{exp} \rvert < 0.181$
$\theta_p(Degrees)$	$\lvert \theta_p - \theta_e \rvert < 2.5°$	$\lvert \theta_p - \theta_e \rvert < 2.75°$

The $P_B P_T$ values obtained using these new cuts are shown in comparison to the standard cuts in Fig. 5.19, again for each Q^2 bin. The effect is again small, the difference in the averages being about 5%, relative, roughly the size of the statistical error.

The co-planarity cut can also be changed, which, since this is the variable in which the background subtraction is performed, amounts to a re-calculation of the background effects as well. The standard cut and normalization region used is shown in Table 5.2

Table 5.2: Modified Co-planarity.

	Standard Range	Modified Range
$ExclusiveRegion$	$178° < \phi_p - \phi_e < 182°$	$177° < \phi_p - \phi_e < 183°$
$LowNormalizationRegion$	$175° < \phi_p - \phi_e < 177°$	$173° < \phi_p - \phi_e < 176°$
$HighNormalizationRegion$	$183° < \phi_p - \phi_e < 185°$	$184° < \phi_p - \phi_e < 187°$

The results for $P_B P_T$ for both sets of co-planarity cuts are shown, for each Q^2 point, in Fig. 5.20. The difference between the averages is also about 5%.
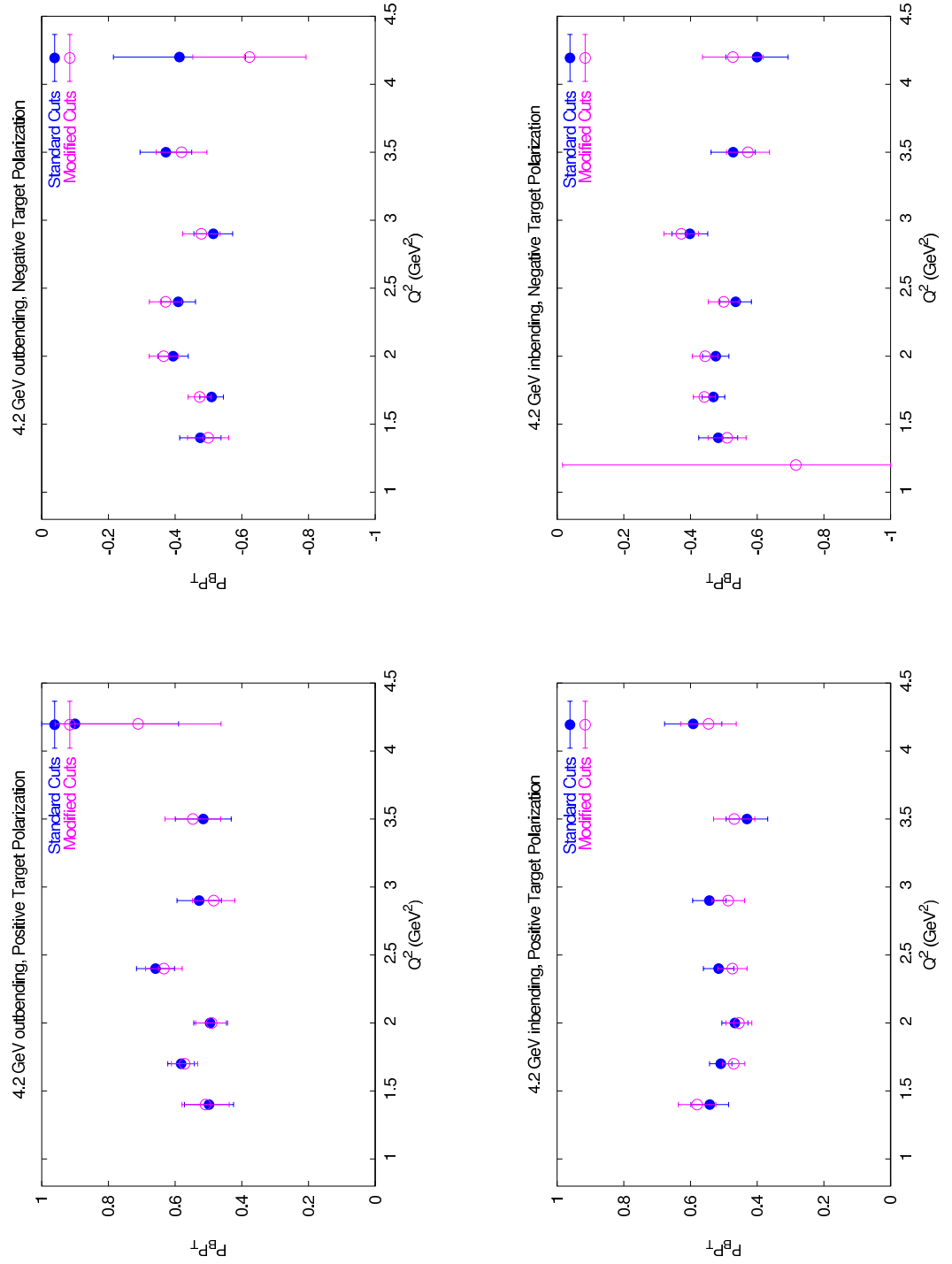
Figure 5.19: $P_B P_T$ for the 4.2 GeV energy data, comparing the results from the standard kinematic cuts to the results using the modified cuts.
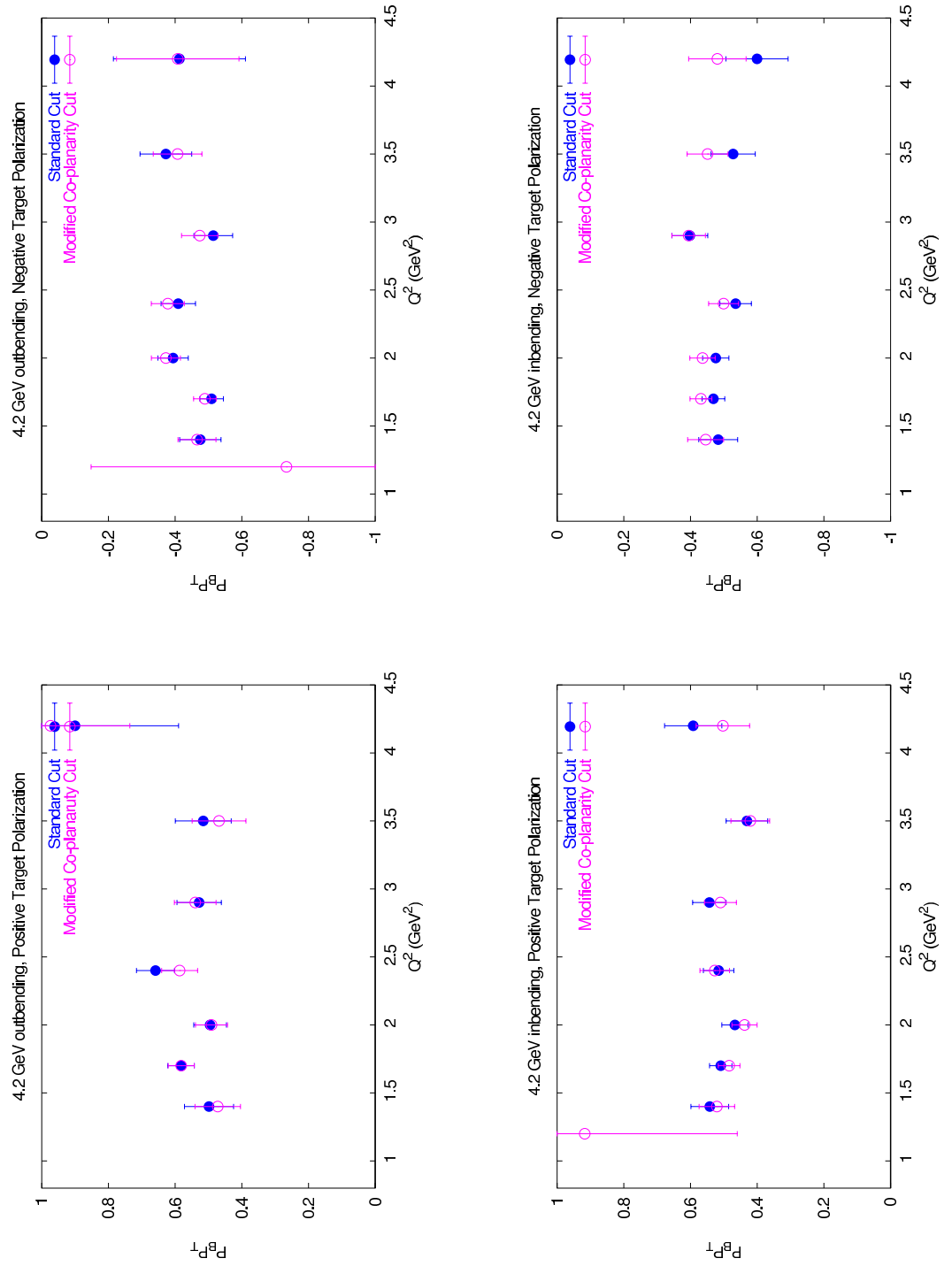
Figure 5.20: $P_B P_T$ for the 4.2 GeV energy data, comparing the results from the standard co-planarity cuts to the results using the modified co-planarity cuts.
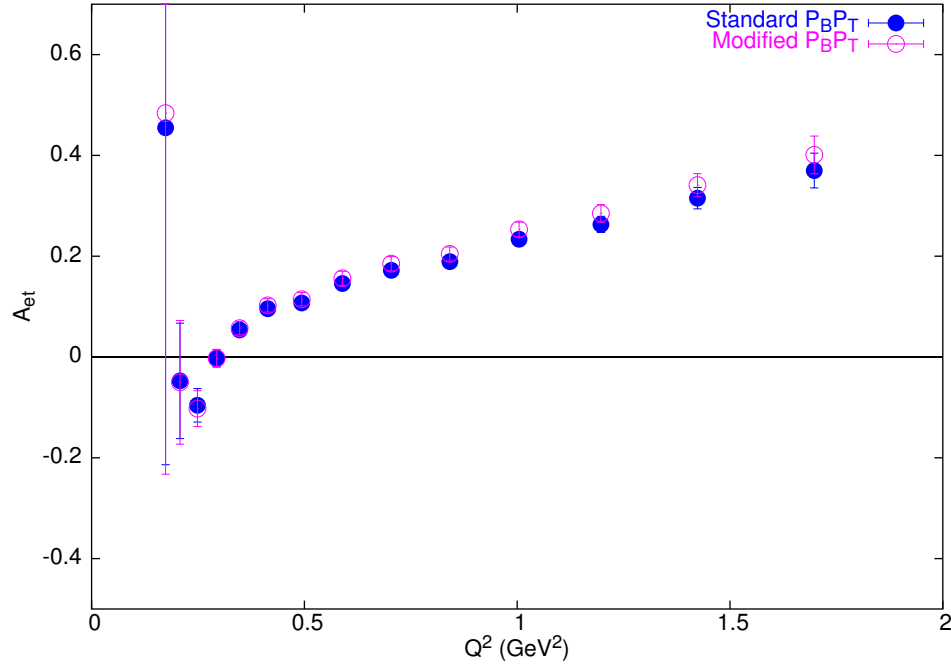
Figure 5.21: A_{et} using the standard values of $P_B P_T$, compared to A_{et} using a value of $P_B P_T$ shifted by one standard deviation.

An overall error budget for the $P_B P_T$ measurements is shown in Table 5.3. The systematic errors are treated as independent, and added in quadrature, and then the resulting overall systematic is added in quadrature to the statistical error.

The effect of $P_B P_T$ on the analysis was done by shifting values by the error associated with them, and then re-analyzing the asymmetry, much as in the other error evaluations. The largest effect on the asymmetry occurs when both the positive and negative target polarization values are moved in the same direction. This has the effect of changing the overall normalization of the asymmetry, without causing much change to the polarization ratios. To test the size of the effect, the positive target $P_B P_T$ was decreased by one standard deviation, as was the negative target $P_B P_T$. The asymmetry was then recalculated, and a comparison to the asymmetry using the standard values of $P_B P_T$ as shown in Fig. 5.21.

5.4.5   The Polarization of ^{15}N

In this analysis, it was assumed that the ^{15}N nucleus in ^{15}NH$_3$ contributes to exclusive π^+ electro-production only as an unpolarized background. This is not true, the ^{15}N nucleus is a spin 1/2 object which polarizes similarly to the protons from the Hydrogen. The spin of the ^{15}N is carried by a single unpaired proton. The size of the effect on the asymmetry is very small, and can be estimated by determining the polarization of this proton, and treating it as a modification of $P_B P_T$.

The polarization of the ^{15}N can be estimated using Equal Spin Temperature theory as described in Section 3.2.2. The temperature of the proton Zeeman system and the ^{15}N Zeeman system are the same, since both are in thermal contact with the electron spin-spin system. This means that for any given proton polarization, the ^{15}N polarization depends only on the magnetic field and the magnetic moments of the proton and ^{15}N. The magnetic moment of the proton is equal to $2.793\mu_N$ while the magnetic moment of ^{15}N is $-0.282\mu_N$. A proton polarization of 70% corresponds to a ^{15}N polarization of -8.7%, as determined from Eq. 5.1.

$$T_S = \frac{\mu_{prot}B}{k\tanh^{-1}P_{prot}}, \ P_{^{15}N} = \tanh\frac{\mu_{^{15}N}B}{kT_S} \tag{5.1}$$

The polarization of the proton in the ^{15}N can be determined using Clebsch-Gordon coefficients, given that the proton is in the p-state [46]. The polarization of the proton in ^{15}N is of the opposite sign, and one third the magnitude of the ^{15}N polarization, $P_{prot_{N15}}$ =2.9%.

There is only one ^{15}N atom per every three Hydrogen atoms, so the expected effect of the polarized proton from ^{15}N is further reduced by a factor of 3. The result is an estimate for the maximum contribution of the polarized ^{15}N of $\sim$1% (absolute). This will be further reduced by the fact that the Fermi motion of the proton in the

^{15}N will cause some events to fall outside the neutron missing mass cut, and perhaps extend even into the region used to normalize the ^{12}C counts to the ^{15}N counts. The exact reduction of the effect due to the Fermi motion is difficult to determine, but whatever the reduction, it is sufficient to allow the ^{15}N polarization to be neglected for this analysis.

5.4.6 Radiative Corrections

It is possible for the electron to radiate a low energy photon, before or soon after the scattering takes place. This results in an measurement of the electron energy that is different from the energy that the electron had during the scattering. For cross section measurements, these effects are very important, as some of the cross section strength from higher energies will be shifted down into the lower energies. In the case of asymmetries, the effect is greatly reduced due to cancellations in the ratio. More specifically, in the case of this analysis, radiative effects are expected to be very small, since the tight missing mass cut restricts the allowed phase space for radiated photons. A calculation of the radiative effects is still under way, but an estimate of the size can be gained from the eg1a π^+ electro-production analysis [47], which calculated the correction to be a few percent. For the time being, this estimate will be treated as a systematic error on the asymmetry.

5.4.7 Pion Decay

The mean lifetime of a pion in its center of mass frame is 26 ns. In the lab frame, this results in a reasonable probability of the pion to decay. By far the most likely decay path is $\pi^+ \rightarrow \mu^+ \nu_\mu$ with a branching ratio greater than 99.9%. In principle, the μ^+ can still be detected, and in fact could easily be mis-identified as a π^+. In

this case, there would be a kinematic shift, since the decay into a μ^+ would alter the reconstructed track of the particle and result in an incorrect determination of the momentum. This effect can be estimated by comparing the asymmetry for events which had a high probability of decay to events which had a low probability of decay. The probability of a pion not decaying is determined through Eq. 5.2 for each event in the analysis, where τ is the mean lifetime of the pion in the center of mass frame. The distribution of this probability is shown in Fig. 5.22. The region that had a survival probability less than 95% was analyzed separately from the region which had a survival probability greater than 95%. The asymmetry for each case can then be compared, as shown in Fig. 5.23.

$$P_{surv} = e^{-t/\tau\gamma} \tag{5.2}$$

It would appear to the eye that there is a large difference between the two data sets. This is misleading however. In fact, the two sets have very different kinematic regions. In the independent, four-dimensional analysis of the asymmetry, there are very few bins where the data overlaps. In those few bins where there is overlap, the agreement is actually very good, with a an average difference is $0.0168 + / - 0.0309$ and a χ_ν^2 of 0.659.

5.4.8 Overall Systematic Error Estimate

All of the previously mentioned errors are treated as independent systematics. In every case, the analysis was varied, and a comparison was made between two independent data sets, highlighting a specific effect, such as the case for pion decay or the event selection cuts, or comparing a non-standard analysis to the standard one, such as in the dilution and $P_B P_T$ in each case, the weighted average of the difference
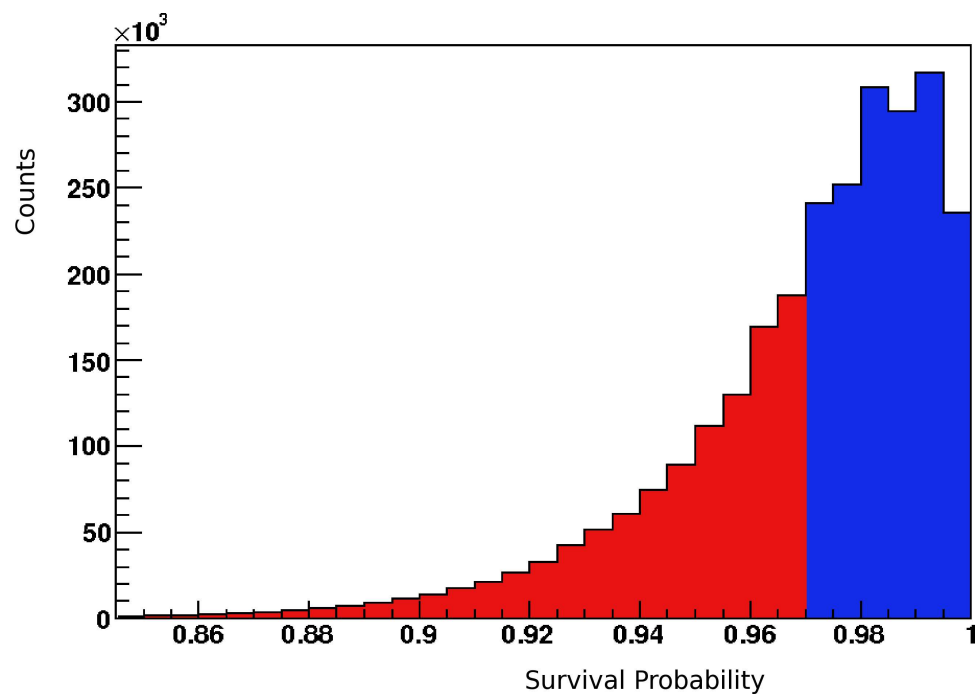
Figure 5.22: The probability that the pion does not decay during its flight. The red region and blue region represent separate samples that can be analyzed to determine the effect of pion decay on the asymmetry.
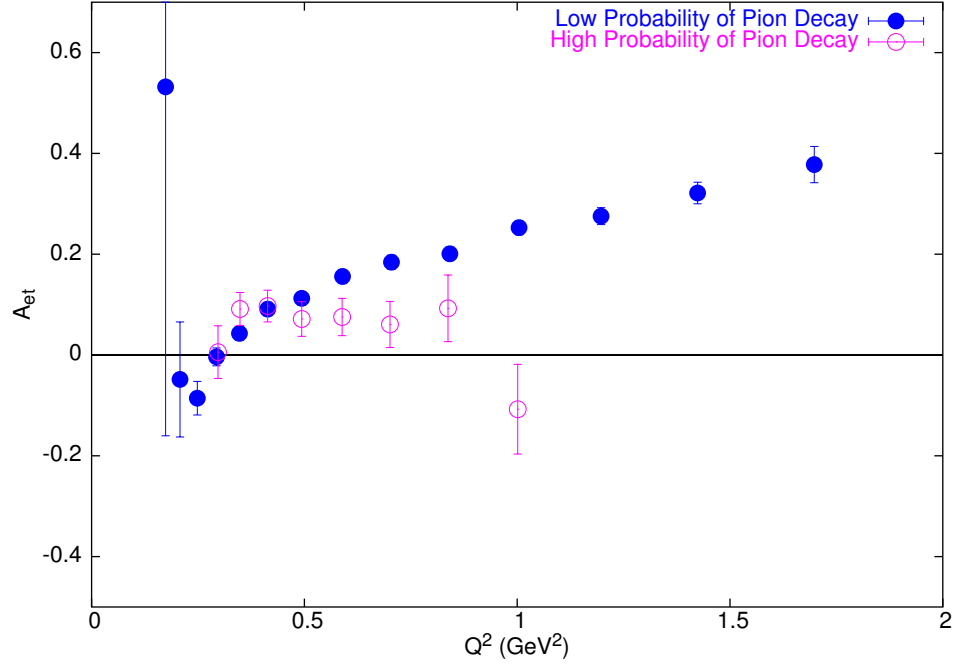
Figure 5.23: Comparison of A_{et} for the events where the pion had a very low probability of decay ($P_{surv} > 95\%$), and events where the pion had a higher probability of decay ($P_{surv} < 95\%$).

between the two asymmetry measurements (in the bins they share in common) is used as an estimate of the systematic error.

Each of these values is added in quadrature to determine the overall systematic error associated with the asymmetry, the result being shown in Table 5.4.

Table 5.3: $P_B P_T$ Error.

4.2 GeV in-bending, $P_T > 0$	
Systematics	
Analyzing power (from r)	0.98%
Kinematic cuts	4.4%
Co-planarity cuts	4.6%
Sub-total	6.47%
Statistical	3.53%
TOTAL	7.36%
4.2 GeV in-bending, $P_T < 0$	
Systematics	
Analyzing power (from r)	0.98%
Kinematic cuts	4.35%
Co-planarity cuts	8.08%
Sub-total	9.23%
Statistical	3.81%
TOTAL	9.98%
4.2 GeV out-bending, $P_T > 0$	
Systematics	
Analyzing power (from r)	0.83%
Kinematic cuts	1.90%
Co-planarity cuts	2.79%
Sub-total	3.48%
Statistical	4.10%
TOTAL	5.37%
4.2 GeV out-bending, $P_T < 0$	
Systematics	
Analyzing power (from r)	0.88%
Kinematic cuts	4.65%
Co-planarity cuts	4.31%
Sub-total	6.39%
Statistical	4.45%
TOTAL	7.79%

Table 5.4: Systematic Error on A_{et}.

Systematic	Average Value
Dilution	0.001 (value changes only with $\cos\theta^*$)
Acceptance (from torus comparison)	0.024
Acceptance (from sector comparison)	0.036
Acceptance (from re-binning)	0.016
Event Selection	0.009
$P_B P_T$	0.036 ($\approx 8\%$)
Radiative Effects	~ 0.03
pion decay	0.017
TOTAL	0.068

Chapter 6

Conclusion and Outlook

The data obtained during the eg1b experiment has been used to determine the double spin asymmetry, A_{et}, and the single spin asymmetries, A_e and A_t, for exclusive π^+ electro-production. The asymmetry has been directly compared to the MAID2003 model. There seems to be reasonable agreement between the data and the values obtained from MAID, with some deviation that appears at first inspection to be significant. The level of agreement implies that the results of this analysis are consistent with those from other experiments, both direct measurements of the asymmetries and other measurements which are used to determine the multi-pole terms of the resonances. The deviations, especially in the case of the double spin asymmetry, represent places where MAID, or perhaps other models, can be improved by incorporating the results of this analysis into the fit. Improvement in the current models of the resonances translates into an improvement of the understanding of the strong force.

The analysis of the other energy settings will increase the kinematic coverage, as well as the statistics of the measurement. A large table of all of the asymmetry values for all of the energy settings will be invaluable for those making models for

pion production.

Improved knowledge of the response functions corresponds directly to an increased understanding of the spin structure of the resonances. Other channels from the eg1b experiment are also being analyzed by other collaboration members, notably exclusive π^- electro-production from the neutron. This data was taken with the polarized ND_3 target, and acts as a compliment to the data presented in this thesis and can be analyzed in the same way. It can add to the knowledge of the neutron resonances just as the π^+ results will help with the understanding of the proton resonances.

In 2005, a new experiment [48] was conducted in Hall B at Jefferson Lab, using much of the same equipment (with a modified Čerenkov detecor in one sector of CLAS allowing for a much improved detection of scattered electrons at very small polar angles), including the polarized target. An analysis of the double spin asymmetry for exclusive π^+ production using data from this experiment would increase both the overall statistic and the kinematic coverage of the measurement, especially in the low Q^2 region. After a scheduled upgrade of the CEBAF accelerator, another experiment [49] has been approved to run with a polarized target and polarized electron beam. Data from this experiment would greatly extend the kinematic range for which the asymmetry could be calculated.

The results for double spin asymmetry in exclusive π^+ electro-production from the eg1b experiment will be useful in improving the understanding of the spin structure of the resonances, understanding which will be further improved with the increased statistics and kinematic range that come from recent experiments and experiments yet to come.

Appendix A

Response Functions, CGLN Amplitudes, and Helicity Amplitudes

A.1 Response Functions in terms of CGLN amplitudes

$$R_T = |F_1|^2 + |F_2|^2 + \frac{\sin^2\theta^*}{2}(|F_3|^2 + |F_2|^2)$$

$$R_T^y = Im[\sin\theta^*(F_1^*F_3 - F_2^*F_4 + \cos\theta^*(F_1^*F_4 - F_2^*F_3) - \sin^2\theta^*F_3^*F_4)]$$

$$R_L = Re[|F_5|^2 + |F_6|^2 + 2\cos\theta^*F_5^*F_6]$$

$$R_L^y = -2\sin\theta^*Im[F_5^*F_6]$$

$$R_{LT} = \sin\theta^*Re[F_2^*F_5 - F_3^*F_5 - F_1^*F_6 - F_4^*F_6 - \cos\theta^*(F_4^*F_5 + F_3^*F_6)]$$

$$R_{LT}^x = Im[-F_1^*F_5 + F_2^*F_6 + \cos\theta^*(F_2^*F_5 - F_1^*F_6)]$$

$$R_{LT}^y = Im[-F_1^*F_5 + F_2^*F_6 + \cos\theta^*(F_2^*F_5 - F_1^*F_6) + \sin^2\theta^*(F_3^*F_6 - F_4^*F_5)]$$

$$R_{LT}^Z = \sin\theta^* Im[F_2^* F_5 + F_1^* F_6]$$

$$R_{TT} = \frac{1}{2}\sin^2\theta^*(|F_3|^2 + |F_4|^2) + \sin^2\theta^* Re[F_2^* F_3 + F_1^* F_4 + \cos\theta^* F_3^* F_4]$$

$$R_{TT}^x = \sin\theta^* Im[2F_1^* F_2 + F_1^* F_3 - F_2^* F_4 + \cos\theta^*(F_1^* F_4 - F_2^* F_3)]$$

$$R_{TT}^y = -Im[\sin\theta^*(-2F_1^* F_2 - F_1^* F_3 + F_2^* F_4 + \cos\theta^*(F_2^* F_3 - F_1^* F_4) + \sin^2\theta^* F_3^* F_4)]$$

$$R_{TT}^z = -\sin^2\theta^* Im[F_2^* F_3 + F_1^* F_4] \tag{A.1}$$

$$R_{LT'} = -\sin\theta^* Im[F_2^* F_5 + F_3^* F_5 + F_1^* F_6 + F_4^* F_6 + \cos\theta^*(F_4^* F_5 + F_3^* F_6)]$$

$$R_{LT'}^x = Re[-F_1^* F_5 + F_2^* F_6 + \cos\theta^*(F_2^* F_5 - F_1^* F_6)]$$

$$R_{LT'}^y = Re[F_1^* F_5 - F_2^* F_6 + \cos\theta^*(F_1^* F_6 - F_2^* F_5) + \sin^2\theta^*(F_4^* F_5 - F_3^* F_6)]$$

$$R_{LT'}^z = \sin\theta^* Re[F_2^* F_5 + F_1^* F_6]$$

$$R_{TT'}^x = \sin\theta^* Re[F_1^* F_3 - F_2^* F_4 + \cos\theta^*(-F_2^* F_3 + F_1^* F_4)]$$

$$R_{TT'}^z = -|F_1|^2 - |F_2|^2 + Re[2\cos\theta^* F_1^* F_2 - \sin^2\theta^*(F_2^* F_3 + F_1^* F_4)]$$

A.2   Response functions and helicity amplitudes

$$R_T = \frac{1}{2}(|H_1|^2 + |H_2|^2 + |H_3|^2 + |H_4|^2)$$

$$R_T^y = -Im[H_1^* H_2 + H_3^* H_4]$$

$$R_L = |H_5|^2 + |H_6|^2$$

$$R_L^y = -2Im[H_5^* H_6]$$

$$R_{LT} = \frac{1}{\sqrt{2}}Re[H_5^* H_1 - H_5^* H_4 + H_6^* H_2 + H_6^* H_3]$$

$$R_{LT}^x = \frac{1}{\sqrt{2}}Im[-H_5^* H_2 + H_5^* H_3 - H_6^* H_1 + H_6^* H_4]$$

$$R_{LT}^y = \frac{1}{\sqrt{2}}Im[-H_5^* H_2 - H_5^* H_3 + H_6^* H_1 - H_6^* H_4]$$

$$R_{LT}^z = \frac{1}{\sqrt{2}}Im[-H_5^* H_1 - H_5^* H_4 + H_6^* H_2 - H_6^* H_3]$$

$$R_{TT} = Re[-H_1^* H_4 + H_2^* H_3] \qquad (A.2)$$

$$R_{TT}^x = Im[H_1^* H_3 - H_2^* H_4]$$

$$R_{TT}^y = -Im[H_1^* H_3 + H_2^* H_4]$$

$$R_{TT}^z = -Im[H_1^* H_4 + H_2^* H_3]$$

$$R_{LT'} = \frac{1}{\sqrt{2}} Im[-H_5^* H_1 + H_5^* H_4 - H_6^* H_2 - H_6^* H_3]$$

$$R_{LT'}^x = \frac{1}{\sqrt{2}} Re[H_5^* H_2 - H_5^* H_3 + H_6^* H_1 + H_6^* H_4]$$

$$R_{LT'}^y = \frac{1}{\sqrt{2}} Re[-H_5^* H_2 - H_5^* H_3 + H_6^* H_1 - H_6^* H_4]$$

$$R_{LT'}^z = \frac{1}{\sqrt{2}} Re[H_5^* H_1 + H_5^* H_4 - H_6^* H_2 + H_6^* H_3]$$

$$R_{TT'}^x = Re[H_1^* H_2 + H_3^* H_4]$$

$$R_{TT'}^z = \frac{1}{2}(|H_1|^2 - |H_2|^2 + |H_3|^2 - |H_4|^2)$$

Appendix B

Asymmetry Plots
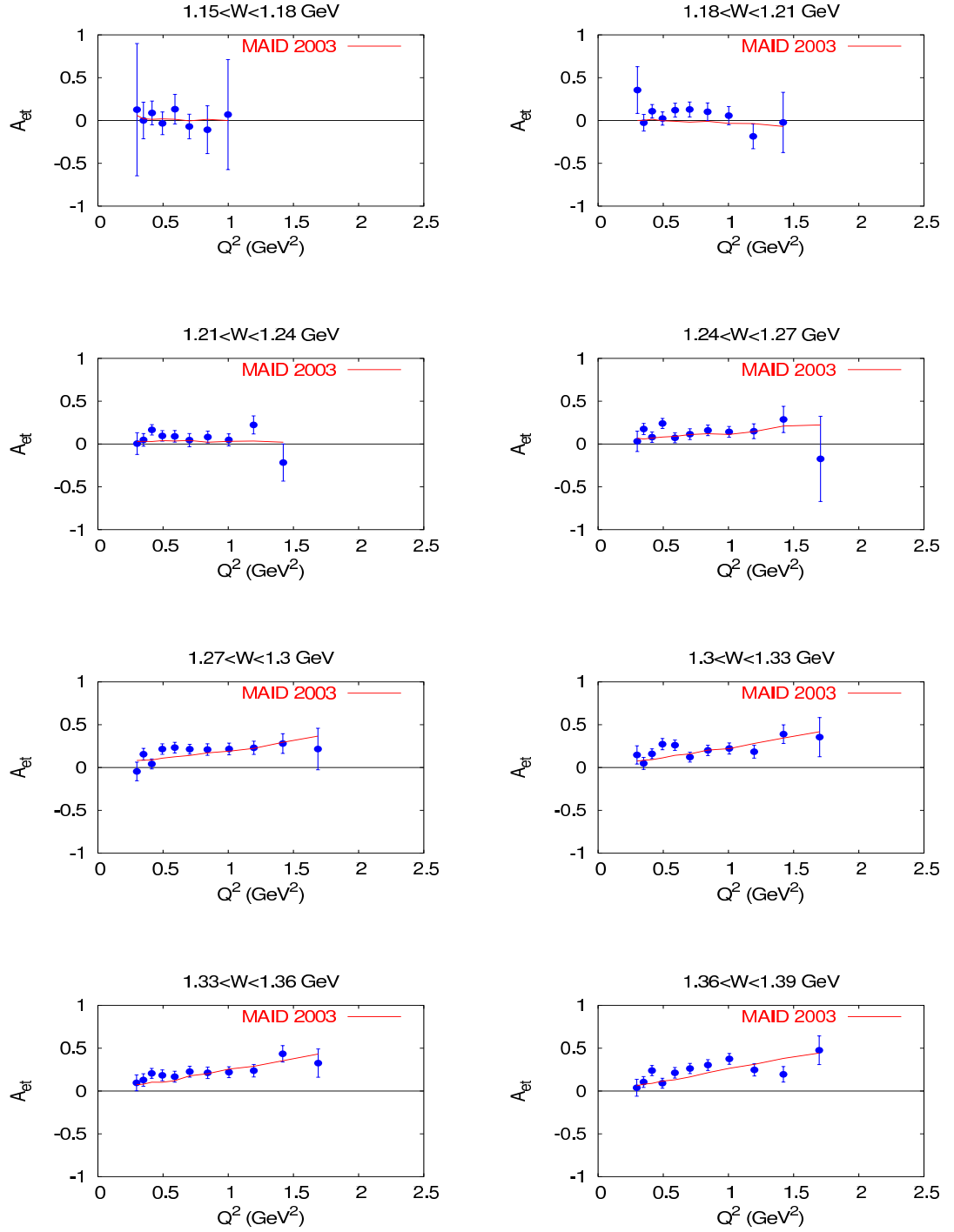
Figure B.1: A_{et} as a function of Q^2 for each W bin from 1.15 GeV to 1.39 GeV. The asymmetry has been averaged over $\cos\theta^*$ and ϕ^*.
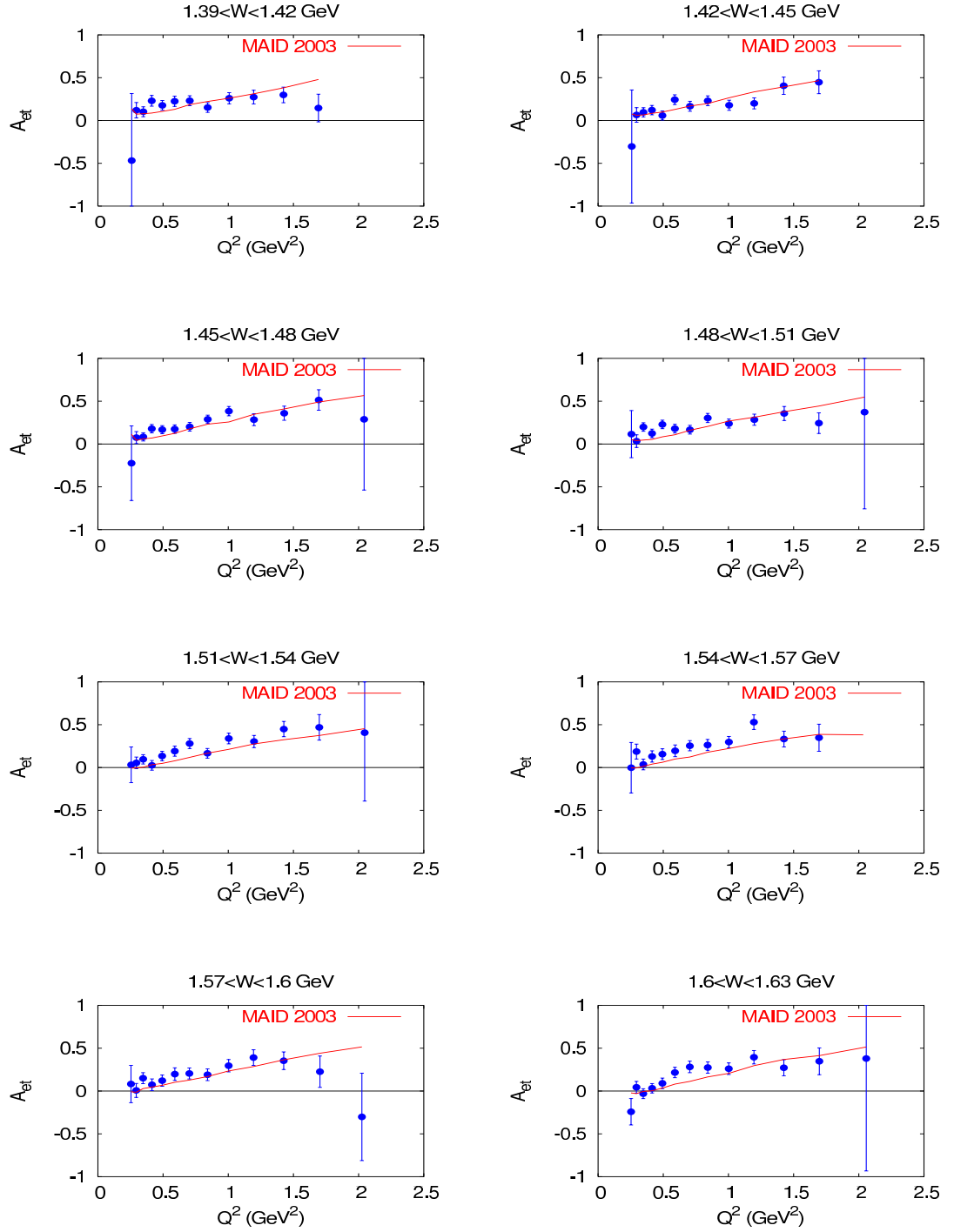
Figure B.2: A_{et} as a function of Q^2 for each W bin from 1.39 GeV to 1.63 GeV. The asymmetry has been averaged over $\cos\theta^*$ and ϕ^*.
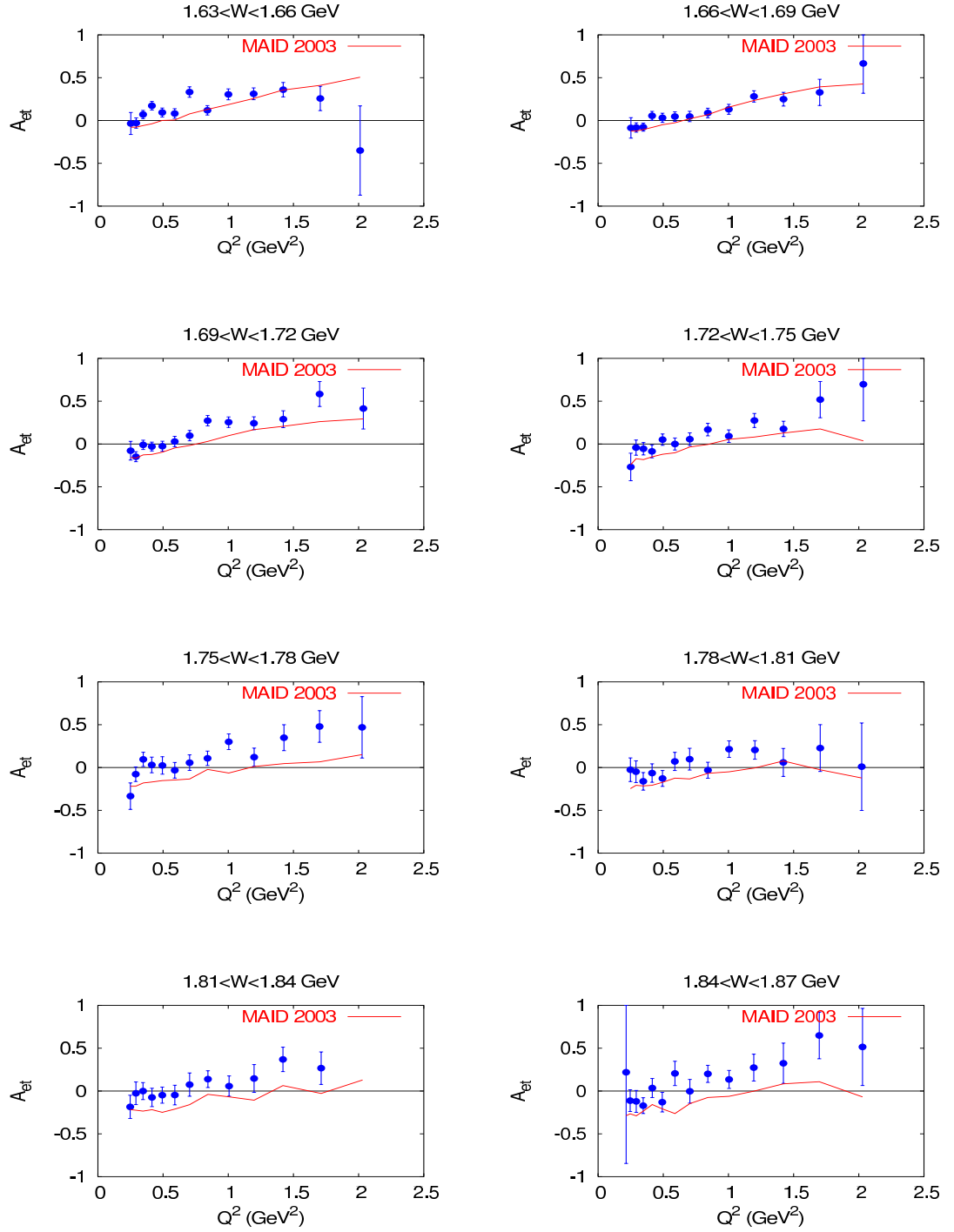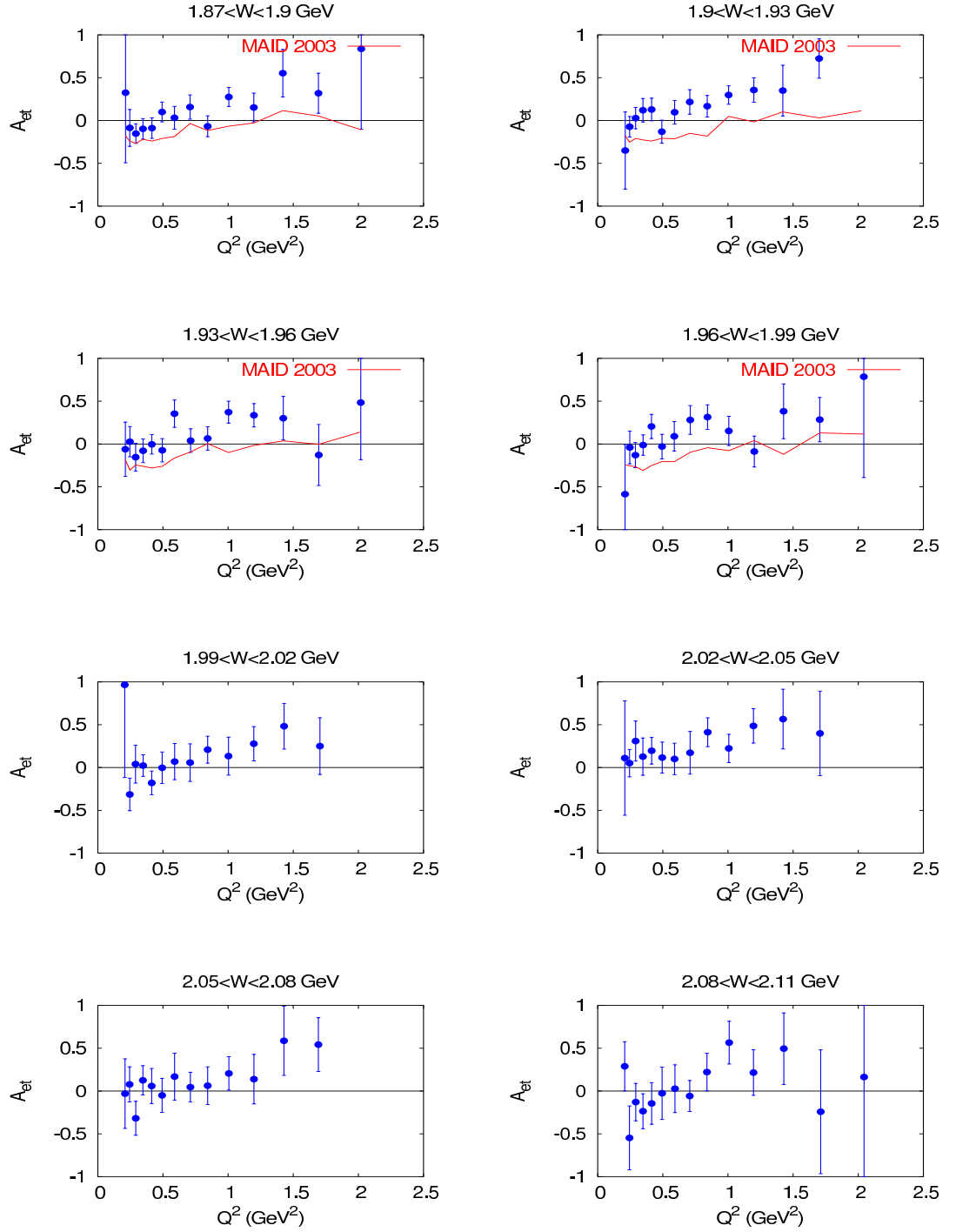
Figure B.3: A_{et} as a function of Q^2 for each W bin from 1.63 GeV to 1.87 GeV. The asymmetry has been averaged over $\cos\theta^*$ and ϕ^*.

Figure B.4: A_{et} as a function of Q^2 for each W bin from 1.87 GeV to 2.11 GeV. The asymmetry has been averaged over $\cos\theta^*$ and ϕ^*.
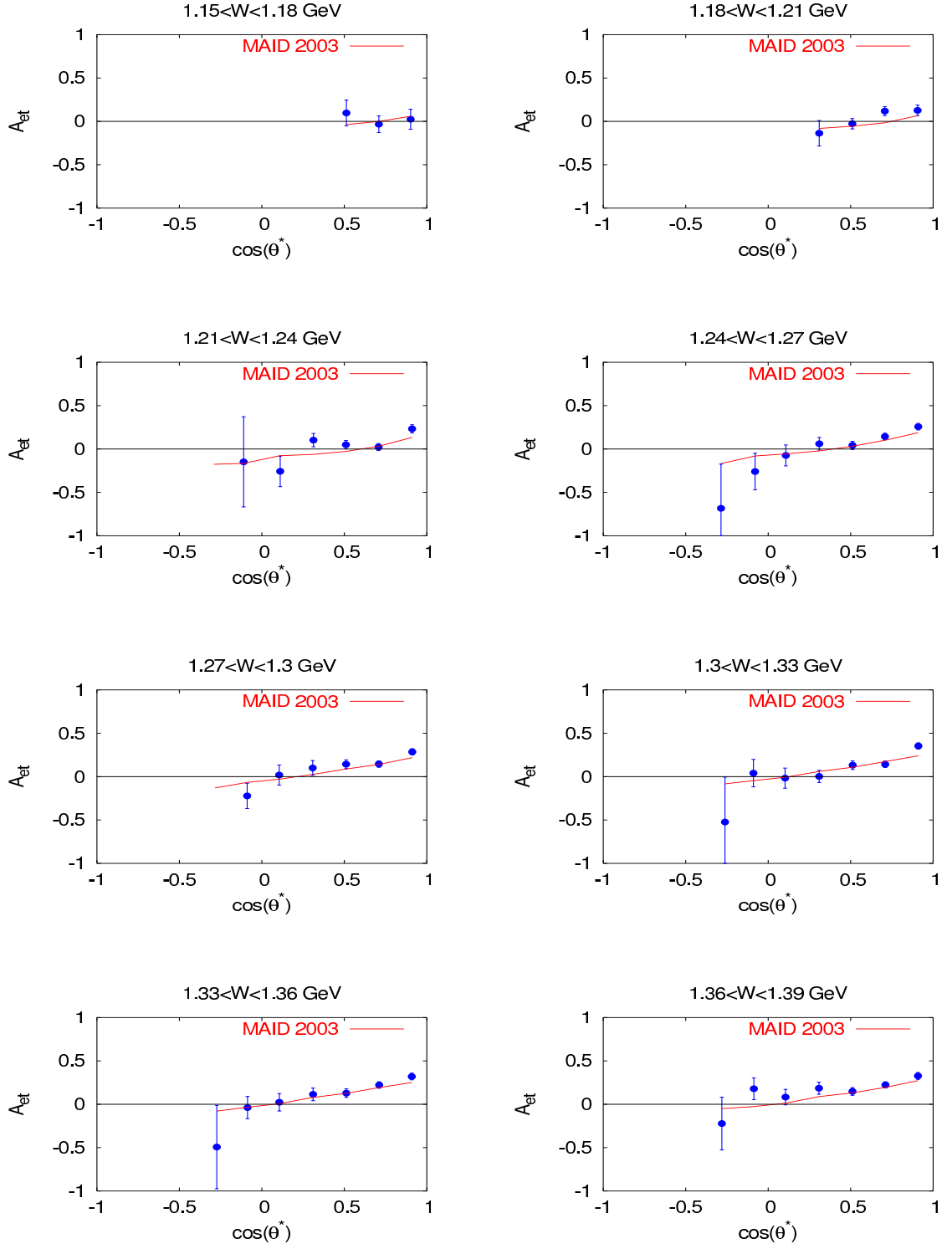
Figure B.5: A_{et} as a function of $\cos\theta^*$ for each W bin from 1.15 GeV to 1.39 GeV. The asymmetry has been averaged over Q^2 and ϕ^*.
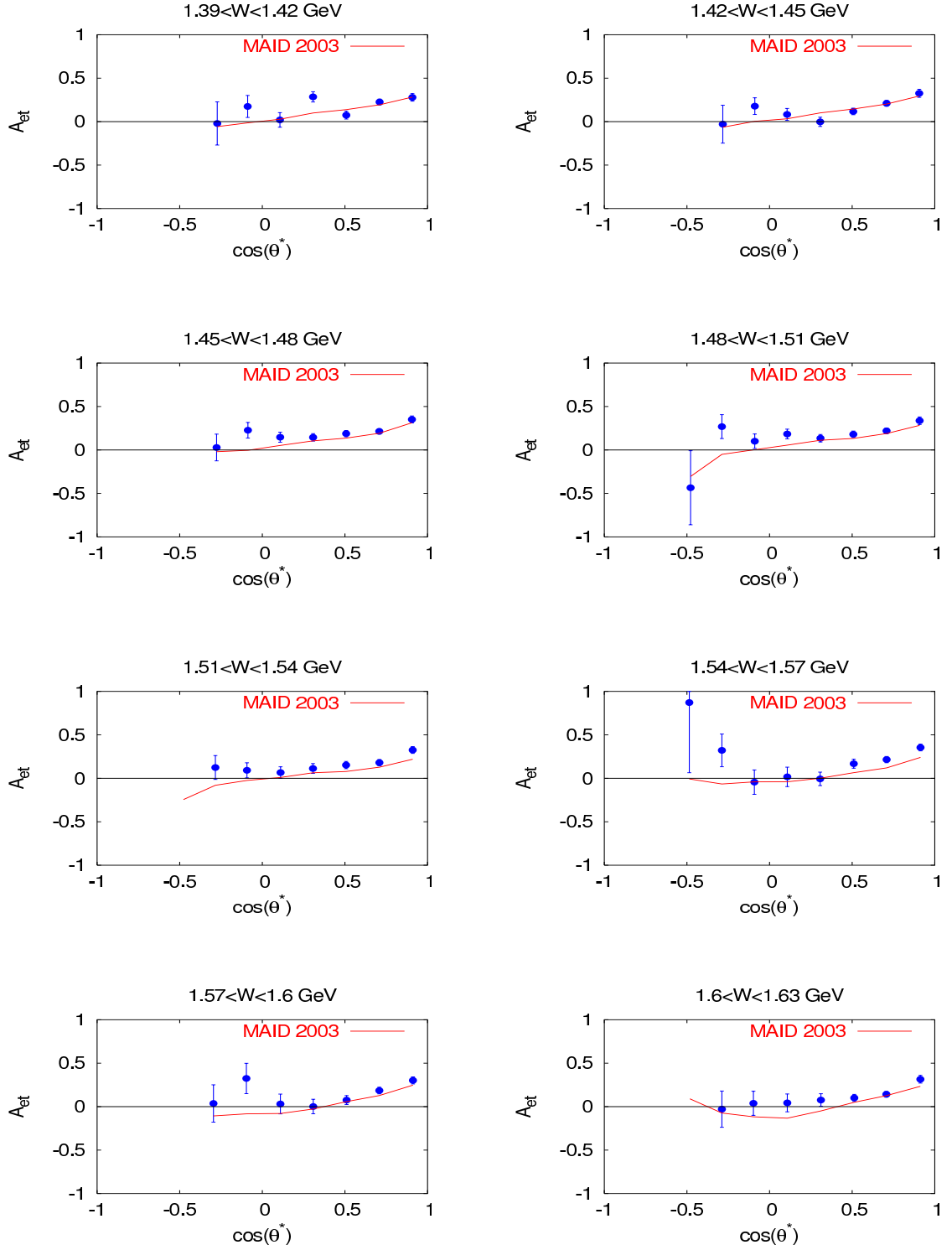
Figure B.6: A_{et} as a function of $\cos\theta^*$ for each W bin from 1.39 GeV to 1.63 GeV. The asymmetry has been averaged over Q^2 and ϕ^*.
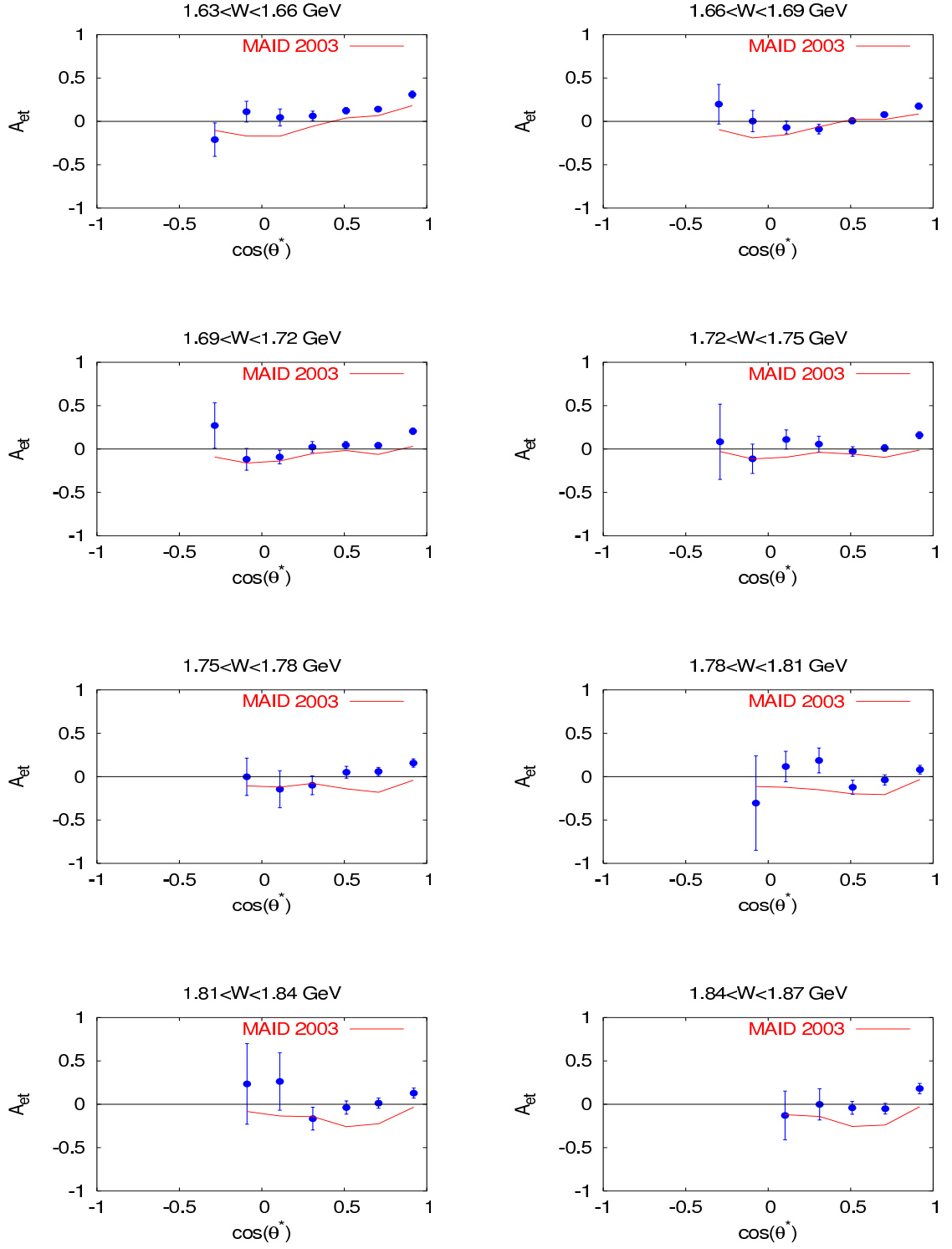
Figure B.7: A_{et} as a function of $\cos \theta^*$ for each W bin from 1.63 GeV to 1.87 GeV. The asymmetry has been averaged over Q^2 and ϕ^*.
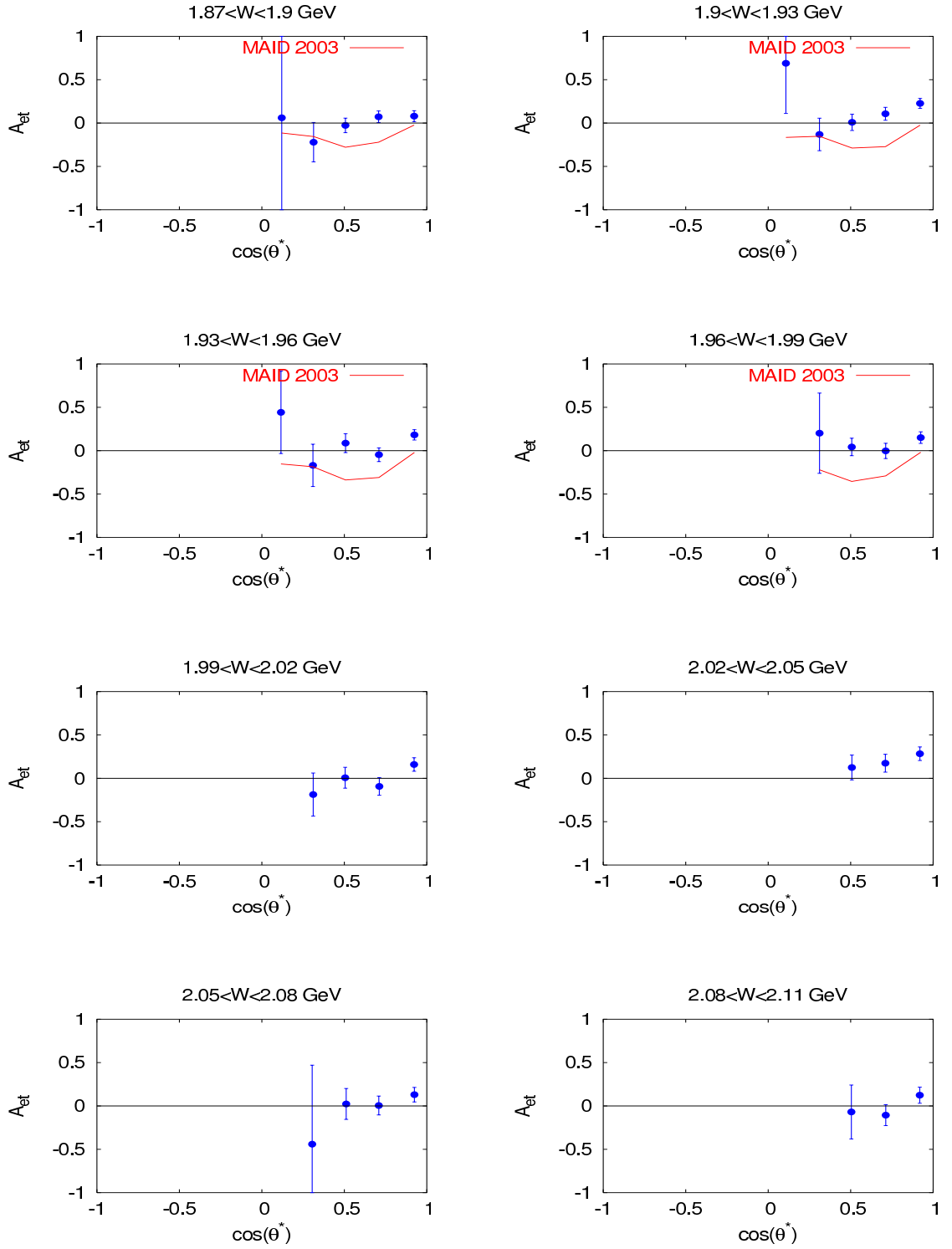
Figure B.8: A_{et} as a function of $\cos\theta^*$ for each W bin from 1.87 GeV to 2.11 GeV. The asymmetry has been averaged over Q^2 and ϕ^*.
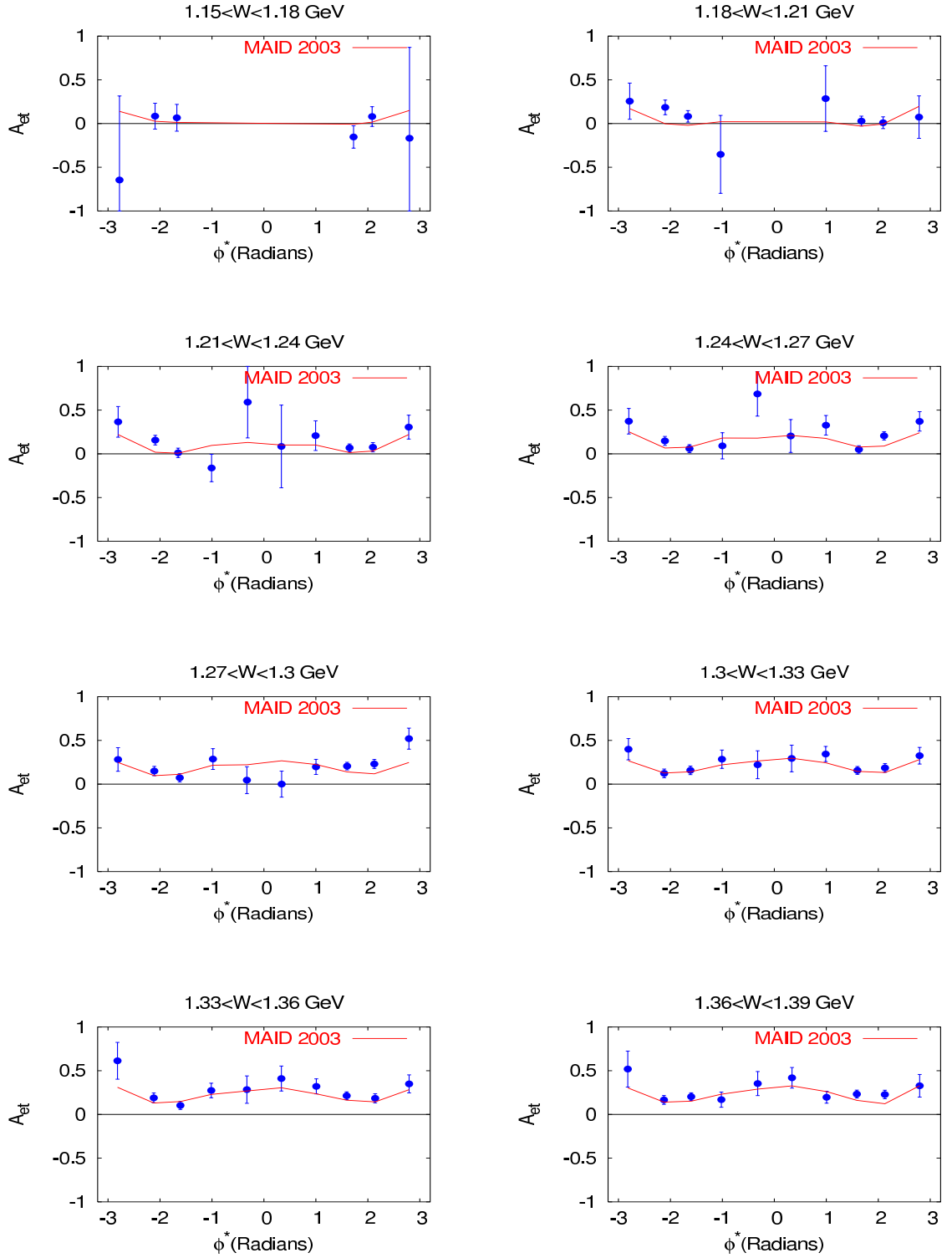
Figure B.9: A_{et} as a function of ϕ^* for each W bin from 1.15 GeV to 1.39 GeV. The asymmetry has been averaged over Q^2 and $\cos\theta^*$.

Figure B.10: A_{et} as a function of ϕ^* for each W bin from 1.39 GeV to 1.63 GeV. The asymmetry has been averaged over Q^2 and $\cos\theta^*$.
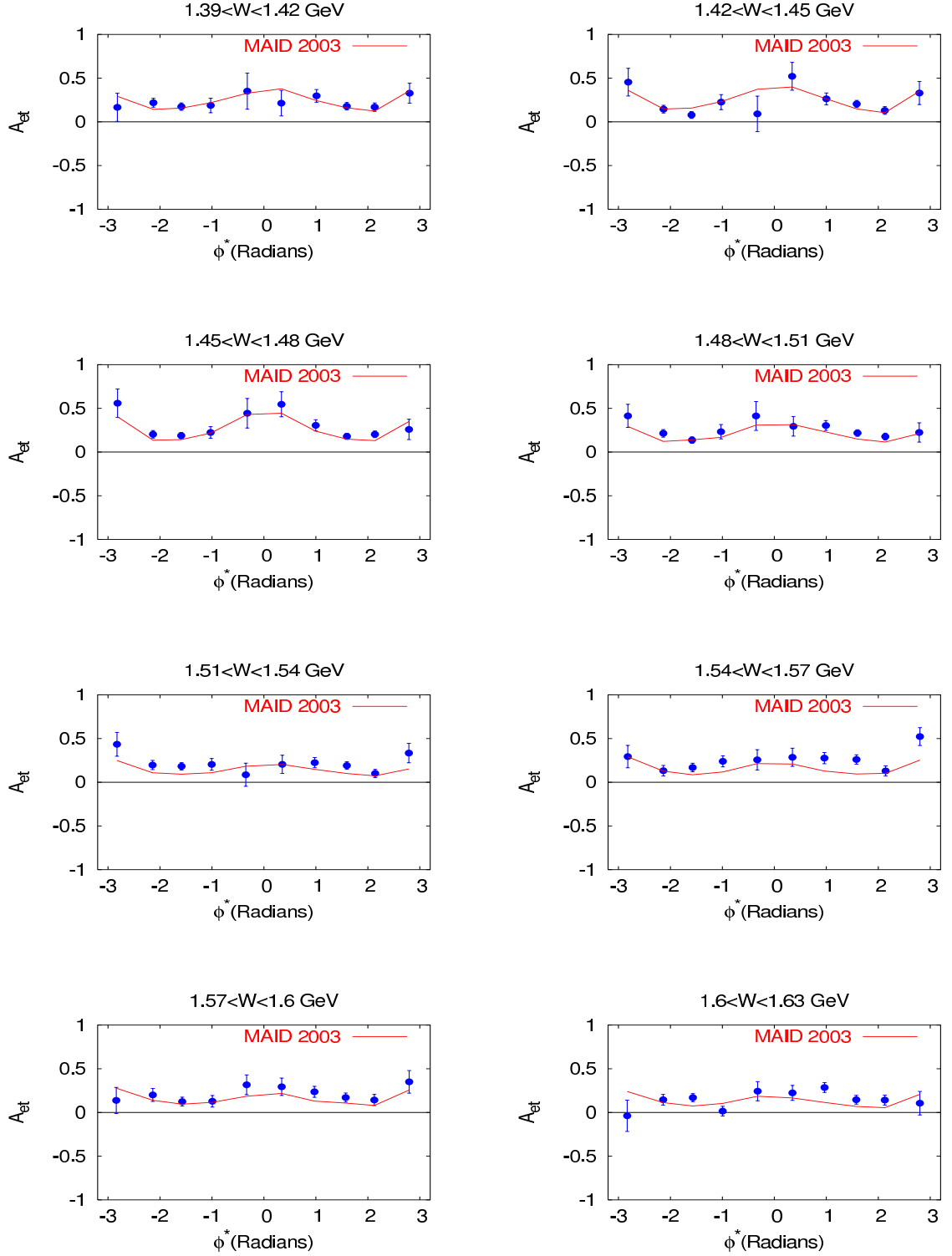
Figure B.11: A_{et} as a function of ϕ^* for each W bin from 1.63 GeV to 1.87 GeV. The asymmetry has been averaged over Q^2 and $\cos\theta^*$.
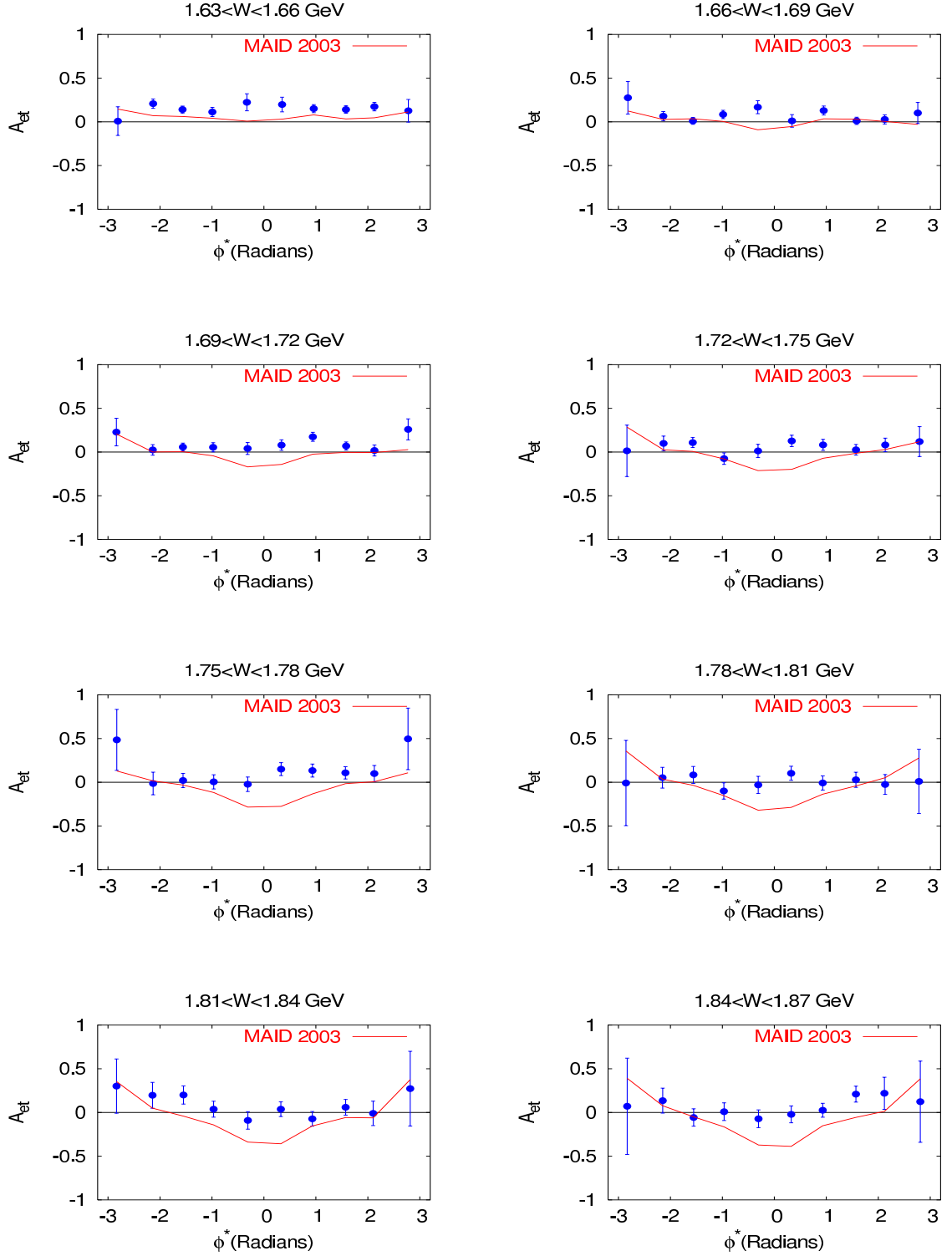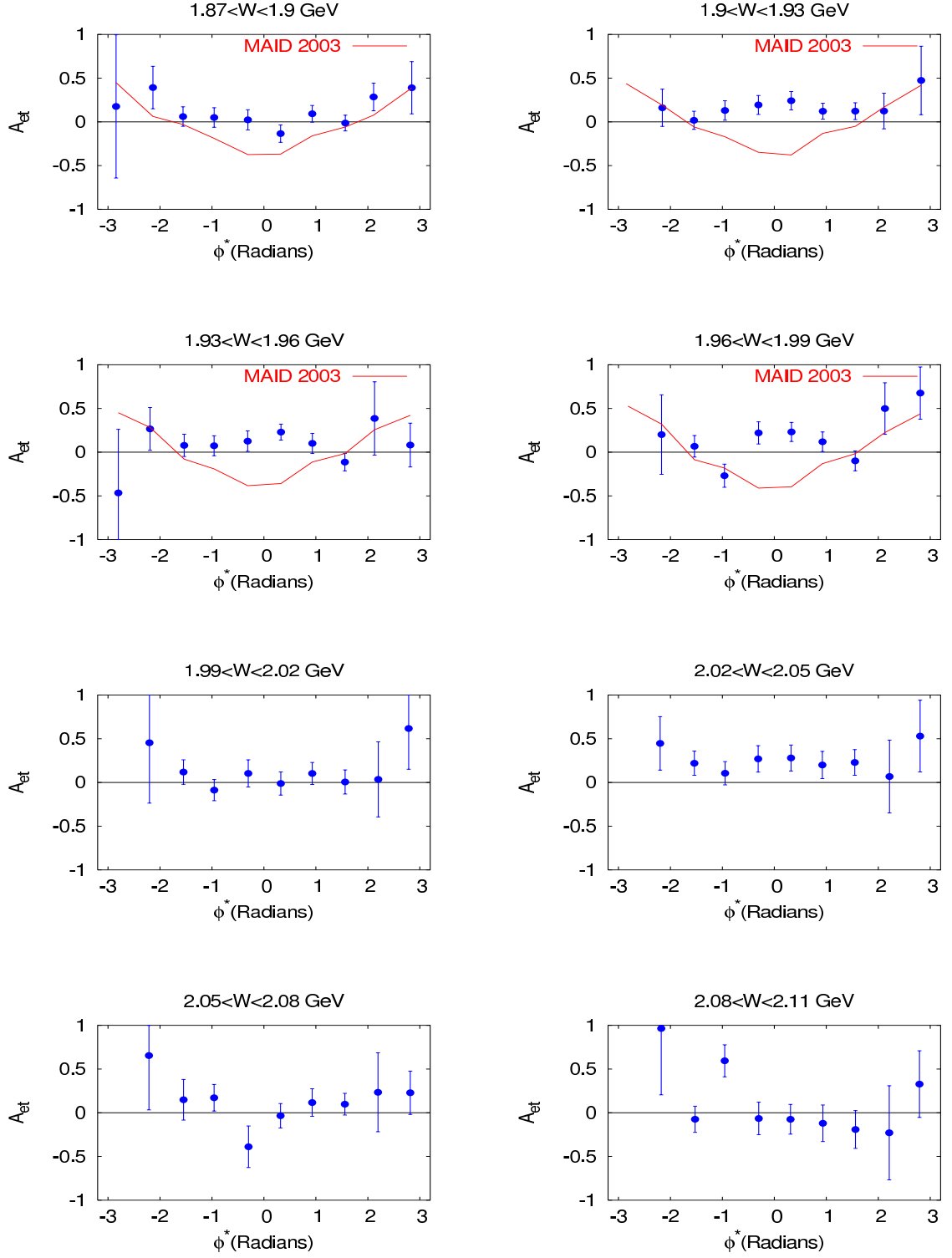
Figure B.12: A_{et} as a function of ϕ^* for each W bin from 1.87 GeV to 2.11 GeV. The asymmetry has been averaged over Q^2 and $\cos\theta^*$.

Bibliography

[1] P. D. Group, "Review of Particle Properties," Phys. Rev. D (2006).

[2] F. W. Brasse *et al.*, "Parametrization of the Q^2 dependence of virtual gamma p total cross-sections in the resonance region," Nucl. Phys. **B110**, 413 (1976).

[3] F. Foster and G. Hughes, "Electroproduction of nucleon resonances," Rept. Prog. Phys. **46**, 1445 (1983).

[4] M. J. Alguard *et al.*, "Deep inelastic e p asymmetry measurements and comparison with the Bjorken sum rule and models of the proton spin structure," Phys. Rev. Lett. **41**, 70 (1978).

[5] J. Bjorken and S. Drell, *Relativistic Quantum Mechanics* (McGraw-Hill, 1964).

[6] A. S. Raskin and T. W. Donnelly, "Polarization in coincidence electron scattering from nuclei," Ann. Phys. **191**, 78 (1989).

[7] G. Knochlein, D. Drechsel, and L. Tiator, "Photoproduction and electroproduction of eta mesons," Z. Phys. **A352**, 327 (1995).

[8] G. F. Chew, M. L. Goldberger, F. E. Low, and Y. Nambu, "Relativistic dispersion relation approach to photomeson production," Phys. Rev. **106**, 1345 (1957).

[9] D. Drechsel, O. Hanstein, S. S. Kamalov, and L. Tiator, "A unitary isobar model for pion photo- and electroproduction on the proton up to 1-GeV," Nucl. Phys. **A645**, 145 (1999).

[10] R. L. Walker, "Phenomenological analysis of single pion photoproduction," Phys. Rev. **182**, 1729 (1969).

[11] A. Bartl and W. Majerotto, "Electroproduction of pions with polarized beams and polarized targets," Nucl. Phys. **B62**, 267 (1973).

[12] R. Fatemi *et al.*, "Measurement of the proton spin structure function g1(x,Q^2) for Q^2 from 0.15-GeV^2 to 1.6-GeV^2 with CLAS," Phys. Rev. Lett. **91**, 222002 (2003).

[13] J. Yun *et al.*, "Measurement of inclusive spin structure functions of the deuteron with CLAS," Phys. Rev. **C67**, 055204 (2003).

[14] R. De Vita *et al.*, "First measurement of the double spin asymmetry in e(pol.) p(pol.) $\rightarrow$ e' pi+ n in the resonance region," Phys. Rev. Lett. **88**, 082001 (2002).

[15] V. Burkert and Z.-j. Li, "What do we know about the Q^2 evolution of the Gerasimov- Drell-Hearn sum rule?" Phys. Rev. **D47**, 46 (1993).

[16] K. Joo *et al.*, "Measurement of the polarized structure function $\sigma_{LT'}$ for p(e(pol.),e' pi+)n in the Delta(1232) resonance region," Phys. Rev. **C70**, 042201 (2004).

[17] K. Joo *et al.*, "Measurement of the polarized structure function $\sigma_{LT'}$ for pion electroproduction in the Roper resonance region," Phys. Rev. **C72**, 058202 (2005).

[18] H. Egiyan *et al.*, "Single pi+ electroproduction on the proton in the first and second resonance regions at 0.25-GeV^2 < Q^2 < 0.65- GeV^2 using CLAS," Phys. Rev. **C73**, 025204 (2006).

[19] V. D. Burkert and T. S. H. Lee, "Electromagnetic meson production in the nucleon resonance region," Int. J. Mod. Phys. **E13**, 1035 (2004).

[20] Y. Prok, "GDH Integral on the Proton from Asymmetries," JLAB-PHY-04-17.

[21] K. V. Dharmawardane *et al.*, "Measurement of the x- and Q^2-Dependence of the Asymmetry A_1 on the Nucleon," Phys. Lett. **B641**, 11 (2006).

[22] H. A. Grunder *et al.*, "The continuous electron beam accelerator facility," Nucl. Phys. **A478**, 831c (1988).

[23] T. Maruyama, E. L. Garwin, R. Prepost, and G. Zapalac, "Electron spin polarization in photoemission from strained GaAs grown on GaAsP," Phys. Rev. **B46**, 4261 (1992).

[24] E. Leader, *Spin in Particle Physics* (Cambridge University Press, 2005).

[25] B. A. Mecking *et al.*, "The CEBAF Large Acceptance Spectrometer (CLAS)," Nucl. Instrum. Meth. **A503**, 513 (2003).

[26] M. D. Mestayer *et al.*, "The CLAS drift chamber system," Nucl. Instrum. Meth. **A449**, 81 (2000).

[27] G. Adams *et al.*, "The CLAS Cherenkov detector," Nucl. Instrum. Meth. **A465**, 414 (2001).

[28] E. S. Smith *et al.*, "The time-of-flight system for CLAS," Nucl. Instrum. Meth. **A432**, 265 (1999).

[29] M. Amarian *et al.*, "The CLAS forward electromagnetic calorimeter," Nucl. Instrum. Meth. **A460**, 239 (2001).

[30] E. S. Smith *et al.*, "Calibration of CLAS TOF system," CLAS-NOTE 1999-011 (2003).

[31] P. L. Anthony *et al.*, "Measurements of the Q^2 dependence of the proton and neutron spin structure functions g1(p) and g1(n)," Phys. Lett. **B493**, 19 (2000).

[32] G. Warren *et al.*, "Measurement of the electric form factor of the neutron at Q^2 = 0.5-GeV/c^2 and 1.0-GeV/c^2," Phys. Rev. Lett. **92**, 042301 (2004).

[33] S. Goertz, W. Meyer, and G. Reicherz, "Polarized H, D and He-3 targets for particle physics experiments," Prog. Part. Nucl. Phys. **49**, 403 (2002).

[34] D. G. Crabb and W. Meyer, "Solid polarized targets for nuclear and particle physics experiments," Ann. Rev. Nucl. Part. Sci. **47**, 67 (1997).

[35] M. Borghini, "Proton spin orientation," (1968), CERN-68-32.

[36] E. Hughes, "SLAC experiment E142," (1990), invited talk given at 9th Int. Symp. on High Energy Spin Physics, Bonn, Germany, Sep 10-15, 1990.

[37] M. L. Seely, *Dynamic nuclear polarization of irradiated target materials*, Ph.D. thesis, Yale (1982), uMI-83-10583.

[38] C. D. Keith *et al.*, "A polarized target for the CLAS detector," Nucl. Instrum. Meth. **A501**, 327 (2003).

[39] G. R. Court, D. W. Gifford, P. Harrison, W. G. Heyes, and M. A. Houlden, "A High precision Q meter for the measurement of proton polarization in polarized targets," Nucl. Instrum. Meth. **A324**, 433 (1993).

[40] W. A. Tobias, *Measurement of the Proton and Deuteron Spin Structure Functions g_1 and g_2*, Ph.D. thesis, University of Virginia (2001).

[41] P. Bosted, "$P_t P_b$ from *ep* Coincidences for Eg1b," EG1b-Note-PB1 (2002).

[42] M. K. Jones *et al.*, "G(E(p))/G(M(p)) ratio by polarization transfer in e(pol.) p $\rightarrow$ e p(pol.)," Phys. Rev. Lett. **84**, 1398 (2000).

[43] S. Bosted, P. Kuhn and Y. Prok, "Raster Corrections for EG1b," CLAS-NOTE 2003-008 (2003).

[44] A. Klimenko and S. Kuhn, "Momentum Corrections for E6," CLAS-NOTE 2003-005 (2003).

[45] H. Bosted, P. Avakian, "Multiple Scattering and Stray Magnetic Field Corrections for Tracking in the Presence of Target Field," CLAS-NOTE 2006-006 (2006).

[46] O. A. Rondon, "Corrections to nucleon spin structure asymmetries measured on nuclear polarized targets," Phys. Rev. **C60**, 035201 (1999).

[47] R. De Vita, *Measurement of the double spin asymmetry of exclusive π^+ electroproduction with CLAS*, Ph.D. thesis, Universita degli Studi di Genova (2000).

[48] M. Ripani *et al.*, "The GDH Sum Rule with Nearly Real Photons and the Proton g_1 Structure Function at Low Momentum Transfer," Experiment Proposal.

[49] S. Kuhn *et al.*, "The Longitudinal Spin Structure of the Nucleon," Experiment Proposal (Approved).